Mono- and Multivalent Interactions between Thiol and Amine Ligands with Noble Metal Nanoparticles

Inaugural-Dissertation

to obtain the academic degree

Doctor rerum naturalium (Dr. rer. nat)

submitted to the Department of Biology, Chemistry and Pharmacy

of Freie Universität Berlin

by

SUGUNA PERUMAL

from (Dharmapuri, India)

April 2012

This work was performed during February 2008 – April 2012 at the Physical and Theoretical Chemistry, Institute for Chemistry and Biochemistry, Freie Universität Berlin in the group of Prof. Dr. Eckart Rühl.

1st Reviewer: Prof. Dr. Eckart Rühl

2nd Reviewer: Prof. Dr. Christina Graf

date of defence:22.06.2012

To my Parents, Sisters and Brothers

Abstract

In this thesis, the interactions between mono- and multivalent thiol and amine ligands and noble metal nanoparticles are investigated. The multivalent interactions are characterized by the simultaneous binding of multivalent ligands on one entity to multivalent receptors on another one. The binding affinities of multivalent ligands are stronger than that of monovalent ones. So far, multivalent interactions with nanoparticles are not fully explored. Therefore, different physico-chemical techniques are used to investigate the interactions between mono- and multivalent ligands with nanoparticles.

The results gathered in this work are divided into four parts. In first part, the effect of the ligand's multivalency and the nanoparticles size on the binding kinetics of thiol ligands on gold nanoparticles is evaluated by exchanging monovalently bound pyrene thiol ligands bound to gold nanoparticles against flexible mono- and multivalent thiol ligands. For this, gold nanoparticles with diameters of 2.2 ± 0.4 nm, 3.2 ± 0.7 nm, and 4.4 ± 0.9 nm are used as substrates. The pyrene thiol is used as a fluorescent probe as well as a stabilizer of the gold nanoparticles before the ligand exchange reaction takes place. The effects of the ligand's multivalency and the particles size are evaluated by comparing the rate constants of the ligand exchange reactions. To evaluate these effects, the experimental data have been fitted by using various models. The results from kinetics studies are well fitted by a bi-exponential function as well as by a second order Langmuir diffusion models. However, only a bi-exponential fit function can reasonably explain the processes occurring with the ligand exchange process. Systematic investigations reveal a significant enhancement of the reaction rates of di- and trivalent ligands compared to the monovalent ones. This is attributed to a distinct multivalency effect. In contrast, the exchange rates of the trivalent ligands are similar or even lower than those of the divalent ones. This is explained by steric hindrance of bulky trivalent ligands. In addition, it is also observed that the rate constants increase with the particle size. The results are used to derive structural information on the binding of the mono- and multivalent ligands to the nanoparticles surface. Furthermore, it turns out, that gold particles larger than 4 nm in diameter aggregate during the ligand exchange

reaction, likely because the non-bulky incoming alkyl thiol ligands do not provide sufficient steric stabilization.

In the second part of this work, the binding of rigid aromatic thiols on gold nanoparticles of 2.2±0.4 nm, 3.2±0.7 nm, and 4.4±0.9 nm is investigated. The pyrene thiol bound on gold nanoparticles is exchanged by 4-toluenethiol or 3,4-toluenedithiol. During the exchange reaction, the particles aggregate immediately after the addition of the aromatic rigid thiol ligands. This clearly shows that flexible alkyl thiol ligands provide sufficient steric stabilization for the gold nanoparticles than the rigid aromatic thiol ligands.

In the third part, the binding of mono- and multivalent alkyl thiol ligands on silver nanoparticles with 4.6±2.0 nm diameter is studied, wherein the same alkyl thiol ligands which are also used in the experiments on gold nanoparticles are used. Silver particles stabilized by pyrene thiol ligands are synthesized and the thiol ligands are exchanged by the mono- and multivalent alkyl thiol ligands. During the exchange process partial precipitation of the particles occurs as a consequence of severe aggregation. The results on the silver nanoparticles are compared to those obtained from gold nanoparticles of a similar size (4.4±0.9 nm) during the exchange of pyrene thiol against mono- and multivalent alkyl thiol ligands. The exchange rates of pyrene thiol with di- and trivalent ligands are similar for silver and gold nanoparticles. In case of the monovalent ligands, initially, the exchange rate on silver nanoparticles seems to be faster than on gold nanoparticles.

In last part of this work, the influence of the presence of mono-, di-, and trivalent alkyl amine ligands on the nucleation and growth of platinum and silver nanoparticles is investigated. Here, for the first time mono- and multivalent amine ligands are used to control the formation of platinum and silver nanoparticles using platinum (II) acetylacetonate and silver (II) acetylacetonate as precursors, respectively. Platinum and silver nanoparticles are prepared by one-step processes at 200 °C and 120 °C, respectively, in order to investigate the influence of the amine ligands on the formation of nanoparticles. Additionally, procedures are applied, where the reaction temperature is stepwise increased between 160 and 200 °C in the case of platinum and between 80 and 120 °C for silver. The multivalency effects of the ligands on the formation of

platinum particles are investigated by using TEM measurements. The platinum particles prepared at 200 °C in the presence of monovalent ligands are rather polydisperse and have a non-spherical shape, whereas the di- and trivalent ligands cause the growth of monodisperse and spherical particles. In contrast, platinum particles prepared by stepwise increasing the temperature have a spherical shape independent on the ligand multivalency and the reaction temperature. The influence of the ligand's multivalency on the formation, growth, and stability of silver particles is investigated by TEM and UV-Vis measurements. The size distributions of the silver particles prepared by a one-step process are wider than those of the particles prepared by a stepwise process. This is because faster nucleation and growth processes take place and as a consequence, nucleation and growth are not well separated if the particles are prepared by a one-step process at high temperature instead of a stepwise process at lower temperatures.

Kurzfassung

In dieser Arbeit werden die Wechselwirkungen zwischen mono- und multivalenten Thiol- und Amin-Liganden und Edelmetall-Nanopartikeln untersucht. Charakteristisch für die multivalenten Wechselwirkungen ist die zeitgleiche Bindung multivalenter Liganden einer Spezies an multivalente Rezeptoren einer anderen Spezies. Dabei ist die Bindungsenergie der multivalenten Bindung größer, als die Summe der einzelnen, monovalenten Bindungen. Die Untersuchung des Multivalenzeffektes erfolgt mittels verschiedener physikalisch-chemischer Techniken mit dem Ziel, das grundlegende Verständnis der Wechselwirkungen zwischen multivalenten Liganden und Nanopartikeln zu verbessern.

Die Ergebnisse dieser Arbeiten sind in vier Teilen zusammengefasst. Im ersten Teil werden der Einfluss der Multivalenz der Liganden sowie der Größe der Nanopartikel auf die Bindungskinetik von Thiol-Liganden auf Goldnanopartikel anhand des Austausches von monovalent gebundenen Pyren-Thiol-Liganden gegen flexible mono- und multivalente Alkyl-Thiol-Liganden untersucht. Dazu werden Gold-Nanopartikel mit einem Druchmesser von 2.2±0.4 nm, 3.2±0.7 nm und 4.4±0.9 nm als Substrat verwendet. Die Pyren-Thiol-Liganden dienen als fluoreszierende Sonden und zur Stabilisierung der Goldnanopartikel vor dem Ligandenaustausch. Die Auswirkungen der Multivalenz der Liganden und der Partikelgröße werden durch den Vergleich der Geschwindigkeitskonstanten der Liganden-Austausch-Reaktionen ermittelt. Um diese besser beurteilen zu können, wurden die erhaltenen Ergebnisse mit verschiedenen Modellen angepasst. Es stellte sich heraus, dass sich die Daten aus den Kinetik-Versuchen mit einer biexponentiellen Funktion und einem Langmuir-Diffusions-Modell zweiter Ordnung grundsätzlich annähern lassen. Zur Anwendung kam jedoch ausschließlich das biexponentielle Modell, da dieses die ablaufenden Prozesse korrekt beschreibt. Systematische Untersuchungen zeigen eine deutliche Erhöhung der Reaktionsgeschwindigkeit di- und trivalenter Liganden im Vergleich zu den monovalenten Liganden. Dies ist auf einen deutlichen Multivalenzeffekt zurückzuführen. Im Gegensatz dazu ist die Austauschgeschwindigkeit der trivalenten Liganden ähnlich oder gar niedriger als die der divalenten Liganden. Dies wird durch die sterische Hinderung der sterisch anspruchsvollen trivalenten Liganden erklärt. Darüber

hinaus wird beobachtet, dass die Geschwindigkeitskonstanten mit zunehmender Teilchengröße steigen. Die erhaltenen Resultate werden dazu genutzt, Informationen über die Struktur der Bindung der mono- und multivalenten Liganden an die Nanopartikel-Oberfläche abzuleiten. Darüber hinaus hat sich gezeigt, dass Gold-Partikel mit einem Durchmesser von mehr als 4 nm während des Ligandenaustausches aggregieren. Dies ist wahrscheinlich auf die unzureichende sterische Stabilisierung durch die Alkyl-Thiol-Liganden zurückzuführen.

Im zweiten Teil wird die Bindung von starren, aromatischen Thiolen an Goldnanopartikel mit einem Durchmesser von 2.2±0.4 nm, 3.2±0.7 nm und 4.4±0.9 nm untersucht. Die an die Partikel gebundenen Pyren-Thiol-Liganden werden gegen 4-Toluolthiol und 3,4-Toluoldithiol substituiert. Während des Ligandenaustausches aggregieren die Teilchen unmittelbar nach der Zugabe der aromatischen Thiole. Dies ist möglicherweis auf eine unzulängliche sterische Stabilisierung der Goldpartikel durch die starren, aromatischen Thiol-Liganden zurückzuführen. Es wird deutlich, dass die flexiblen Alkyl-Thiol-Liganden im Vergleich zu den starren, aromatischen Thiolen eine stärkere Stabilisierung der Goldnanopartikel gewährleisten.

Im dritten Abschnitt wird die Bindung von mono- und multivalenten Alkyl-Thiol-Liganden an Silber-Nanopartikel mit 4.6±2.0 nm Durchmesser untersucht, wobei die gleichen Liganden, die auch in den Versuchen mit den Gold-Nanopartikeln genutzt wurden, zum Einsatz kommen. Durch Pyren-Thiol-Liganden stabilisierte Silberpartikel werden synthetisiert und anschließend die Pyren-Liganden gegen mono- und multivalente Alkyl-Thiol-Liganden substituiert. Im Zuge dieses Austauschprozesses fallen die Partikel teilweise aus, was eine Folge ausgeprägter Aggregationsprozesse ist. Die erhaltenen Ergebnisse zu Silber-Nanopartikeln werden mit den Ergebnissen zum Ligandenaustausch von Pyren-Thiol-Liganden gegen mono- und multivalente Alkyl-Thiol-Liganden an Gold-Nanopartikel gleicher Größe verglichen. Die Austauschgeschwindigkeit von Pyren-Thiolen gegen di- und trivalente Liganden liegen im Fall von Gold- wie Silber-Nanopartikeln in derselben Größenordnung. Im Fall der monovalenten Liganden scheint die Austauschgeschwindigkeit der Liganden, die an Silberpartikel gebunden sind, höher zu sein als für Goldnanopartikel.

Im letzten Teil dieser Arbeit wird der Einfluss von mono-, di- und trivalenten Alkyl-Amin-Liganden auf die Nukleation und das Wachstum von Platin- und Silber-Nanopartikel untersucht. Zum ersten Mal wurden mono- und multivalente Amin-Liganden verwendet, um die Bildung der Platin- und Silber-Nanopartikel aus den Vorstufen Platin(II)acetylacetonat bzw. Silber(II)acetylacetonat zu steuern. Um den Einfluss der Amin-Liganden auf die Partikelbildung zu untersuchen, werden Platin- und Silber-Nanopartikel zum einen durch ein einstufiges Verfahren bei 200 °C für Platin beziehungsweise 120 °C für Silber dargestellt. Zum anderen erfolgt die Synthese der Partikel durch ein Verfahren, bei dem die Reaktionstemperatur schrittweise zwischen 160 und 200 °C im Fall von Platin bzw. 80 und 120 °C im Fall von Silber erhöht wird. Die Auswirkungen des Multivalenz-Effektes der Liganden auf die Bildung von Platinpartikel wird vor allem durch TEM-Experimente untersucht. Die bei 200 °C in Gegenwart monovalenter Liganden dargestellten Platin-Nanopartikel weisen eine nicht-sphärische Form auf, wohingegen die mittels di- und trivalenten Liganden synthetisierten Partikel sphärisch sind. Im Gegensatz dazu führt die Synthesemethode mit einem schrittweisen Anstieg der Temperatur zu sphärischen Partikeln, unabhängig von der Wahl des Liganden. Der Einfluss der Valenz der Liganden auf die Bildung, das Wachstum und die Stabilität der Silber-Partikel wird mittels dem TEM- und UV-Vis-Messungen untersucht. Die Größenverteilung der Silberpartikel aus dem einstufigen Syntheseprozess ist breiter als die der Teilchen, die durch ein stufenweises Verfahren hergestellt worden sind. Der Grund hierfür liegt in den schnelleren Nukleations- und Wachstumsprozessen im Fall des einstufigen Prozesses bei hohen Temperaturen, die keine deutliche Trennung von Nukleation und Wachstum zulassen.

Table of Contents

1. Introduction

Multivalent interactions are common in nature, for example the binding of antibodies to cells and cell-cell recognition.[1] Multivalent interactions are characterized by the simultaneous binding of multiple ligands on one entity to multiple receptors on another entity.[2] These multivalent interactions have a number of characteristics that monovalent interactions do not have. The major advantages of multivalent interactions are that they can be collectively much stronger than the corresponding monovalent interactions. There has been a growing interest in using this advantage to design effective multivalent molecules influencing biological interactions.[1-5] As a result, the multivalent ligands have been used as powerful inhibitors,[2] strong effectors,[4] in pharmaceutical agents, such as anticancer vaccines,[4] bacterial toxins,[4] and also to promote desired cellular responses.[3] Multivalent ligands can be small molecules,[6] dendrimers,[6] glycopeptides,[4, 6] cyclic peptide scaffolds,[7] or alkyl ligands.[8] Multivalently ligand stabilized metal nanoparticles also show multivalent activity.[9] Among the metal nanoparticles, noble metal nanoparticles, such as gold, silver, and platinum nanoparticles are promising candidates for studies of multivalent effects. Carbohydrates bound gold nanoparticles are found to be powerful inhibitors.[10] Where glycopeptides stabilized metal nanoparticles are used as antigens.[9] In general, nanoscale materials, are an intermediate state between molecular and bulk matter which possesses unique chemical and physical properties which drive significant fundamental and technological interest.[11] Thus, metallic nanoparticles are used in biochemistry, in catalysis, and nanostructured magnetism (such as storage devices).[11-13] Most of the attractive applications of the metallic nanoparticles are based on the particle's surface plasmon resonance (SPR) which is strongly dependent on their specific size and shape.[14] In principle, the plasmon band of nanoparticles can be systematically tuned by controlling their size and shape evolution during particle growth.[15-17] Further, the shape of the nanoparticles can be controlled by varying the ligands[18] and their concentration.[19] Until now, the growth mechanisms for the formation of nanoparticles are not well understood. Earlier reports show that the ligands used to stabilize the particles play an important role during the formation of the particles,[15-17] influencing their size and shape.[18, 19]

1

In general, thiols, amines, phosphines, carboxylates, and polymers have been successfully used as stabilizers for metallic nanoparticles.[20] Multivalent alkyl ligands are also can be used to stabilize the nanoparticles[21] and it has been explained that the multivalent ligands enhance the stabilization of the particles by an entropy-driven chelate effect.[22]

The ligands on the nanoparticles can be tuned to design the nanoparticles for various techniques, such as biosensors,[21] opto-eletronics,[21] and also in biological applications.[22] Tuning of the ligands on nanoparticles can be achieved by ligand exchange reaction and can be used to design novel functionalities on nanoparticles.[22, 23] The mechanism of the ligand exchange of aromatic and alkane thiol ligands on gold clusters are studied by Murray and co-workers.[24, 25] A key feature of nanoparticles is the fact that their surface is imperfect, which results in two defects sites, corresponding to the vertices and the edges, and one nondefect site (terrace or face) for binding of ligands.[24, 25] These different sites have different electron densities and steric behavior and hence will exhibit with different reactivity.[24]

In general, the ligand exchange studies were done using Nuclear Magnetic Resonance (NMR)[24, 25] as well as Electron Paramagnetic Resonance (EPR).[26] Typical acquisition times of ≥15 s per spectrum are required by NMR and EPR, which usually resulted in time intervals of 1-5 min between measurements in kinetics experiments. These difficulties can be overcome by using the optical spectroscopy methods. For the first time, Montalti et al. investigated exchange reactions using time resolved fluorescence spectroscopy.[27] This technique is versatile for the investigation of fast reactions involving changes in optical properties of reactants and products, providing a temporal resolution in the sub-second regime. However, systematic studies of the size dependence of the kinetics of ligand exchange reactions on gold nanoparticles of 2-15 nm have not been reported to date.

Thus, the aim of this thesis is to investigate the binding kinetics of different types of ligands on different types of nanoparticles. Further, it is aimed to study the effect of ligand multivalency on the formation of the silver and platinum nanoparticles.

In the Section 4.1, the binding kinetics of mono-, di-, and trivalent alkyl thiol ligands on gold nanoparticles of 2.2±0.4 nm, 3.2±0.7 nm, and 4.4±0.9 nm in diameter are investigated. For this, pyrene thiol capped gold nanoparticles are synthesized by wet colloidal chemistry. The ligands

(mono-, di-, and trivalent) are chosen in such a way that the lengths of the alkyl chains are almost the same. Then, the kinetics exchange reaction between pyrene thiol by mono- and multivalent thiol ligands are also studied using time-resolved fluorescence spectroscopy.

In the Section 4.2, the binding of aromatic rigid thiols on three different sizes of the gold nanoparticles (2.2 nm, 3.2 nm, and 4.4 nm in diameter) are investigated. For this, the pyrene thiols bound on the three different sizes of the gold nanoparticles are exchanged by 4-toluenethiol (Ar-monovalent thiol) and 3,4-toluenedithiol (Ar-divalent thiol). In Section 4.3, the binding of alkyl mono- and multivalent thiol ligands (the same alkyl thiol ligands used in Section 4.1) on silver nanoparticles is studied.

In Section 4.4, the influence of mono-, di-, and trivalent alkyl amine ligands on the formation and stability of platinum and silver nanoparticles are investigated. The particles are prepared by using platinum (II) acetylacetonate and silver (II) acetylacetonate as precursors by a one-step process and also by stepwise increasing the temperature. Then, the ligand multivalency effects are investigated using TEM and UV-Vis measurements.

2. Background discussion

2.1. Multivalent interactions

Multivalent interactions are of fundamental importance since numerous interactions in living systems, for example binding of antibodies to cells or cell-cell recognition, involve multivalent interactions.[2] Multivalent interaction is characterized by the simultaneous binding of multiple ligands on one entity to multiple receptors located on another site, as shown in Figure 2.1. Multivalent interactions are known to be significantly stronger than the corresponding monovalent ones.[2] The multivalent interactions have a number of characteristics that monovalent interactions do not have. For example, multivalent ligands have a higher avidity, which is known as the association constant of the multivalent interactions.[2] This avidity constant is a collective association constant that corresponds to multiple interactions between multiple ligands (N) and multiple receptors (N).
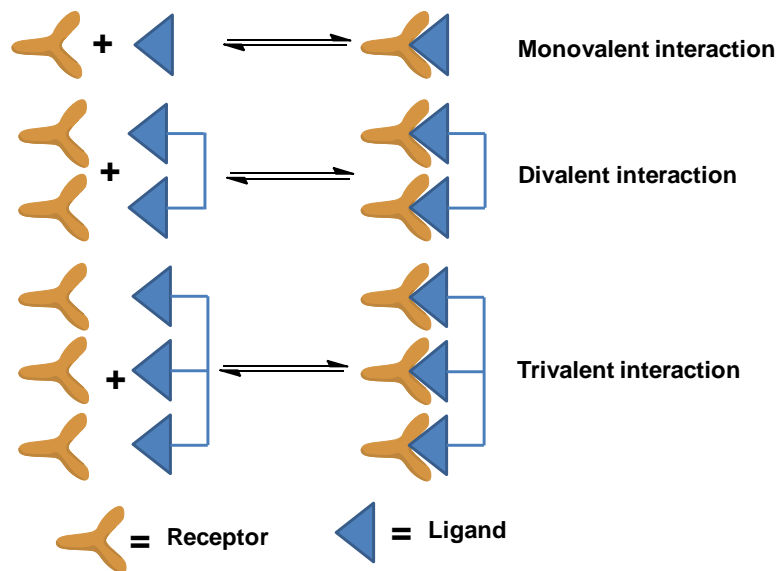
Figure 2.1: Mono- and multivalent interactions between receptors and ligands.[2]

The thermodynamic principles of multivalent interactions have been investigated by several groups.[2, 4-7, 28] The following discussion is essentially based on a review published by Mammen et al.[2] and a book published by Seok-Ki Choi.[28] The term "affinity" is a qualitative term and the affinity constant (K_a) is the association constant.[2, 28] For a monovalent system, which is composed of a receptor and a ligand, the affinity constant (K_a^{mono}) is the binding strength. This binding strength is related to the free energy of association (ΔG^{mono}) by the Gibbs equation, as shown in equation 2.1.[2, 28]

$$\Delta G^{mono} = -RTln(K_a^{mono}) \qquad\qquad 2.1$$

For the multivalent system, which has more than one receptor and ligand, the association constant is defined as "avidity" (K_a^{multi}). The relationship of the avidity constant with the free energy of association (ΔG_N^{multi}) is defined as follows: [2, 28]

$$\Delta G_N^{multi} = -RTln(K_a^{mono}) \qquad\qquad 2.2$$

In many cases, the avidity (K_a^{multi}) is found to be greater than the affinity K_a^{mono}. The average free energy interaction between a ligand and receptor of a multivalent system (ΔG_N^{multi}) can be greater than, equal to, or less than the free energy in the analogous monovalent interaction $N\Delta G^{mono}$, where N is independent of receptor-ligand interactions. The ratio between both quantities indicates the degree of cooperativity, where the corresponding coefficient (α) is defined as: [2, 28]

$$\alpha = \frac{\Delta G_N^{multi}}{N\Delta G^{mono}} \qquad\qquad 2.3$$

Depending on the magnitude of α, multivalent interaction is either positively cooperative i.e. synergistic (α > 1), or noncooperative i.e. additive (α = 1), or negatively cooperative i.e. interfering (α < 1). The term cooperativity is often used for biological system, which shows

positive cooperativity or synergistic. However, there are presently no convincingly characterized examples of positive cooperativity for multivalent systems in the literature. Thus, cooperativity, as defined for traditional biological system, is neither a useful nor a descriptive parameter for multivalent systems, as it is for monovalent ones. Therefore, a new term (β) is introduced, describing the enhancement of binding of multivalent association. The quantity β is the ratio of avidity and the component affinity of the corresponding monovalent interaction. Thus, the enhancement factor (β) can be expressed by: [2, 28]

$$\beta = \frac{K_a^{multi}}{K_a^{mono}}$$

2.4

The free energy (ΔG_N^{multi}) consists of enthalpic (ΔH_N^{multi}) and entropic (ΔS_N^{multi}) components as shown in equation 2.5.

$$\Delta G_N^{multi} = \Delta H_N^{multi} - T\Delta S_N^{multi}$$

2.5

As an approximation, ΔH_N^{multi} can be estimated by the sum of enthalpies of N monovalent interactions ($N\Delta H^{mono}$). The enthalpy value of multivalent systems may be either larger or smaller by other interactions around the active site. If the binding of one ligand to a receptor with a given enthalpy cause another ligand to bind to its receptor with greater enthalpy, then the value of the enthalpy (ΔH_{avg}^{multi}) is more negative (i.e. more favorable) than the value of ΔH^{mono}. Such binding is referred as enthalpically enhanced binding. If the binding of one ligand to its receptor interferes with the next ligand to bind to its receptor, then the enthalpy of the multivalent system is less favorable than that expected for N equivalent monovalent interactions. Such binding is referred as enthalpically diminished binding. This enthalpy diminished binding can occur when multiple ligand-receptor interactions between multiple entities require energetically unfavorable molecular conformations. Thus, the enthalpy of binding for multivalent interactions is easy to explain qualitatively, but it is difficult to estimate quantitatively, by experiments or theoretical models.

Understanding the entropy changes of multivalent interactions (ΔS_N^{multi}) it is essential to understand the relationship of monovalent to multivalent binding. As an approximation, the value of ΔS_N^{multi} is the sum of the enthalpies of N monovalent interactions ($N\Delta S^{mono}$). The total entropy change involved it is assumed that changes primarily occur in the translational and rotational entropies of the ligands and receptors upon association. This can be expressed by equation 2.6.

$$\Delta S_N^{multi} \approx \Delta S_N^{mono}(\text{translational}) + \Delta S_N^{mono}(\text{rotational})$$

2.6

Equation 2.6 represents a summation of the mentioned factors, where it is assumed that the translations and rotations make more significant contributions than the other ones, such as conformational, vibrational, and solvation entropy changes, which are considered to be relatively unimportant. Then, the entropy can be expressed by equation 2.7.

$$\Delta S_N^{multi} \approx \Delta S_N^{mono}(\text{translational}) + \Delta S_N^{mono}(\text{rotational})$$
$$+\Delta S_N^{multi}(\text{conformational, linker})$$

2.7

The above mentioned explanations reveal that the multivalent interactions provide the basis for mechanisms, which are fundamentally different from those of the corresponding monovalent systems. The monovalent ligands typically bind to a single receptor; whereas multivalent ligands interact by different mechanisms, such as chelate effects, subsite binding, receptor clustering, and statistical rebinding. These interaction mechanisms were explained in greater detail by Mammen et al.,[2] Gestwicki et al.,[6] and Kiessling et al..[4] Recently, Perl, et al.[5] have explained the kinetics of multivalent interactions at the interfaces. There, the movement of multivalent ligands across an artificial multivalent surface involves a combination of mechanisms of hopping, walking, and flying.[5, 7] Due to their high affinity, multivalent interactions are currently of great interest to understand biological processes.[1, 2, 4-7, 9, 10, 28-31] The multivalent ligands can be alkyl ligands,[8, 32] small molecules,[6] dendrimers,[6] glycopeptides,[2, 4, 6, 10, 28, 29] cyclic peptides,[7, 30] or polymers.[2, 4-7] Chemical structures of such different types of multivalent ligands are shown in Figure.2.2.
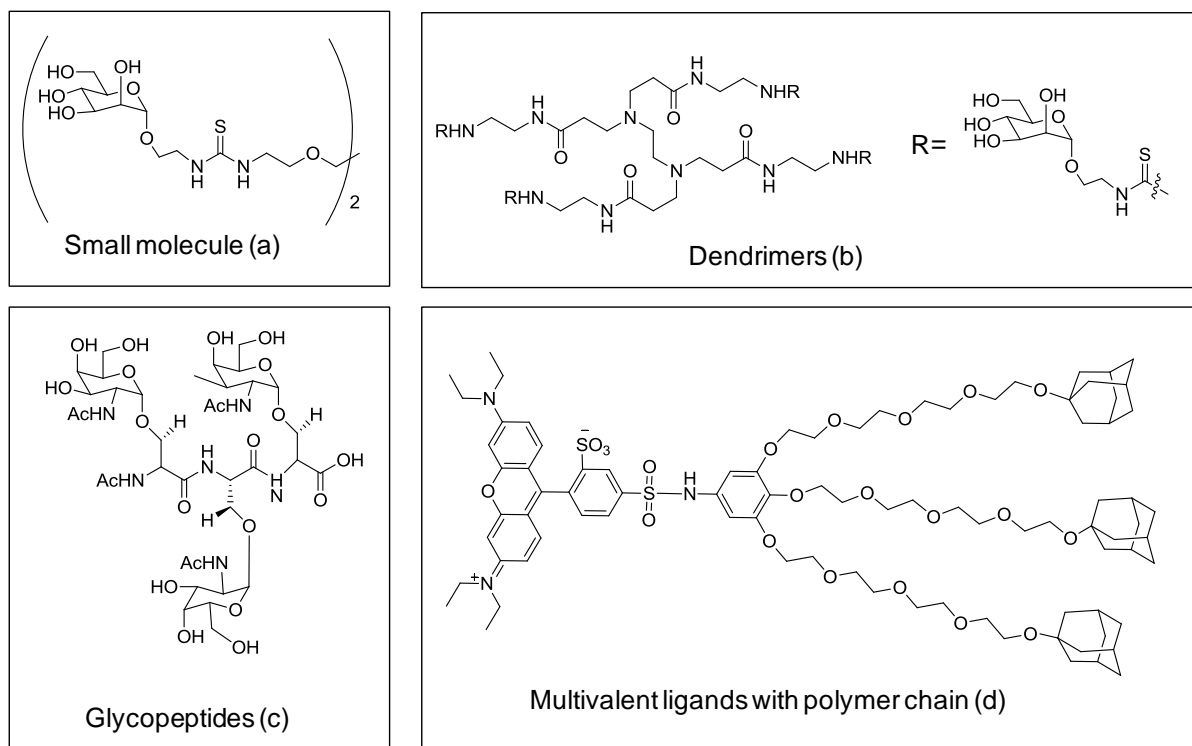
Figure 2.2: Chemical structures of multivalent ligands: (a) small molecular dimers,[6] (b) dendrimers of zero generation,[6] (c) glycopeptides,[29] and (d) multivalent ligands with adamantane and fluorescent moieties.[5, 7]

The multivalent ligands can act as powerful inhibitors[2] or potent effectors.[4] Moreover, the concept of multivalency is useful for developing novel strategies for designing multivalent carbohydrates[4] and pharmaceutical agents, such as anticancer vaccines.[4] Synthetic multivalent glycopeptides are also used as HIV antigens.[30] These synthetic antigens have functional groups which can attach to a carrier protein and permits to use it as a vaccine.[30, 31] These multivalent ligands can also be used to stabilize nanoparticles and they may form self-assembled monolayers on surface, as shown in the Figure 2.3.[10, 32]
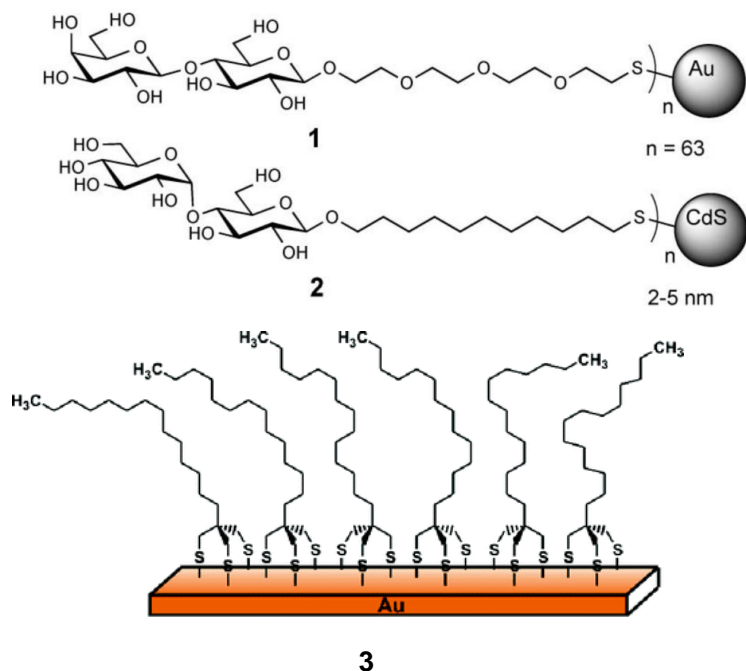
Figure 2.3: Glycosides bound to gold nanoparticles (1),[10] quantum dots (2),[10] and schematic representation of a self-assembled monolayer of multivalent ligands on a gold surface.[32]

Carbohydrates bound to nanoparticles, such as quantum dots are found to be potent inhibitors.[10] Further, multivalent saccharide-stabilized nanoparticles are used as antigens.[9] Multivalent alkyl ligands are used for the preparation of self-assembled monolayers, where the chelating alkane molecules control the packing density on the gold surface better than the corresponding monovalent systems.[8]

2.2. Nanoparticles

Nanoparticles are microscopic particles with at least one dimension on the nanometer scale (1-100 nm).[11] The transition from microparticles to nanoparticles can lead to a number of changes in physical properties. The two major factors in this area are the increase in the surface-to-volume-ratio and the size of the particles moving into the regime, where quantum effects dominate. The particle size gets smaller as the surface-area-to-volume ratio increases and, thus, leads to dominance of the behavior of atoms on the surface than those in the bulk interior of the particles. This affects the size-dependent properties of the particles and the interactions with their surroundings. Such unique properties of nanoparticles are different from the corresponding bulk materials. Nanoparticle research is currently an area of intense scientific research, which is due to a wide variety of promising applications in biomedical, optical, and electronic fields.[11]

2.2.1. Metallic nanoparticles

Metallic nanoparticles with sub nanometer core dimensions are of main interest to fundamental research.[11-13] In general, metallic nanoparticles exhibit distinct properties, which are quite different from those of the individual atomic or molecular constituents, surfaces, or bulk materials.[11] Especially, noble-metal nanoparticles have received significant attention, since their initial use in the 17th century. They were used at that time for ornamental decoration,[12] such metal nanoparticles were used in the form of colloids or sols.[12] Michael Faraday[33] has prepared in 1857 stable sols and elucidated the mechanism for the formation of metallic colloids. The metallic nanoparticles have fascinating spectroscopic, electronic, and chemical properties depending on the particle size and shape.[11-13, 33, 34] Thus, their applications are diverse and interdisciplinary, which reaches also into the fields of biochemistry, catalysis, as well as chemical and biological sensors, systems for nanoelectronics, nanostructured magnetism (e.g. data storage devices), and medicine, where their potential use for drug delivery has been considered.[11-13, 33]

2.2.2. Synthesis strategies to prepare metallic nanoparticles and its size and shape effects

Metal nanoparticles can be prepared by two major methods, the bottom up approach and the top down approach.[33, 34] The particles can either be built from separate atoms by using the bottom up approach, which makes use of chemical methods of nanoparticle preparation. In contrast, in the top down approach, the nanoparticles can be prepared by using various dispersion and aggregation procedures, which make use of physical methods. For example, particles are prepared by evaporation of a metal in vacuum by resistive heating, or laser ablation.[12] Then, the size of the nanoparticles cannot be exactly controlled during evaporation but it is possible to narrow the size distribution by controlling the rate of evaporation.

In this thesis nanoparticle preparation was performed by using chemical methods, i.e. the bottom up approach. Moreover, the ligands used are hydrophilic (amines, thiol), so that the chemical methods used to prepare such hydrophilic ligand stabilized particles are explained in detail.

The chemical methods includes, salt reduction, photochemical processes, and sonochemical procedures.[12, 35, 36] Decomposition of appropriate metastable precursor molecules also permits to prepare metallic nanoparticles.[34, 35] In any case, formation of nanoparticles occurs when individual, neutral atoms, are subjected to collide with each other, resulting in nucleation to form nuclei. Subsequent particles growth can be influenced by the concentration of the reactants, the solvent, reducing agents, and specifically by the presence of a stabilizing agent.[34] Short nucleation times support the formation of monodisperse particles, since freshly generated atoms will be trapped by existing nuclei in a diffusion-controlled growth. Consequently, no new particles will be formed and formation of a broad particle size distribution is prevented. An important factor of particle formation is the specific surface energy of the corresponding metal. If the surface energy is significantly higher than the loss of entropy, then Ostwald ripening[34] will occur, where smaller particles grow to larger ones, leading to a broad particle size distribution. Passivation of the particle surfaces due to the presence of appropriate ligands may result in size-selective generation of nanoparticles. This process helps not only to prepare size selective nanoparticles but also to prevent the particles from so-called agglomeration. The process called

digestive ripening occurs by heating the particle solution to an appropriate temperature with an excess of ligands.[35-37] The reason for the occurrence of this process is that the larger particles will be reduced in size, whereas the smaller particles will grow. This is a reverse process of Ostwald ripening, which is caused by the thermodynamically favored reduction of nonstabilized surfaces.

Other than controlling the size of nanoparticles, controlling their shape also provides further challenges, especially because of possible applications in various areas of nanotechnology.[35, 38] The synthesis of shape-controlled metal nanoparticles has developed significantly during the past decade. They are in the ideal case single-crystalline, but in reality they are often polycrystalline. Both, the thermodynamic and kinetic factors must be considered to control the shape of particles. In a thermodynamically controlled reaction the most stable product will be formed, whereas in kinetically controlled particle formation the speed of reduction or decomposition of the reactants during crystal germ formation will dominate.[38] The thermodynamically most stable shapes would be truncated spheres, cubes, rods, hollow cages, wires, octahedrons, and tetrahedrons. Kinetic factors in particle growth play a dominant role, where the reaction conditions, such as reaction time, stabilizers, concentrations of the metal precursor, and the temperature influence both the nucleation process and crystal growth. The size and shape control is the main point to recognize in fabrication of metallic nanoparticles. The reason behind this increasing interest in metal nanoparticles of distinct shape is due to numerous shape-dependent properties, especially in the optics field, as will be elucidated in the following.

2.2.3. Optical properties of metallic nanoparticles

Apart from the optical properties of nanoparticles, some other properties, such as their electronic and chemical properties are also affected by size and shape. This Section covers only the optical properties, since they are of primary relevance to the present work. It is known that electromagnetic surface waves can propagate along the interface between conducting materials and a dielectric over a broad range of frequencies.[14, 38-41] The absorption band, which is induced by an interacting electromagnetic field with a collective oscillation of valence electrons, is

referred to a surface plasmon. The oscillation wavelength depends on number of factors, such as particle size, shape, color of the particles, as well as the surrounding medium.[14] The electric field of the incoming radiation induces the formation of a dipole in the nanoparticles. This results in unique resonance wavelengths, as shown in Figure 2.4, as taken from a review of Liz-Marzán.[14]
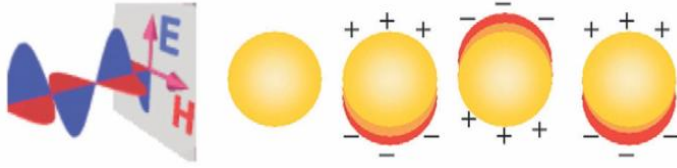
Figure 2.4: Schematic diagram of the interaction of electromagnetic radiation with a metal nanosphere. A dipole is induced, which oscillates in phase with the electric field of the incoming light.[14]

The resonance depends on the dielectric properties of the metals and can be explained by using Mie theory.[14, 38, 40, 41] For dilute dispersions of spherically small nanoparticles, the total extinction cross section (C_{ext}) can be expressed by equation 2.8:[14, 41]

$$C_{ext} = \frac{24\pi^2 R^3 \varepsilon_m^{3/2}}{\lambda} \frac{\varepsilon''}{(\varepsilon' + 2\varepsilon_m)^2 + \varepsilon''^2}$$

2.8

Here, R is the radius of the nanoparticles, λ is the wavelength of the incident radiation, ε' and ε'' are the frequency dependent real and imaginary party of the dielectric function of the material and ε_m is the dielectric constant of the surrounding medium. The influence of the surrounding medium is usually related to its refractive index, ε' is fairly constant in the UV-Vis regime and a maximum in the absorption will occur when $\varepsilon' = -2\varepsilon_m$.[14, 40, 41] This is assigned to a surface Plasmon. Further, the width and intensity of the plasmon band can be determined by ε''. For many metals, such as Pb, In, Hg, Sn, and Pt, ε' has a negative value, whereas the ε'' -values are positive.[41] Thus, the plasmon bands of these metals are found in the UV-regime. As a result, the colloids will be of brown color and the absorption spectra appear flat and featureless. For coinage metals, such as Au, Ag, and Cu, both ε'' and ε' vary with wavelength in this spectral

regime and interband (d-d) transitions accompany the plasmon resonances. This pushes the plasmon bands into the visible part of the electromagnetic spectrum. In general, the plasmon bands of Au and Ag having particle size below 20 nm, lie close to 520 nm and 400 nm, respectively.
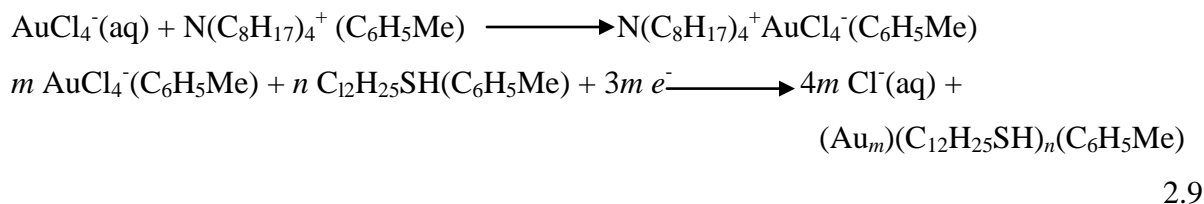
Surface plasmon is quite sensitive to particle size and shape. Kreibig et al.[42] explained the relation between the breadth and intensity of the plasmon band by the fact that the plasmon bandwidth has 1/R dependence, where R refers to the radius of the particle. When the diameter of the particles become smaller than the mean free path of the conduction electrons (i.e. below approximately 3 nm) there is electron scattering at the particle boundaries resulting in broadening and damping of the surface plasmon. Thus, the surface plasmon band for small particles may disappear completely.[43] The size effects for smaller nanoparticles are known as "intrinsic size effects".[38] In the case of particles larger than 25 nm, there is an increase in the bandwidth with increasing particle size. These changes are, however, ascribed to retardation effects as well as the involvement of higher order multipoles, which are also called "extrinsic effects". The surface plasmon resonance shows a red-shift in the extrinsic size-regime with a corresponding change in color of the colloidal solution.

Among the metallic nanoparticles, the work presented in this thesis is performed on gold, silver, and platinum nanoparticles. Thus, only gold, silver, and platinum nanoparticles, syntheses, optical properties, and ligands that can be used to stabilize the nanoparticles are discussed in the next Sections.

2.2.4. Gold nanoparticles

Gold nanoparticles have emerged as a new field of research in the domain of colloids and surface science, which was initiated by Michael Faraday's work.[33] He found that the color of the Cassius ruby-red is due to the gold nanoparticles. Richard Adolf Zsigmondy[44] prepared first gold colloidal solutions by reducing gold chloride by formaldehyde in the presence of weakly alkaline solutions. After Faraday's work; Richard Adolf Zsigmondy used phosphorus to reduce the gold chloride instead of formaldehyde, which resulted in fine gold divisions in molecular

size. Later, the synthesis of gold particles was developed by many group using chemical methods. Since particles prepared in the solution phase have the tendency to aggregate, it is necessary to protect the particles using surfactants or stabilizers. The citrate method was first pioneered by Turkevich et al.[45] and later it was simplified by Ferns.[46] Where the gold salt was reduced by sodium citrate which also acts as a stabilizer Brust et al.[47] developed a phase transfer method to prepare gold nanoparticles in organic solvents. The reaction scheme involved in the two-phase system is shown in reaction 2.9. The two-phase redox reaction is carried out by using a redox agent (reducing agent) in the adjoining agent. Here, dodecanethiol is used as a stabilizer and sodium borohydride is used as the reducing agent, which acts as a source of electrons.

$AuCl_4^-(aq) + N(C_8H_{17})_4^+ (C_6H_5Me) \longrightarrow N(C_8H_{17})_4^+ AuCl_4^-(C_6H_5Me)$

$m\ AuCl_4^-(C_6H_5Me) + n\ C_{12}H_{25}SH(C_6H_5Me) + 3m\ e^- \longrightarrow 4m\ Cl^-(aq) +$

$$(Au_m)(C_{12}H_{25}SH)_n(C_6H_5Me)$$

2.9

The size of the resulting dodecanethiol-stabilized gold nanoparticles is in the range of 1-3 nm and these particles can be easily redissolved in nonpolar solvents. In general, thiols are excellent stabilizers for capping or stabilizing gold nanoparticles owing to the strong Au-S bond. Other than thiols,[8, 10, 20, 32, 47-49] amines,[20, 48, 49] phosphines,[20, 48] carboxylates,[20, 49] and polymers[20, 49] have been successfully used as stabilizers. Other than stronger reducing agents (sodium borohydride[20, 47-49] and lithium borohydride[20, 38]), some weaker reducing agents, such as amine borane complex can also be used as reducing agents. The weaker reductant can also control the growth of the particles.[50] Thus, the size of the particles can be controlled by using appropriate stabilizers and reductants. Another way to prepare monodisperse nanoparticles is the so-called digestive ripening method, by refluxing the polydisperse particles with an excess of ligands. This result in relatively narrow size distributions.[51] The stabilizer can be easily exchanged by other ligands using ligand exchange techniques which are discussed in greater detail in Section 2.4. The schematic representation of the ligand exchange reaction is shown in Scheme 2.1. The ligands bound on the particle surface can be exchanged by adding an excess of appropriate

ligands, which leads to nanoparticles that are decorated and stabilized with the desired ligands.[20]
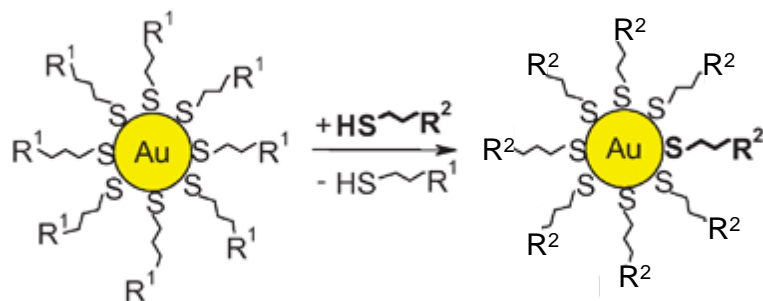
Scheme 2.1: Ligand exchange reaction on gold nanoparticles.

As described above in Section 2.2.3, the optical properties are strongly dependent on the size and shape of the particles, as can be quantified by Mie theory. Figure 2.5 shows a photograph of gold nanoparticles (spheres) of different sizes (4-40 nm), as obtained from transmission electron microscopy images (TEM) ((a(-(e))[52] and extinction spectra of gold nanoparticles of 2.5, 4.6, 15, 60, and 120 nm (f).[15] The photograph shows that the color of the nanoparticles changes from brown to red and finally to violet as the size changes from 4 nm to 40 nm. This is due to the change in surface plasmon band, which shifts as a function of particle size. The reasons for this shift and changes in the surface plasmon band are explained in Section 2.2.3.
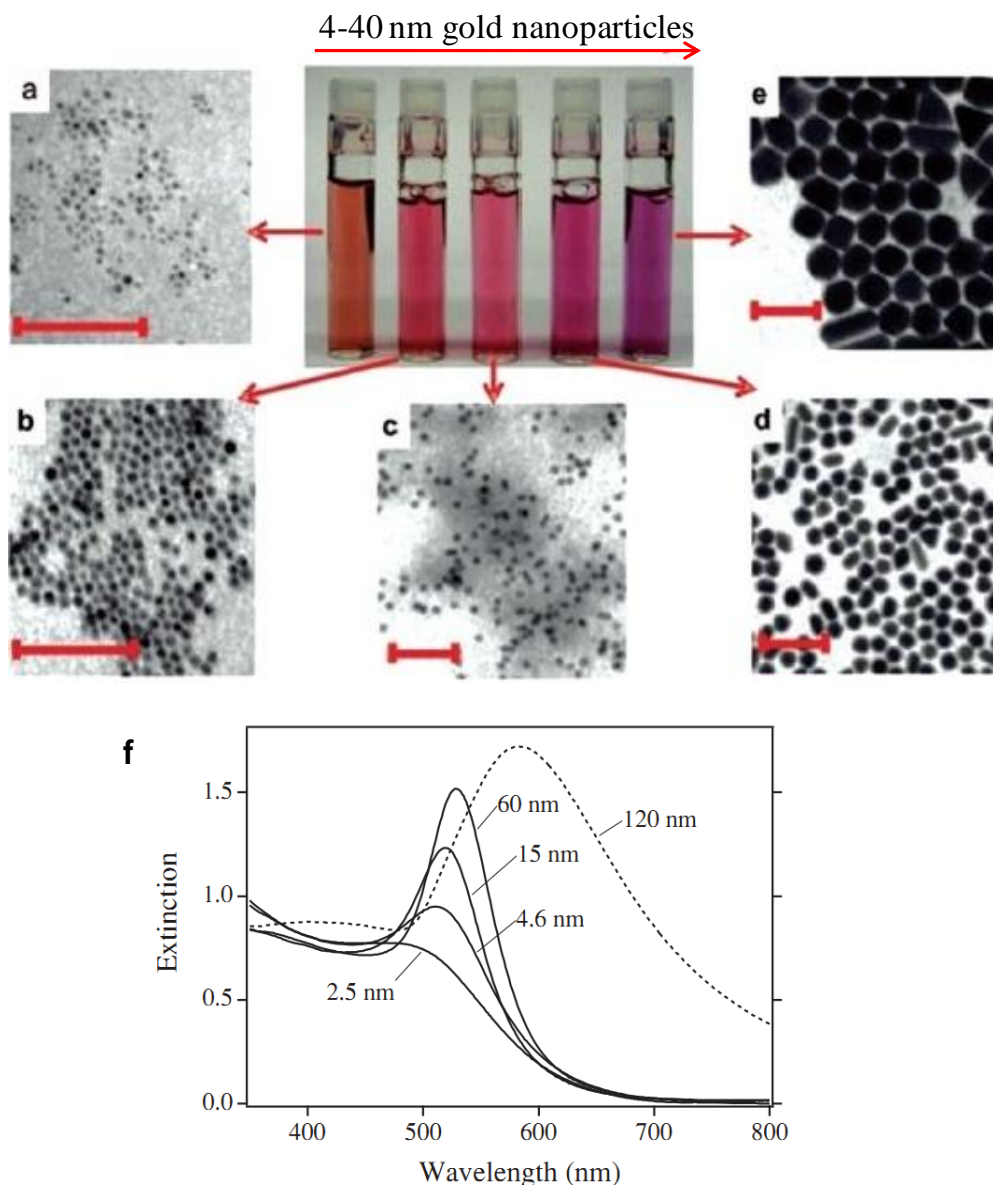
Figure 2.5: Photographs of aqueous solutions of gold nanospheres as a function of increasing dimensions, where the particle size varies from 4 nm to 40 nm. Corresponding TEM images of the nanoparticles are shown in (a)-(e), where all scale bars correspond to 100 nm. (f) Extinction spectra for different sizes (2.5, 4.6, 15, 60, and 120 nm) of gold particles in aqueous solution with a concentration of approximately 10^{-4} mol/L for each sample.[15, 52]

2.2.5. Silver nanoparticles

As with gold nanoparticles, silver nanoparticles also attracted significant attention due their applications in optics,[53] their use as substrate for surface enhanced Raman spectroscopy (SERS),[54] and in biological field as antibacterial agents.[55] Many variations of the methods to prepare silver nanoparticles have been developed. Nearly monodispersed silver nanoparticles can be prepared via the reduction of silver nitrate or silver acetate.[48] The reductant can be sodium citrate,[56] $NaBH_4$,[57] potassium bitartarate, dimethyl formamide, or alcohols.[48] The reduction of silver nitrate ($AgNO_3$) by trisodium citrate is shown below as reaction 2.10. When silver nitrate is dissolved, it dissociates into the solvated ions Ag^+ and NO_3^-. In order to reduce the silver ions it has to receive an electron from a donor, which comes from sodium citrate. After a silver germ has been formed it starts to grow further and continues the growth until an equilibrium between the final nanoparticles is reached, which is evident from the color changes to pale yellow.[56]

$$4Ag^+ + C_6H_5O_7Na_3 + 2H_2O \longrightarrow 4Ag^0 + C_6H_5O_7H_3 + 3Na^+ + H^+ + O_2 \uparrow \qquad 2.10$$
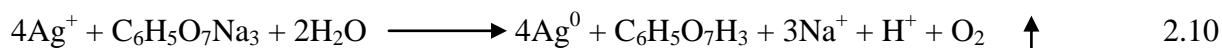
Long-chain alkanethiols are the most common stabilizers for silver particles. However, other than thiols, amines, carboxylic acids, and polymers have also been employed to stabilize silver nanoparticles.[48] Silver nanoparticles can be prepared by using two-phase syntheses also where the silver ions are transferred to the organic phase by hexadecanesulfonic acid. In the organic phase the addition of dodecanethiol, acting as a stabilizer, and subsequent addition of sodium borohydride, leads to silver nanoparticle formation, where the particles are brown in color.[57] One can also prepare monodisperse silver nanoparticles by using digestive ripening concepts.[58] In a first step the particle formed by reduction of silver nitrate using sodium borohydride results in polydisperse particles. The resulting polydisperse nanoparticles are subjected to reflux with an excess of ligands leading to monodisperse particles.[58] Figure 2.6 shows that the size distribution of the particles gets relatively narrowed after such digestive ripening process.
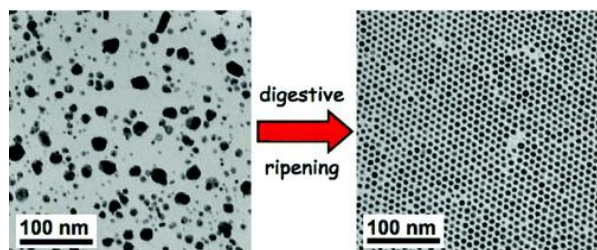
Figure 2.6: Transmission electron images of silver nanoparticles before (left) and after digestive ripening (right).[58]

Similar to gold nanoparticles, silver nanoparticles have also specific surface plasmon bands, which are shape or size sensitive. In Figure 2.7 the conversion of triangular nanoplates into round nanoplates under UV radiation are shown.[17] Upon UV radiation of the silver triangular nanoplates, the color changes from cyan to blue, purple, red, and finally yellow and thus the plasmon band shifted from 871 nm to 450 nm (see Figure 2.7).[17]
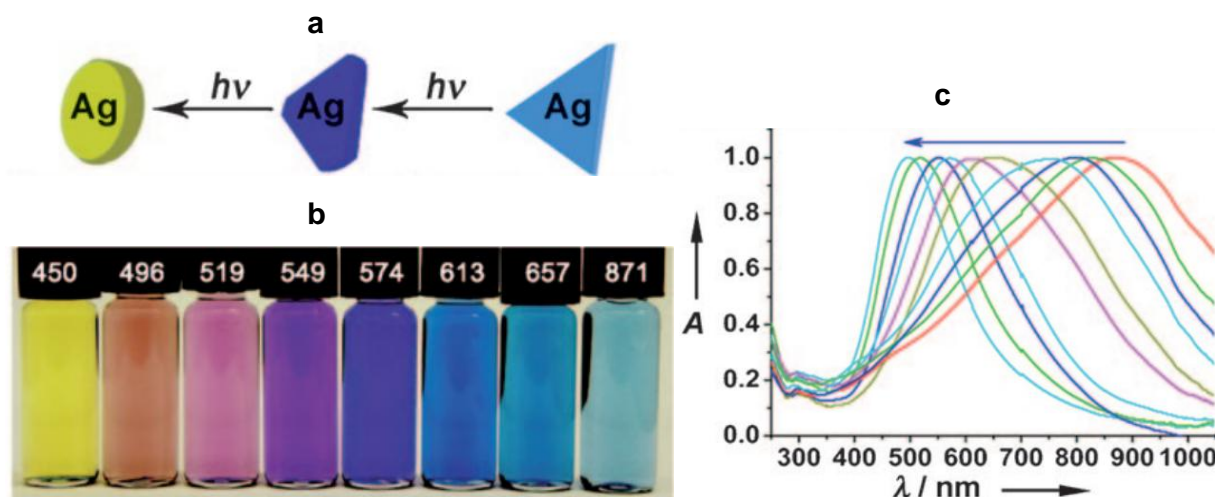
Figure 2.7: a) Illustration of changes in particle from triangular nanoplates to round nanoplates upon UV radiation. The photographs (b) and extinction spectra (c) indicate that the shift in the plasmon band occurs from 871 nm to 450 nm as the shape changes from triangular to round shape.[17]

Peng et al.[16] demonstrated that there are size-dependence changes in surface plasmon resonance for silver nanoparticles. As shown in Figure 2.8 (A) the surface plasmon resonance band exhibits

an exceptional behavior: as size decreases from ≈ 20 nm in diameter it initially blue-shifts but then it turns to a strong red-shift for ≈ 12 nm particles. Further, this spectral shift in plasmon bands is confirmed by theoretical analyses, as well.[16] The reason for this shift is explained using Mie theory model, considering silver nanoparticles of icosahedral shape (see Figure 2.8 B) composed of a core with a diameter d, which has a thickness of the surfactant layer s and a thickness of the silver outer layer t. The electron conductivity in the outer layer of silver atoms is assumed to be lowered when compared to that of the inner silver atoms. This is because the silver atoms in the outer layer involve a partial participation in the chemical bonds between the surface and the surfactants stabilizing the particles. The lowered electron conductivity in the outer layer leads to a red-shift of the plasmon band.[16]

Figure 2.8: A) Size-dependent absorption spectrum of silver nanoparticles dispersed in chloroform. B) Illustration of the theoretical model: d represents the diameter of silver nanoparticles, t is t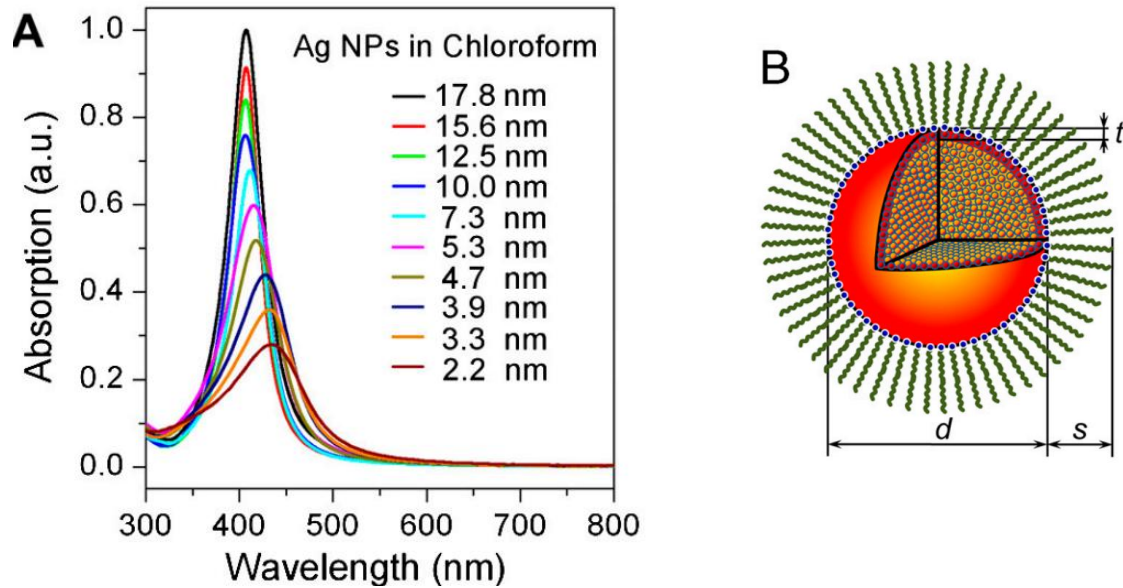he thickness of the outermost atomic silver layer with lowered conductivity, and s is denoted as the thickness of the surfactant layer.[16]

2.2.6. Platinum nanoparticles

Platinum nanoparticles plays an important role in a wide variety of catalytical process and for fuel cells applications.[59-62] Platinum nanoparticles deposited on carbon nanotubes show excellent dehydrogenation properties.[63] The usual technique for the synthesis of platinum nanoparticles is the chemical reduction of chloride metal salts with thiols,[48, 59, 60] polymer,[48, 60] amines,[49, 60, 63] alkyl isocyanides,[48] and cyclodextrins,[48] which also act as stabilizers. The preparation can be performed by one-phase[61] or two-phase[59] methods using sodium borohydride[48, 59, 61] or lithium triethylborohydride as reductants.[61] Usually, platinum nanoparticles will be in brownish black or brown color.[59] Platinum nanoparticles of different shapes can be prepared by varying the ligands,[18] the ratio of ligand to metal precursor,[64] and by using different types of metals salts.[65] Figure 2.9 shows platinum nanoparticles of different shape, which are prepared for catalytic and electrocatalytic applications.[60] The TEM images of platinum nanoparticles are shown, where (a) tetrahedrons, as synthesized by reducing the metal using hydrogen and sodium polyacrylate used as stabilizers, (b) octahedron shaped platinum particles, (c) cuboctahedrons prepared by reducing platinum precursor with high concentration of sodium borohydride, and (d) cube shaped particles, which are prepared using low concentration of sodium borohydride.[60]
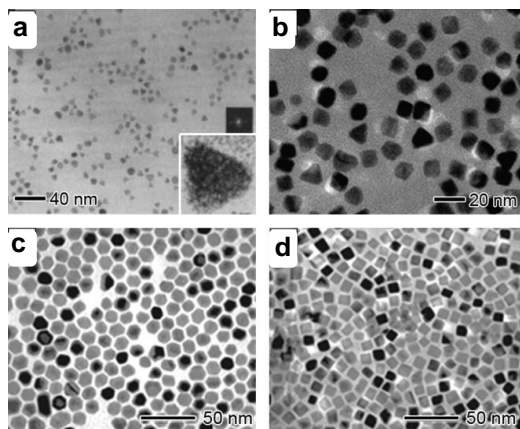

Figure 2.9: Transmission electron images of platinum nanocrystals in the polyhedral shapes: (a) tetrahedrons, (b) octahedrons, (c) cuboctahedrons, and (d) cubes.[60]

In a detailed review, Chen et al.[60] presented different types of synthetic procedures of platinum nanoparticles with different shapes that can be used for catalytic properties. Several different methods have been reported to control the shape of the particles.[18, 60, 64, 65] However, the detailed mechanism of the formation of particles is not well understood. Petroski et al.[19] suggest a shape-controlled growth mechanism, where the difference in growth rate of the crystal lattice faces {100} and {111} is considered. These authors explain the growth mechanism by using time dependent shape changes, as observed during transmission electron microscopic measurements. The growth mechanism is shown as Figure 2.10. It is based on the fundamental face-centered cubic lattice of platinum, where the atoms are defined to be at the edges of the unit cell. The connection of all 13 atoms forms a truncated octahedron shaped cluster, which is bound by eight {100} and six {111} planes. If the growth rate (G) of the {111} plane ($G_{\{111\}}$) is similar that of the growth rate of the {100} plane ($G_{\{100\}}$), the area ratio between these two planes remains constant. This result in the formation of larger truncated octahedron shape nanoparticles (see Figure 2.10 in the first row). If $G_{\{100\}} \gg G_{\{111\}}$, the {100} facets will vanish, forming octahedral shape nanoparticles, as shown in Figure 2.10 in the middle row. On the other hand, as shown in Figure 2.10 in the last row, where $G_{\{100\}} \ll G_{\{111\}}$, the {111} facets will vanish, forming cubically shaped nanoparticles.
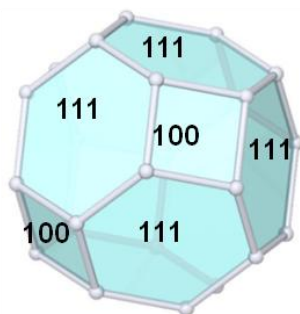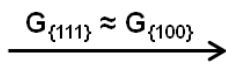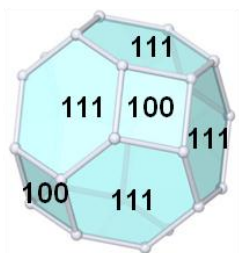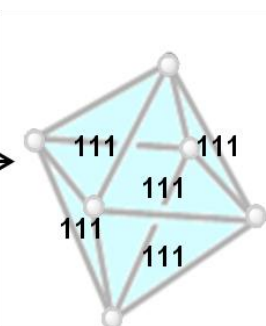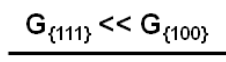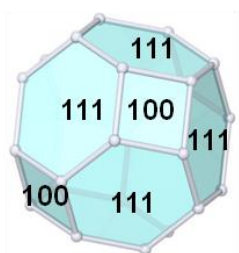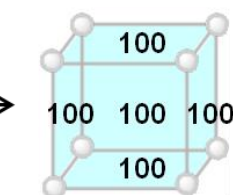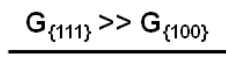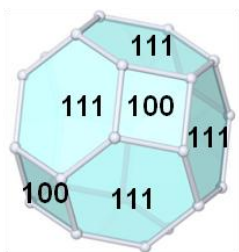
Figure 2.10: Schematic representation of the shape controlled growth mechanism of platinum nanoparticles. The figure is redrawn by using the idea from Petroski et al..[19]

2.3. Synthesis of ligands for functionalization of nanoparticles

As explained in Sections 2.2.4, 2.2.5 and 2.2.6, the properties of nanoparticles are highly dependents on the ligands, which are used to stabilize the nanoparticles. The synthesis of ligands also includes a variety of reactions as that of nanoparticles preparations and hence here only the essential reactions, which are relevant for the present thesis, are presented below. This includes thiol and amine ligands.

2.3.1. Thiol ligands

The thiols are sulfur analogs of alcohols.[66] Thiols can be synthesized using a variety of reactions. Here, only a brief overview will be given in order to elucidate the chemical pathways involved in the Sections 3.2.1 and 4.1.1.
Thiols are generally prepared starting from alkyl halides with alkali-metal hydrosulfides.[66] Thiols can be prepared by hydrolysis of S-alkyl isothiuronium salts, as well.[66, 67] This involves the reaction between thiourea and alkyl halides, as shown in reaction 2.11:[66]

$$RX + (NH_2)_2C=S \longrightarrow [RSC(=NH_2)NH_2]^+X^- \xrightarrow{\text{NaOH}} RSH + NaX + H_2O + NH_2CN$$

R = alkyl   2.11
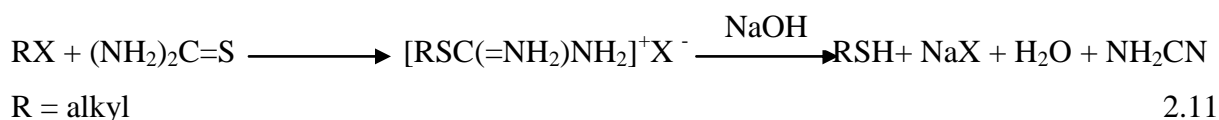
Further thiols can be prepared from thioesters (SAc) by reducing ester using lithium aluminium hydride (LiAlH$_4$).[68] The thioesters are either prepared from alcohols[68, 69] or from corresponding halides.[70] The alcohols easily convert to alkyltosylate group by treating alcohols with tosylchloride followed by substitution of tosylate group to thioacetate derivatives using potassium thioacetate.[69] In another way the thioacetate derivatives can be synthesized directly from alcohols is the Mitsunobu reaction.[68, 71] The thiol compounds presented in this work are mostly prepared by using the Mitsunobu reaction method which is followed by a reduction using LiAlH$_4$.[68]

In addition to the simple thiol compounds, which have only a single thiol group, multivalent thiol compounds with more than one thiol group are also known.[68, 71] The thiol groups of multivalent ligands can bind simultaneously on a substrate.[32] The interest in syntheses of multivalent compounds has significantly increased recently because of the enhanced bond strength to metal cations, as compared to mono-thiol derivatives.[32] The disulfides also bind to nanoparticles and results in a better stabilization than the monovalent ones.[72] Further, the synthesis of thiol functionalized multivalent ligands and their stabilization on nanoparticles are discussed in the thesis of Andreas Hofmann.[73]

2.3.2. Amine ligands

In the most simple way the substitution of hydrogen in ammonia results in alkyl amines; substitution with one alkyl group produces primary amines (RNH_2), with two alkyl groups secondary amines (RR'NH) are formed, and tertiary amine (RR'R''N) have three alkyl groups. In general, amines can be prepared by alkylation of ammonia or its derivatives,[66, 74] reductive methods and degradative methods.[66]

The reactions between alkyl halides with sodium amide in liquid ammonia produce primary, secondary, and tertiary amine as shown in reaction 2.12:[74]

$$C_5H_{11}Br + NaNH_2 \longrightarrow C_5H_{10} + NaBr + NH_3$$
$$C_5H_{11}Br + NaNH_2 \longrightarrow C_5H_{11}NH_2 + NaBr$$
$$2C_5H_{11}Br + 2NaNH_2 \longrightarrow (C_5H_{11})_2NH + 2NaBr + NH_3$$
$$3C_5H_{11}Br + 3NaNH_2 \longrightarrow (C_5H_{11})_3N + 3NaBr + 2NH_3 \qquad 2.12$$
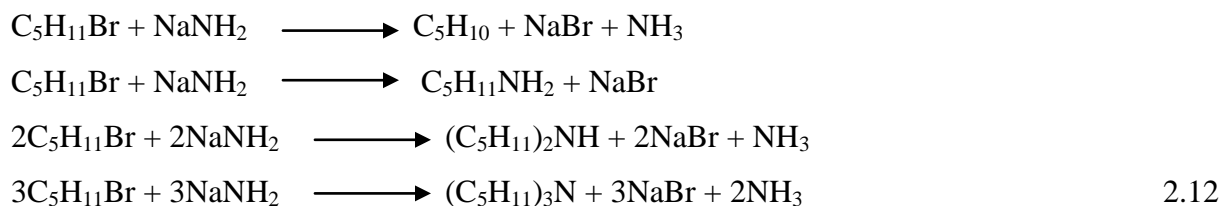
Amines can be prepared by using Gabriel regents, where N-alkylation and cleavage steps take place.[66, 75] The reaction between potassium phthalimide and an alkyl halide form the corresponding N-alkylated phthalimide, which is cleaved to give a primary amine. The reduction of nitriles with $LiAlH_4$ in ether or tetrahydrofuran also yields amine compounds as well as the reduction of azide substrates with $LiAlH_4$. By Staudinger reaction,[76] when azides react with phosphines form iminophosphorane as an intermediate, which is followed by hydrolyzing the

25

intermediate will yield amine compounds and phosphine oxides as a side product. In another case the azides can be directly reduced to the corresponding amine by using LiAlH$_4$ in tetrahydrofuran.[77]

Multivalent amine ligands also exist, but only few reported synthesis procedures are found in the literature on multivalent amine ligands.[32, 77] Similar to thiols, the amino groups in multivalent amine ligands can also bind simultaneously to substrates.[32] Multivalent amine functionalized ligands are used for the first time in this thesis to stabilize nanoparticles.

2.4. Ligand exchange reaction on nanoparticles

Generally, nanoparticle surfaces are covered by the ligands which prevents the nanoparticles core from aggregation.[21, 78-82] However, the bonds between the inorganic nanoparticle surface and the stabilizing ligands, for example an electron donating end group ligand molecule such as thiol, amine or phosphine, undergoes dynamic binding and unbinding processes. This may lead to aggregation of the particles.[20] In order to improve the stability of given nanoparticles, the ligand molecules on the surface can be exchanged by other ligands can possibly provide new properties or functionality to the particles.[20, 79] Thus in most cases, the incoming ligand molecule binds more strongly to the inorganic nanoparticle surface.[20, 78, 80] Ligand exchange reaction is a well-known method to exchange bound ligands on nanoparticles by simply mixing the free ligands with nanoparticles, which results in a replacement of the bound ligands by incoming ligands (see Figure 2.11). Thus, ligand exchange is a simple and versatile approach to tune the ligand shell on nanoparticles. Further the protecting ligands are exposed to solvents and external reagents and because of this several properties of the nanoparticles, such as solubility as well as chemical and physical properties will differ.[21, 44, 78-82] After the exchange of ligands they may be used as biosensors, catalysts, or for optoelectronics applications.[21] Glycol ligands stabilized on platinum particles after exchange with phosphine ligands show an improved electrocatalytic activity.[78, 80] The particle size can also be adjusted by exchanging the ligands bound on particles.[79]
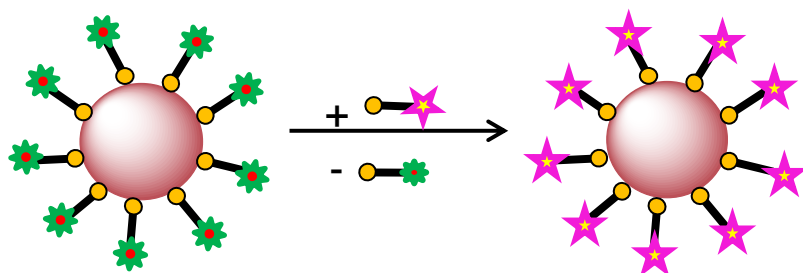
Figure 2.11: Schematic diagram of a ligand exchange reaction on nanoparticles.

The mechanism of ligand exchange was studied in detail by Murray[24, 25] and subsequently many other groups also investigated such processes. Thiols have been exchanged by other thiols,[26, 27, 83-85] phosphines with thiols,[13, 86-90] dimethylaminopyridine by thiols,[91] and amines by thiols.[72, 78, 92] One important aspects of ligand exchange is the morphology and size of the nanoparticles. Their surface has different sites (two defect and one non-defect sites), i.e. vertices (corner sites) and edges are defects sites where as terrace (face sites) are known as nondefect sites (see Figure 2.10. a).[24, 25, 27, 72, 83] Figure 2.12. (b) indicates the processes that take place during ligand exchange reactions: (i) fast ligand exchange at edge and vertex sites, (ii) slower exchange at near-edge and at terrace sites, where near-edge and interior sites are distinguished, and (iii) migration between the surface sites. [24, 25, 27, 72, 83]
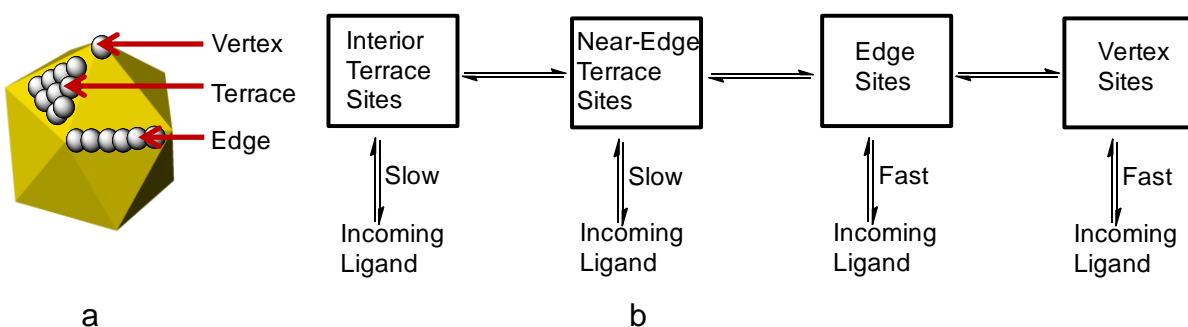
Figure 2.12: (a) Schematic diagram representing the various nanoparticles surface sites, assuming nanoparticles of icosahedral shape, which contain different ligand binding sites on terraces, edges, and vertices. (b) Model for the processes of ligand exchange reactions on nanoparticles (adapted from Hostetler et al.[25]).

These different surface sites have different electron densities and steric behavior hence they will have different reactivity.[24, 83] It is found that the rate of ligand exchange reaction decreases as the chain length and the steric bulk of the initial protecting ligand shell is increased.[25] Further, due to the variation in surface curvature of differently sized nanoparticles, the reactivity may also differ.[93, 94] For example, Kell et al.[93] observed an increase in reaction rate with decreasing the particle size.[93]

Generally, ligand exchange studies were done using NMR, EPR. Specifically, the ligand exchange reaction of aromatic ligands on nanoparticles were studied using NMR,[13, 24, 25, 83, 93] whereas the exchange of disulfides, free radicals, amines, and sulfides are studied by using EPR.[26, 95] The kinetics of exchange of phenylethanethiolate ligands (PhC$_2$S) on gold clusters Au$_{140}$(PhC$_2$S)$_{53}$ by para-substituted arylthiols (*p*-X-ArSH) were measured by ^{1}H-NMR.[83] The exchange rate increased rapidly at an initial stage and gradually slowed down when the equilibrium state was reached. The rate constants normally increase for ligands with electron-withdrawing substituent (X = NO$_2$ and 4-OH). At longer reaction times, the ligand exchange reaction takes place at non-defect (terrace) as well as defect sites (vertex and edge) and the reaction rate is higher for thiols with electron-donating substituent. Murray and co-workers[24] explained the core size effect of ligand exchange using ^{1}H-NMR by comparing the exchange kinetics of phenylethanethiolate ligands (PhC$_2$S-) of (Au$_{38}$(SC$_2$Ph)$_{24}$ and Au$_{140}$(SC$_2$Ph)$_{53}$ clusters by p-substituted arylthiols (*p*-X-Ar-SH), where X = NO$_2$, Br, CH$_3$, OCH$_3$, and OH. The chemical reactivity of differently sized clusters is almost independent on their size, since vertices and edges are contained in all these species. The only difference with increasing size is that larger terrace sites occur, where the reaction rate is slower than at the other sites.

Ionita et al.[26, 95] measured the ligand exchange reaction using EPR spectroscopy. They also found that the reactions are more active at the defect sites than the non-defect sites. These EPR studies indicate that triphenylphosphine bound particles were found to be more reactive than the thiol bound and disulfide bound ones.[26] Moreover, the binding of disulfides was explained by EPR measurements,[26, 95] where the disulfides do not adsorb close to each other on the surface of the nanoparticles. Typically, by using NMR and EPR, acquisition times of $\geq$ 15 s per spectrum were required and resulted in time intervals of 1-5 min between single measurements. This limits the accessible time regime for kinetics studies to fairly slow ligand exchange processes. This is even truer, since the initial stage of these processes is required to derive the mechanism of ligand exchange. Hence, under these situations optical spectroscopy would be the more suitable method to probe fast ligand exchange processes. For example, Montalti and co-workers monitored pyrene derivative exchange using different concentrations of dodecanethiol by time resolved fluorescence spectroscopy for the first time.[27] Key to this approach is the quenched fluorescence of particle-bound dye molecules, which completely recovers when they are exchanged against

thiol ligands. This technique is versatile for the investigation of fast ligand exchange reactions involving changes in optical properties of reactants and products. This provides a temporal resolution in the sub-second regime. In another study by Uznański et al.[72] used fluorescence spectroscopy to investigate the rates of adsorption of disulfides by exchange of amines bound on nanoparticles and desorption of disulfides by exchange with incoming dodecanethiol. The results show that the rates of pyrene disulfides exchange on gold nanoparticles is higher for desorption compared to chemisorption.[72]

2.5. Kinetics studies for ligand exchange on nanoparticles

The detailed understanding of the mechanism of ligand exchange is essential for tuning the ligand shell on nanoparticles and its kinetics. In general, the reaction kinetics provides reaction mechanisms. Chemical reaction kinetics deals with the rates of chemical processes which may be broken down into a sequence of one or more reactions yielding the products. Consider a hypothetical one step reaction as shown below in equation 2.13,[96, 97] leading to the formation of the products (A + BC) from the reactants (AB + C). The reactants (AB and C) have to pass through a transition state between the reactants and the products. The transition state occurs at the maximum energy of the reaction coordinate and acts as an energy barrier of the reaction. If a reaction processes proceed in a single step with a single transition state, as shown in the Figure 2.13, then this is known as an elementary reaction.

The Hypothetical one-step reaction:

$$AB + C \longrightarrow A + BC \qquad\qquad 2.13$$
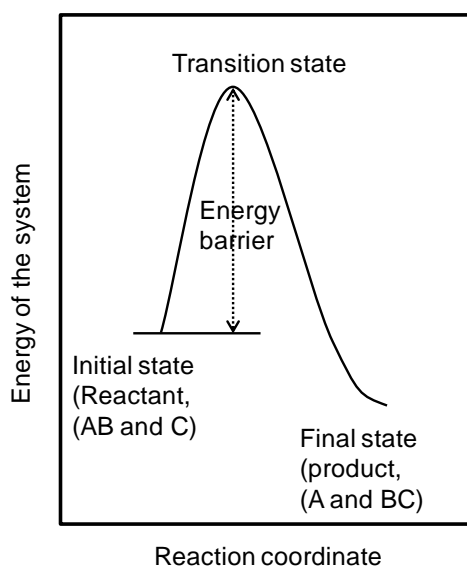
Figure 2.13: Schematic diagram for hypothetical one-step reaction. Taken from Connors et al.[97]

This shows that the rates of reactions will depend on the energy barrier of the reaction path. The main task in chemical kinetics is essentially to establishing quantitatively a suitable kinetics scheme; where the overall reaction is to be decomposed into its elementary reactions. This kinetics scheme determines variables, which are involved in the rate studies, such as temperature, pressure, reactant concentrations, activation energy, and surface area.[96, 97]

The mechanism of the reaction[97] can be broadly classified either into homolytic (free radical) or heterolytic (ionic) reactions. Further one might distinguish substitutions, additions, and eliminations. If a reaction involves two reactants, one has to be considered as a substrate and other one as the reagent. The reagents may be nucleophiles which is electron rich, either bases or reducing agents or electrophiles which are electron deficient. These are either acids or oxidizing agents. Reagents may also be classified in terms of their hardness or softness.[97] Hard acids are small, with a high positive charge and of low polarizability and soft acids are bulky and polarizable. A hard base has high electronegativity and low polarizability and a soft base is easily polarizable. The hard and soft acid-base (HSAB) concept has been particularly useful in understanding substitution reactions.[97] The reaction types are classified accordingly by a class and reagent type. Thus, a nucleophilic substitution (S_N) is a substitution reaction by a nucleophilic reagent. Further, the substitution can be classified into two types as S_N1 and S_N2 which are known as unimoecular and bimolecular, respectively, as the order of the reaction. The molecularity is the number of reactant molecules included in the transition state. S_N1 reaction takes place in two-steps and only the substrate is included in the transition state and not the reagent (dissociative mechanism). In contrast, S_N2 are one-step reactions; the reactants, the substrate, and the reagents are present in the transition state (associative mechanism). The rate of reaction depends on the reactant and substrate concentrations (cf. textbooks written by Connors et al.[97] and Atkins et al.[96]).

Consider the reaction:
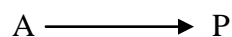
$$A \longrightarrow P \qquad\qquad 2.14$$

The rate of an elementary reaction is proportional to the molar concentrations of the reactants, raised to the power of their stoichiometric coefficients. Thus, for the reaction 2.14, the rate of the reaction is

$$v = kc_A^a \qquad\qquad 2.15$$

Where k is called rate constant and is independent of the concentrations of reactants [A] but may depend upon factors such as the temperature, pressure, and the solvent. The power a is order of the reaction with respect to the reactant A. The units of the rate constant depend upon the reaction order.

For a general unimolecular reaction 2.14, where A is the reactant and P is the product, the reaction rate expression for a first order reaction is

$$-\frac{d[A]}{dt} = k[A] \qquad\qquad 2.16$$

This shows that the reaction rate is proportional to the concentration of a single reactant raised to the first power.

Separating the variables in equation 2.16 and integrating the resulted equation yields

$$\ln\frac{[A]}{[A]_0} = -kt \qquad\qquad 2.17$$

$$\log\frac{[A]}{[A]_0} = -\frac{kt}{2.303} \qquad\qquad 2.18$$

$$[A] = [A]_0 e^{-kt} \qquad\qquad 2.19$$

Therefore for a first order reaction, a plot of ln[A] or ln[A]/[A]$_0$ against time is linear. The plot should be linear up to a conversion of about 90% and the first order rate constant can be obtained from slope. A first order rate constant has the dimension time^{-1}, the usual unit being second^{-1}.

The integrated rate laws and the units of rate constant for 0, 1st, pseudo first order, 2nd and nth order are shown in Table 2.1. For zero order, (first row in the Table 2.1) the rate of the reaction is independent of the concentration of reactant, so that the rate of the reaction is constant. When the limiting reactant is completely consumed, the reaction stops abruptly. For first order, (second row in the Table 2.1) the reaction rate is proportional to the concentration of a single reactant (A) which is raised to the first power. The pseudo first order reaction which is shown in third row of the Table 2.1, the concentration of e.g. A is considerably larger than B. Then, [A] will remain almost constant during the reaction. Thus, the rate of the reaction is only proportional to the concentration of B. The rate of a second order reaction (see fourth row in Table 2.1) is proportional to either the concentration of a reactant squared, or the product of concentrations of two reactants.

Table 2.1: Summary of the rate laws and its units for reaction orders 0, 1, pseudo first, 2, and n.

Order	Reaction	Integrated Rate Law	Units of Rate Constant
0	A $\longrightarrow$ P	$[A] = [A]_0 - kt$	$\dfrac{M}{s}$
1	A $\longrightarrow$ P	$[A] = [A]_0 \cdot e^{-kt}$	$\dfrac{1}{s}$
Pseudo First Order Reaction	A + B $\longrightarrow$ P [A] >> [B]	$k = \dfrac{k\prime}{[A]}$	$\dfrac{1}{s}$
2	A + B $\longrightarrow$ P	$\dfrac{1}{[A]} - \dfrac{1}{[A]_0} = kt$	$\dfrac{1}{M.s}$
nth	A $\longrightarrow$ P	$\dfrac{1}{[A]^{n-1}} = \dfrac{1}{[A]_0^{n-1}} + (n-1)kt$	$\dfrac{1}{M^{n-1}.s}$

For broken reaction, the order of the reaction will be a non-integer typically such reactions will have complex reaction mechanism, complex reaction is a multistep reaction.[97] A complicated rate equation arises largely in the study of complex reactions. Most generally complicated reaction can classified as parallel reactions or consecutive reactions. In parallel reactions a reactant undergoes two or more concurrent reactions to give different products. Parallel reactions are also known as competitive reactions.[97] Consecutive reactions are those in which the product of one reaction is the reactant in the next reaction. Thus consecutive reactions are also known as series reactions, reversible reactions, autocatalytic reaction, polymerization reactions, and chain reactions are can be viewed as consecutive reactions.

In general, most of the reactions rates are sensitive to temperature. Experimentally it has been found that the rate constant of a reaction related to the temperature, which is called as Arrhenius equation.

$$K = Ae^{-E_a/RT} \hspace{6cm} 2.20$$

Where R is the gas constant, T is the absolute temperature, A is preexponential factor and often called as frequency factor, which has units of the rate constant and will vary depending on the order of the reaction, and E_a is the experimental activation energy whose units is commonly expressed in kilocalories or kilojoules per mole. The equation shows, increasing the temperature or decreasing the activation energy will result in an increase in rate of the reaction.

The appropriate methods to study the reaction kinetics are flow method, stopped-flow technique, flash photolysis, quenching and chemical quenching flow methods.[96] NMR,[13, 20, 24, 25, 83, 93, 95, 98] EPR,[20, 26, 95] electrochemical methods,[97, 99] and the fluorescence method[27, 72] are also employed for kinetics study on nanoparticles. The kinetics study on nanoparticles are often carried out by using the ligand exchange reaction.[24, 25, 27, 83] Since, in this thesis, the kinetics study of the binding of multivalent ligands on gold, silver and platinum nanoparticles are carried out using ligand exchange reaction, the kinetics studies on nanoparticles are explained further in greater details.

The kinetics of ligand exchange on nanoparticles is well explained in a review by Caragheorgheopol et al..[20] The ligand exchange reactions has been shown to occur via a

dissociative (S_N1) mechanism.[95] The kinetics of the exchange of hexanethiols on the Au_{140} (gold clusters) by 6-mercapto-1-hexanol were studied by using a thermogravimetric method.[99] The rate of this reaction was found to be of pseudo-first order as the rate of the reaction varies with the incoming thiol (6-mercapto-1-hexanol).[99] In some cases the associative mechanism is involved in the ligand exchange.[25, 27, 83] The kinetics of the exchange of phenylethanethiolate ligands of monolayer-protected gold cluster ($Au_{140}(PhC_2S)_{53}$) by para-substituted arylthiols are described by Murray and co-workers using the NMR technique.[83] NMR measurements shows that the pseudo-first-order rate constants derived from the first 10% of the exchange reaction vary linearly with in-coming arylthiol concentration, implying that the labile ligands exchange in a second-order process, which is consistent with ligand exchange being an associative process. The kinetics study of the ligand exchange reaction using the fluorescence technique by Montalti and co-workers[27] also suggested that the exchange of pyrene derivatives by different concentrations of dodecanethiol undergoes an S_N2-type associative mechanism.

Badijic´ et al.[98] explained that the multivalency can be expressed kinetically. The authors discovered that that the mixing of two-component triply threaded superbundles in solution the formation of the product precedes in a two-step process. The reactions were monitored using NMR and it has been found that the first step is being kinetically favored and the second step is thermodynamically controlled. Further, the kinetic expressions for the multivalency are observed in biological system.[100] This investigation shows that the multivalent interactions require a long time to achieve equilibrium. By this system an extremely long-lived interaction between polymeric ligands and its multimeric receptor is achieved through multiple binding.

2.6. Methods

Several methods are used in this work to characterize the ligands and the ligands stabilized nanoparticles. These methods are explained below in greater detail.

2.6.1. UV-Vis spectroscopy

UV-Vis spectroscopy is the measurement of the wavelength and intensity of the absorption of near-ultraviolet and visible light by a sample. In UV / VIS spectroscopy, particles are irradiated by with electromagnetic radiation in the range of ultraviolet (UV), visible (VIS) and near infrared (NIR) regimes, i.e. approximately between 200 nm and 3000 nm. Ultraviolet and visible light are energetic enough to promote outer shell electrons to unoccupied states. The ultraviolet-visible spectra depend on electronic transitions of the molecules and the origin of ultraviolet-visible absorption can be caused by $\sigma \rightarrow \sigma^*$, $n \rightarrow \sigma^*$, $n \rightarrow \pi^*$, and $\pi \rightarrow \pi^*$ transitions.

Transitions to σ^* orbitals ($\sigma \rightarrow \sigma^*$, $n \rightarrow \sigma^*$) requires high energy radiation of wavelengths less than 200 nm (such as alcohols, amides and water molecules). Vacuum UV or X-ray radiation is necessary to cause $\sigma \rightarrow \sigma^*$ transitions (such as alkanes). Molecules such as water and methanol absorb maximally at 167-184 nm due to $n \rightarrow \sigma^*$ transitions. Transitions to a π^* orbital requires the presence of an unsaturated functional group (chromophore) to supply the π^* orbitals. Radiation in the 200-700 nm range brings about these transitions. The maxima are strongly affected by substituent groups. For instance, molecules with conjugated double bonds, carbonyl groups, carboxyl groups, nitro groups, and azo groups exhibit $n \rightarrow \pi^*$ while molecules such as ethylene groups, acetylene groups, carbonyl groups and azo groups exhibit $\pi \rightarrow \pi^*$.[101]

Inorganic molecules containing double bond, such as nitrate groups, carbonates groups, and nitrite groups absorb in the UV-Vis region. The UV-Vis spectra of transition metals will be similar in appearance to those of organic compounds that are generally comprise a few broad absorption bands with little fine structures. Visible and near infrared region contain weak absorption bands and strong absorption occurs near UV region. The absorption bands corresponds to the energy required to excite an electron from t_{2g} to higher ones e_g energy level.

The energy gap between the two energy levels (t_{2g} and e_g) is relatively small. The magnitude of the splitting of d-orbitals for transition metal complexes depends on oxidation states of metal ions, nature of metal ion, nature of ligands, number of ligands and geometry of ligands. The splitting of the d-orbitals can be calculated using crystal field theory (CFT). The color of transition metal complexes are depends on either d-d transition explained above and also by charge transfer transition. The charge transfer transition can be ligand-to metal charge-transfer (LMCT) transition or metal-to ligand charge transition (MLCT). For this one of its components must have electron donating properties and another must have electron accepting properties.

In this thesis, the concentrations of pyrene thiol ligands and pyrene thiol bound on gold nanoparticles are calculated by comparing the intensities from unknown concentration to those corresponding to the intensities of known concentrations. These are described in greater detail in Sections 4.1.2 and 4.1.3.

For the measurement dilute solutions of pyrene thiol ligands or gold nanoparticles stabilized by pyrene thiol ligands are brought into a glass or quartz cuvette with a known reference sample (solvent) into an optical spectrometer. Then, the cells are irradiated by light of desired wavelength. The concentration of the unknown sample in solution can be determined by measuring the absorbance at some wavelength and applying in the Beer-Lambert Law (equation 2.21).[101]

$$A = \log_{10}\left(\frac{I_0}{I}\right) = \epsilon \cdot c \cdot l$$

2.21

Where A is the measured absorbance, I_0 is the intensity of the incident light at a given wavelength, I is the transmitted intensity, ϵ the molar extinction coefficient (in $l.mol^{-1}.cm^{-1}$), c is the concentration of the solution, and l is the thickness of the cuvette (pathway of the light travelled through the sample). The nanoparticles also can be characterized by using UV-Vis spectroscopy. This is based on a change in the refractive index around the particles which leads to a change in the extinction spectra of the nanoparticles.

The optical properties of the metallic nanoparticles are explained in detail in the Section 2.2.3. Further, the optical properties of gold and silver nanoparticles are described in detail in Sections

2.2.4 and 2.2.5, respectively. The changes in absorption spectrum due to the changes in shape or size of the particle are also explained in detail (see Sections 2.2.3, 2.2.4, and 2.2.5).

2.6.2. Fluorescence spectroscopy

Fluorescence spectroscopy is a spectroscopy by which fluorescence of the samples can be detected and analyzed. For the measurements dilute solutions of fluorophores in a glass or quartz cuvette are taken into the spectrometer. It is the measurement of wavelength and the fluorescence intensity, i.e. emission of light from electronically exicted states of the molecules which occurs upon electronic relaxation. Primarily, the fluorophores absorb ultraviolet light, which excites the molecules to an excited state. The absorption of light by molecules occurs in discrete amounts known as quanta. Thus, the emission also measured in terms of quanta.[102] Figure 2.14[103] shows by absorbing photons, the molecules reach either the first, S_1, or second S_2, excited singlet state.

Excitation can result in the excited molecule any of the vibrational sub-levels associated with the electronic final state. If the molecules reach one of the higher vibrational levels of an excited state S_2 which has excess energy, then the excess of vibrational energy may be lost by collisions and falls to the lowest vibrational level of the first excited state S_1. Thus, almost all molecules occupying higher states S_2 undergo internal conversion (loss of energy in the absence of light emission) and pass from the lowest vibrational level of the upper state to a lower excited state S_1. From this level, the molecule can return to any of the vibrational levels of the ground state S_0, emitting its energy as fluorescence photons, if no dissociative processes compete with this relaxation process. Other relaxation pathways, such as non-radiative relaxation, and intersystem crossing, may also compete with fluorescence emission process. For example, there may be non-radiative relaxation (indicated by the wavy arrow in Figure 2.14) in which the excitation energy is dissipated as heat (vibrations) to the solvent. Further, the excited molecules can also relax by intersystem crossing to a triplet state T_1, which may subsequently reach the ground state through phosphorescence or by a secondary non-radiative relaxation steps. From triplet state T_1 back to excited singlet state and a subsequent transition to the ground state through delayed fluorescence may also take place.
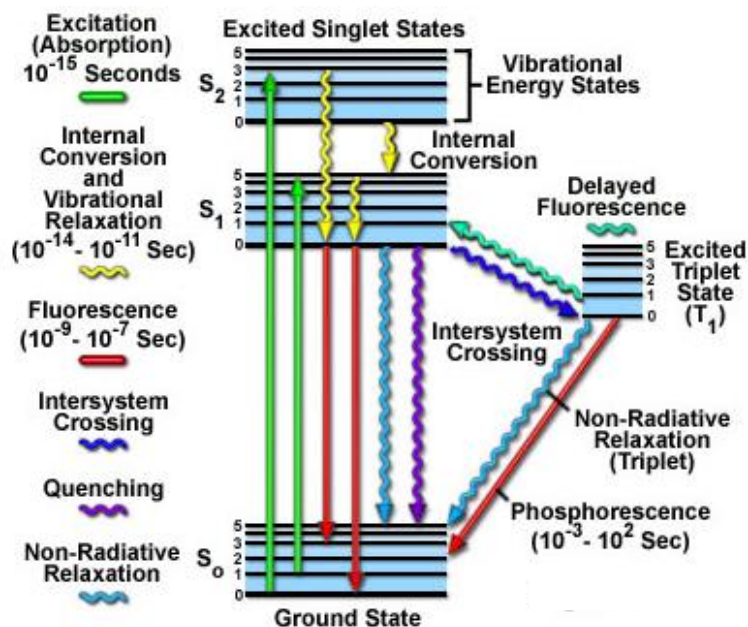
Figure 2.14: Jablonski diagram illustrating different energy levels (S_0, S_1, S_2, T_1) and different processes taking place after the absorption of ultraviolet light by the molecules.[103]

In the excited state undergoes transitions other than the transition to the energy levels S_1, S_2, T_1, the formation of excimers is possible. Typically, excimers are dimers in an excited state, which would not form in the ground state. Due to the high concentration of the fluorophore many solutions manifest such two-bands of fluorescence. The first short-wave fluorescence bands coincide with the emission spectrum of the dilute solution and will be associated with the radiative transition (fluorescence or phosphorescence) reaching the ground state S_0 from S_1. The second long-wave fluorescence band is caused by excimers, which is an associate of the electronically-excited molecule and a ground state one. This dimer after photon emission dissociates into separate molecules and reaches the ground state S_0. The Figure 2.15(a) shows the emission spectra of a pyrene derivative, where specifically this pyrene is used for the kinetics studies in this thesis (see Section 4.3). Figure 2.15(b) shows the emission spectra of pyrenyl-hexadecanoic acid, which is similar to the molecule used in this thesis, at different concentration and clearly reveals that the excimer band appears around 376 nm and decreases with decreasing

concentration.[104, 105] As a result, Figure 2.15 shows the monomer band in the region 377-400 nm and a broad band around 376 nm corresponding to the excimer emission.
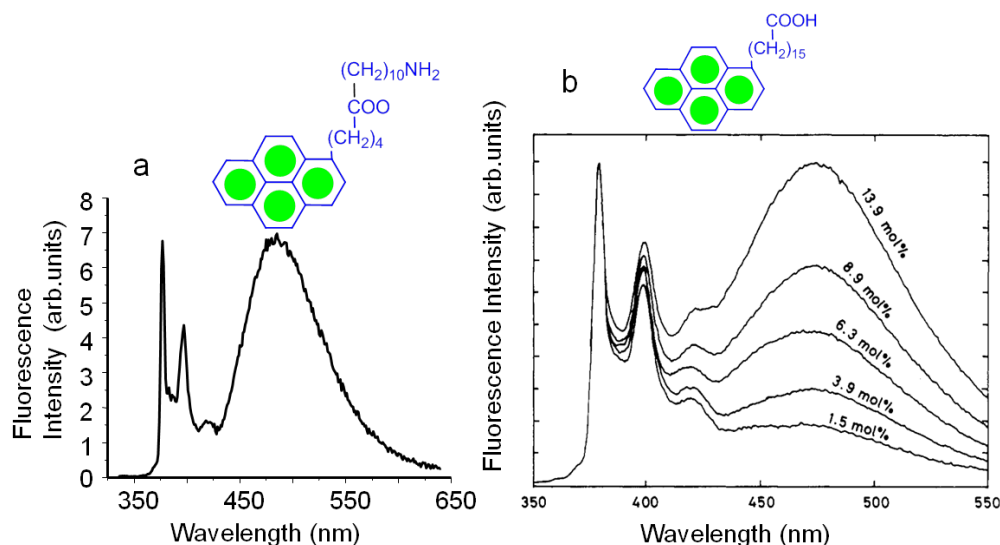
Figure 2.15: Emission spectra (a) of the 4-pyrenebutyl-11-aminoundecanoate at $2 \cdot 10^{-4}$ M concentration and (b) of the 16-(1-pyrenyl)hexadecanoic acid at different concentrations.[105]

Other than excimers, fluorescence quenching is also possible during the excitation of molecules. The decrease in fluorescence intensity is called quenching, which occurs when the excited-state fluorophore is deactivated upon contact with some other molecule in solution, which acts as a quencher. Usually, quenchers can be oxygen, halogens, amines, or electron deficient molecules.[102] The fluorophore reaches the ground state S_0 after the contact with the quencher, as shown by wavy arrow in Figure 2.14 in purple color. Due to this, the molecules are not chemically transformed in such processes. The decrease in fluorescence intensity can be described by the Stern-Volmer equation 2.22:[102]

$$\frac{F_0}{F} = 1 + K[Q] = 1 + k_q \tau_0 [Q]$$
2.22

Where K is the Stern-Volmer quenching constant, k_q is the bimolecular quenching constant, τ_0 is the unquenched lifetime, and [Q] is the quencher concentration. Mainly quenching occurs by a combination of at least three mechanisms, i.e. intersystem crossing or the heavy atom effect, electron transfer or Dexter interactions, and photoinduced electron transfer.[102] By intersystem

41

crossing quenching occur because of heavy atoms, halogens, or oxygen. The molecules reach an excited state due to triplet oxygen, causing the excited singlet state S_1 to transform to the triplet state T_1. From the triplet state it is likely to be either quenched to the ground state by the same quencher (e.g. oxygen) or it returns to the ground state by non-radiative relaxation. Some reports suggest that the oxygen quenching occurs by a mixed mechanism, which includes all the three mechanism.[102, 106, 107] The second mechanism is an electron–exchange mechanism or Dexter interaction, where the electron is transferred from the excited donor to the acceptor.[102, 108] The acceptor then transfers an electron back to the donor. This electron exchange takes place in the highest occupied molecular orbital of the acceptor and thus the acceptor stays in the excited state. This mechanism is similar to FRET (fluorescence resonance energy transfer), where also the energy is transferred from the excited donor to the acceptor. Here, always the donor is a fluorophore and the electron exchange takes place by considering the distance between the acceptor and donor. RET (resonance energy transfer) occurs at large acceptor-donor distance, while the Dexter transfer occur at short donor-acceptor distance.[102] Desce and co-workers[109] explained that pyrene derivatives result in 100% quenching when they are bound on nanoparticles then the other chromophore molecules such as stilbene and diphenyl derivatives. The third mechanism is the photoinduced electron transfer (PET). Here, the fluorophore can either be a donor or an acceptor. The donor and acceptor form a complex in the excited state and this charge transfer complex returns to the ground state without the emission of a photon, but in some case exciplex emission is observed.[102, 103] Finally, the extra electron on the acceptor returns to the donor. Also quenching is possible, when the fluorophore binds on nanoparticles.[27, 72, 109] Ipe et al.[110] explain the possible quenching mechanism of pyrene on gold particle surfaces, as shown in Scheme 2.2. This scheme shows two possible mechanisms of energy and electron transfer, but most reports from the literature indicate that energy transfer from the excited state of fluorophore to the gold core dominates.[27, 72, 109, 110]
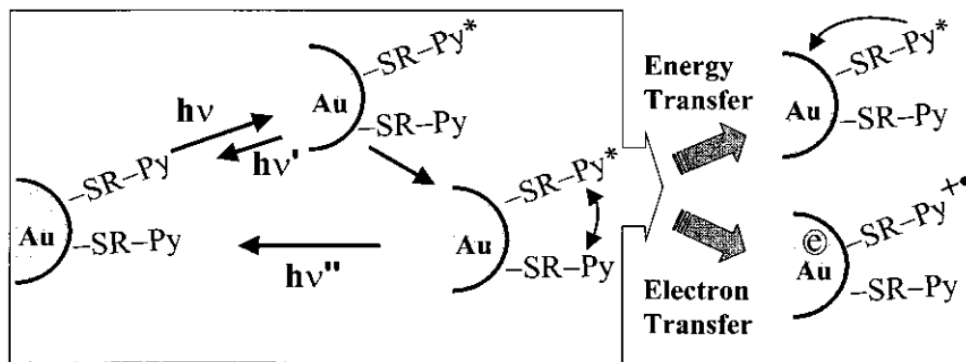
Scheme 2.2: The plausible quenching mechanism of pyrene molecules binding to a gold nanoparticles surface.[110]

2.6.3. High resolution transmission electron microscopy

Transmission electron microscopy (TEM) techniques are capable of structural characterization on the sub-nanometer scale. By using high-resolution transmission electron microscope (HRTEM) atomic arrangements are determined more accurately than by TEM. A resolution of 0.1 nm, which corresponds to a magnification factor of 10^6 can be reached by HRTEM.[111] Further, the resolution depends on the nature of the sample, where gold or silver have higher contrast than semiconductor quantum dots and the resolution depends on the sample preparation, where drying effects may occur. For sample, preparation grids with different films, such as carbon, Formvar can be used. The thin film on which the samples are dried is brought under the electron beam, which is accelerated to 200 keV in high-vacuum of about 10^{-6} mbar. Three types of lenses are used to form the final image: condenser, objective, and projector lenses. The condenser lenses are used to focus the electron beam onto the sample and restrict or remove high angle electrons that deviate from the main optic axis. The resulting thin beam travels through the sample and part of it are transmitted. The transmitted electrons are focused by the objective lens. The objective lens is the heart of the TEM, it forms the initial enlarged illuminated image of the sample in a plane which would be suitable for further magnification of the image on a screen which is usually a phosphorescent plate by using a projector lens. In the image projection mode, the objective aperture enhances the contrast by blocking high-angle diffracted electrons. Finally

the projector lens projects the final magnified image onto the fluorescent plate. The image can be photographically acquired using a charge-coupled device (CCD) through direct contact with the high-energy electron beam. The transmission microscopes also permit to obtain diffraction patterns which provide information on the crystalline structure of the sample. The objective lens collects all scattered electrons by the sample at a single point on the phosphorescent plate. In this back focal plane of the microscope, the diffraction patterns are formed. A crystalline sample will diffract the electron beam strongly through well-defined directions which are dependent on electron wavelength and crystal lattice spacing by Bragg's law:[112]

$$n\lambda_{hkl} = 2d_{hkl}\sin\theta \qquad\qquad 2.23$$

Where n is an integer, λ is the electron wavelength, d is the crystal lattice spacing between atomic planes, and θ is the angle of incidence and also of reflection. Depending on the nature of the sample, a diffraction pattern usually consists of a series of rings (for samples consisting of many randomly oriented microcrystals) or a discrete lattice of sharp spots (for specimens with a single, crystalline domain). Each sharp point in the diffraction pattern is an image of the electron source. From the diffraction patterns one can determine the type of crystal structure such as (f.c.c. (face centre cubic), (b.c.c (body centre cubic)) because different crystal lattice will cleave into their own characteristic geometry. From the diffraction pattern, by measuring the distance between adjacent planes one can know the lattice parameter.

3. Experimental section

3.1. Methods

^{1}H and ^{13}C nuclear magnetic resonance (NMR): NMR spectra were recorded using a BRUKER-DMX-NMR spectrometer operating at 400 and 100 MHz for ^{1}H and ^{13}C, respectively. The spectra were measured in chloroform-d purchased from Deutero GmbH. Chemical shifts were referenced relative to the residual proton or carbon signal of the deuterated solvent as δ = 7.26 for the ^{1}H and δ = 77.00 ppm for the ^{13}C spectra.

Electrospray ionization - time of flight (ESI-TOF): Samples were run on an Agilent 6210 ESI-TOF LC-MS system from Agilent Technologies, Santa Clara, CA, USA. The solvent flow rate was adjusted to 4 µL/min and the spray voltage was set to 4 kV. The drying gas flow rate was set to 15 psi ($\approx$1 bar). All other parameters were adjusted for a maximum abundance of the protonated parent cation $(M+H)^+$.

Transmission electron microscopy (TEM): The diameters of the particles were measured using TEM. Samples for TEM were prepared by immersing carbon-coated copper 400-mesh grids (Quantifoil) into a dispersion of the particles in dichloromethane. Low resolution TEM images were recorded using a Zeiss EM 10 CR microscope operating at 60-80 kV. High resolution TEM images were recorded using a Philips CM 200 FEG microscope and a Technai F20 (FEI) microscope operating at 200 kV. The images were analyzed using the software Simple PCI from C-Images and ImageJ.

UV-Vis spectroscopy: Absorption spectra of dichloromethane dispersions of the nanoparticles and dichloromethane solutions of pyrene molecules were measured in 1.00 cm SUPRASIL quartz cells (Hellma) using a Perkin Elmer Lambda 9 or a Lambda 19 spectrophotometers.

Fluorescence spectroscopy: The fluorescence of the samples was measured using a HORIBA Jobin Yvon Fluoromax-4 spectrofluorometer. Samples of nanoparticles dispersions and dilute dichloromethane solutions of pyrene molecules were analyzed in 1.00 cm SUPRASIL quartz

stirring cells (Hellma). The emission spectra of the samples were recorded by using an excitation wavelength of 328 nm.

Ligand exchange kinetics: A dispersion of the dye capped gold in dichloromethane nanoparticles was placed in a 1.00 cm SUPRASIL quartz stirring cells (Hellma). Subsequently, the mono-, di-, or trivalent alkanethiol ligands were added quickly at 20 °C. Systematic kinetics studies were performed using a HORIBA Jobin Yvon Fluoromax-4 spectrofluorometer.

3.2. Synthesis of ligands

The substances used for synthesis of the ligands and the nanoparticles are listed in Appendix A.1 of this thesis. They were used as received, i.e. without further purification. The solvents chloroform, dichloromethane, ethanol, methanol, ethyl acetate, and hexane were purchased from Merck and distilled before use. All other solvents were purchased from Sigma-Aldrich and were used as received. All ligands prepared in this thesis were purified by column chromatography using 40-63 μm mesh silica gel. Thin-layer chromatography (TLC) was performed using TLC silica gel $60f_{254}$ plates, as purchased from Merck.

3.2.1. Preparation of flexible thiol–functionalized multivalent ligands

I. 1,1-Bis(mercaptomethyl)nonane (4) (Divalent Thiol)

a) Dimethyl 2-octylmalonate[113] (1)

A solution of sodium (2.5 g, 46.2 mmol) in dry MeOH (25 mL) was added to a solution of diethyl malonate (8.09 mL, 53.06 mmol) and 1-bromo-octane (6.12 mL, 35.43 mmol) in dry THF (35 mL) at 0 °C. Subsequently, the resulting solution was refluxed for 4 h. The reaction mixture was neutralized by dropwise addition of 1 N HCl (100 ml), condensed in vacuum, and extracted with ethyl acetate (3 x 50 mL). The organic layer was successively washed with

aqueous $Na_2S_2O_3$ (100 mL) then brine (100 mL). Then, the organic layer was dried over anhydrous Na_2SO_4 and the solvent were evaporated *in vacuo*. The residue was distilled at 107 - 108 °C / 0.3 mbar to afford **1** (the structure is shown below as Figure 3.1) as a colorless liquid (3.4 g, yield: 40%).
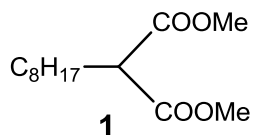
Figure 3.1: Chemical structure of dimethyl 2-octylmalonate (1).

NMR-^{1}H (400 MHz, CDCl$_3$) δ: 0.85 (t, 3 H, J = 6.7 Hz), 1.27-1.23 (m, 12 H), 1.87-1.81 (m, 2 H), 3.38-3.28 (m, 1 H), 3.70 (s, 6 H).

NMR-^{13}C (100 MHz, CDCl$_3$) δ: 14.0, 22.6, 27.3, 28.8, 29.1, 29.2, 31.8, 51.7, 51.9, 52.3, 61.2, 169.9 (2 C).

b) 1,1-Bis(hydroxymethyl)nonane[113] (2)

A solution of **1** (3.42 g, 14.02 mmol) in THF (11.7 mL) was added to a suspension of lithium aluminium hydride (LiAlH$_4$) (1.168 g, 30.78 mmol) in dry THF (7.8 mL) at 0 °C. The mixture was stirred for 1.5 h at RT. Subsequently, water (2 mL), of 15% (w/v) aq. NaOH (15 mL), and water (2 mL) were added successively to the reaction mixture. Subsequently, the reaction mixture was filtered through celite and dried over Na_2SO_4. The filtrate was condensed in vacuum and the crude product purified by column chromatography (20% EtOAc/hexane) to give **2** (the chemical structure is shown below as Figure 3.2) as a white solid (1.63 g, yield: 62%), mp 43 - 45 °C.
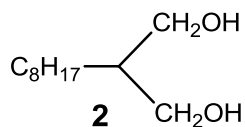

Figure 3.2: Chemical structure of 1,1-bis(hydroxymethyl)nonane (2).

NMR-^{1}H (400 MHz, CDCl$_3$) δ: 0.87 (t, 3 H, J = 6.7 Hz), 1.31-1.18 (m, 14 H), 1.80-1.71 (m, 1 H), 2.68 (s, 2 H), 3.65-3.63 (m, 2 H), 3.81-3.78 (m, 2 H).

NMR-^{13}C (100 MHz, CDCl$_3$) δ: 14.2, 22.7, 27.3, 27.8, 29.4, 29.6, 30.0, 31.9, 42.0, 66.7 (2 C).

c) 2-Octylpropane-1,3-dithioacetate[68] (3)

Diisopropyl azodicarboxylate (DIAD) (3.11 mL, 15.79 mmol) was added dropwise at 0 °C to triphenyl phosphine (PPh$_3$) (4.18 g, 15.93 mmol) in dry THF (46.6 mL). Subsequently, **2** (1.0 g, 5.319 mmol) and thioacetic acid (AcSH) (1.15 mL, 16.16 mmol) in 15.5 mL of dry THF were added to the reaction mixture and stirred at RT for 24 h. The reaction mixture was refluxed for 1 h, then EtOH (19.4 mL) was added and refluxing was continued for another hour. Volatile components were completely removed *in vacuo* and the residue was extracted by hexane (3 x 25 mL) and concentrated under reduced pressure to give a crude yellow oil. After column chromatography (2% EtOAc/hexane) pure **3** was isolated as a yellow oil (1.19 g, yield: 75%). The structure of **3** is shown in Figure 3.3.
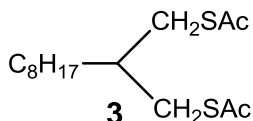

Figure 3.3: The chemical structure of 2-octylpropane-1,3-dithioacetate (3).

NMR-^{1}H (400 MHz, CDCl$_3$) δ: 0.84 (t, 3 H, J = 7.0 Hz), 1.29-1.23 (m, 14 H), 1.79-1.75 (m, 1 H), 2.30 (s, 6 H), 2.86-2.81 (dd, 2 H), 3.00-2.94 (dd, 2 H).

NMR-^{13}C (400 MHz, CDCl$_3$) δ: 14.2, 22.7, 26.7, 29.3, 29.5, 29.7, 30.7 (2 C), 31.9, 33.0, 32.6, 38.4 (2 C), 195.5 (2 C).

d) 1,1-Bis(mercaptomethyl)nonane[68] (Divalent Thiol (4))

 3 (0.60 g, 1.97 mmol) in dry THF (2 mL) was added dropwise to LiAlH$_4$ (0.22 g, 5.92 mmol) suspended in dry THF (6 mL) at 0 °C. The reaction mixture was stirred at RT for 15 h. Then, the reaction was quenched by addition of dilute HCl (1N) and extracted with CHCl$_3$ (3 x 15 mL). The organic layer was washed with brine (100 mL), dried over Na$_2$SO$_4$ and volatile compounds were removed *in vacuo* to afford **4** (structure is shown in Figure 3.4.) (0.38 g, yield: 88%) as a colorless oil.
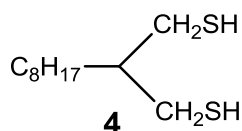
Figure 3.4: Chemical structure of 1,1-bis(mercaptomethyl)nonane (4).

NMR-^{1}H (400 MHz, CDCl$_3$) δ: 0.87 (t, 3 H, J = 7.2 Hz), 1.18 (t, 2 H, J = 8.4 Hz), 1.21-1.26 (m, 12 H), 1.32-1.41 (m, 2 H), 1.61-1.70 (m, 1 H), 2.58-2.72 (m, 4 H).
NMR-^{13}C (400 MHz, CDCl$_3$) δ: 14.2, 22.7, 26.8, 27.0, 29.3 (2 C), 29.6, 29.8, 31.5, 31.9, 42.7.
HRMS (ESI-TOF) m/z: (M-H)$^-$ calculated for C$_{11}$H$_{23}$S$_2$: 219.1241 and observed: 219.1260.

II. 1,1,1-Tris(mercaptomethyl)nonane (7) (Trivalent thiol)

a) 1,1,1-Tris(hydroxymethyl)nonane[114] (5)

KOH in 50% aq. ethanol (160 mL, 128.0 mmol) was added dropwise at 0 – 10 °C to decanal (24 mL, 128.0 mmol) and 40% HCHO (115 mL, 960.0 mmol) in 50% aq. ethanol (64 mL). The mixture was stirred overnight at RT and heated to 50 °C for 2 h. The solvent was removed under reduced pressure and the resulting heterogeneous mixture extracted with ether (3 x 100 mL) and volatile compounds were evaporated *in vacuo*. The remaining residue was recrystallized from

1:2 diethyl ether/hexane to afford **5** as a white solid (6 g, yield: 20%), mp 64 – 66 °C, the structure of **5** is shown in Figure 3.5.

CH₂OH

C₈H₁₇—⟨—CH₂OH

5 CH₂OH
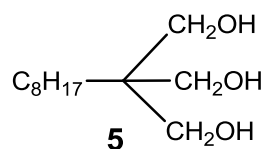
Figure 3.5: Chemical structure of the 1,1,1-tri(hydroxymethyl)nonane (5).

NMR-¹H (400 MHz, CDCl₃) δ: 0.88 (t, 3 H, J = 6.7 Hz), 1.21-1.32 (m, 14 H), 3.61 (s, 6 H), 3.68 (s, 3 H).

NMR-¹³C (100 MHz, CDCl₃) δ: 13.8, 22.4, 22.7, 29.1, 29.3, 30.1, 30.4, 31.7, 42.7,   65.2 (3 C).

b) 1,1,1-Tris(thioacetoxymethyl)nonane[68] (6)

DIAD (4.05 mL, 20.61 mmol) was added dropwise to PPh₃ (5.40 g, 20.61 mmol) in dry THF (68.7 mL) at 0 °C. Subsequently, **5** (1.0 g, 4.58 mmol) and AcSH (1.47 mL, 20.6 mmol) in dry THF (22.9 mL) were added to the reaction mixture. The mixture was stirred at RT overnight and then refluxed for 1 h to yield a clear yellow solution. Subsequently, EtOH (22.9 mL) was added and refluxing was continued for another hour. All volatile components were completely removed *in vacuo* and the residue was extracted with hexane (3 x 25 mL) to give a yellow oil. The crude product was purified by column chromatography (1% EtOAc/hexane) to afford pure **6** whose structure is shown in Figure 3.6. The resulted product was in pale yellow crystalline solid (1.49 g, yield: 83%), mp 138 – 141 °C.
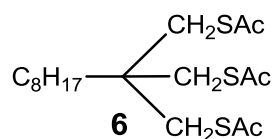
CH₂SAc

C₈H₁₇—⟨—CH₂SAc

6 CH₂SAc

Figure 3.6: Chemical structure of 1,1,1-tris(thioacetoxymethyl)nonane (6).

NMR-^{1}H (400 MHz, CDCl$_3$) δ: 0.83 (t, 3 H, J = 6.7 Hz), 1.18-1.30 (m, 14 H), 2.29 (s, 9 H), 2.93 (s, 6 H).

NMR-^{13}C (100 MHz, CDCl$_3$) δ: 14.2, 22.7, 23.4, 29.3, 29.4, 30.1, 30.7 (3 C), 32.0, 35.3, 36.2, 41.1 (3 C), 194.7 (3 C).

c) 1,1,1-Tris(mercaptomethyl)nonane[32] (Trivalent Thiol (7))

6 (1.0 g, 2.54 mmol) was dissolved in THF (15 mL) and LiAlH$_4$ (1.09 g, 28.8 mmol) was added slowly in small portions at RT. The reaction mixture was refluxed under argon for 4 h, quenched by cautious addition of ethanol (19 mL) and acidified by slow addition of 1 N HCl (112 mL). The product was subsequently extracted by Et$_2$O (3 x 15 mL). The combined organic layers were washed with dilute HCl (1N, 30 mL) and brine (30 mL), dried over anhydrous Na$_2$SO$_4$ and filtered. The crude product was purified by column chromatography, eluting with diethyl ether/hexane (5%) to afford **7** as a yellow oil (0.33 g, yield: 49%). The chemical structure of the 1,1,1-tris(mercaptomethyl)nonane is shown in Figure 3.7.
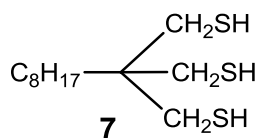
Figure 3.7: Chemical structure of 1,1,1-tris(mercaptomethyl)nonane (7).

NMR-^{1}H (400 MHz, CDCl$_3$) δ: 0.89 (t, J = 6.7 Hz, 3 H), 1.13-1.09 (m, 2 H), 1.18 (t, J = 8.6 Hz, 3 H), 1.31-1.23 (m, 10 H), 1.40-1.35 (m, 2 H), 2.59-2.57 (d, J = 8.8 Hz, 6 H).

NMR-^{13}C (100 MHz, CDCl$_3$) δ: 14.1, 22.6, 23.2, 29.1, 29.2, 29.4 (3 C), 30.1, 31.8, 32.4, 41.3. (NB (3 C)

HRMS (ESI-TOF) m/z: (M-H)$^-$ calculated for C$_{12}$H$_{25}$S$_3$: 265.1119 and observed: 265.1382.

III. 4-Pyrenebutyl-11-mercapto-undecanoate (Pyrene Thiol (8))[27]

11-mercapto-undecanoic acid (0.28 g, 1.30 mmol) was dissolved in dry CH_2Cl_2 (6.5 mL) together with N-N'-dicyclohexylcarbodiimide (DCC) (0.27 g, 1.30 mmol), (4-DMAP) 4-dimethylaminopyridine (0.016 g, 0.13 mmol) and pyrene butanol (0.35 g, 1.30 mmol). The mixture was stirred at 0 °C for 10 min, and then at RT for 3 h. Precipitated 1,3-dicyclohexylurea was filtered off and the filtrate was washed with 0.1 N HCl (50 mL) and saturated aq. $NaHCO_3$ (50 mL). Then, the organic layer was dried over anhydrous Na_2SO_4, filtered and evaporated *in vacuo*. The crude product was purified by column chromatography (20% CH_2Cl_2/hexane), to afford **8** whose structure is shown in Figure 3.8. The resulting pyrene thiol was received as a fluorescent yellow oil (0.43 g, yield: 70%).
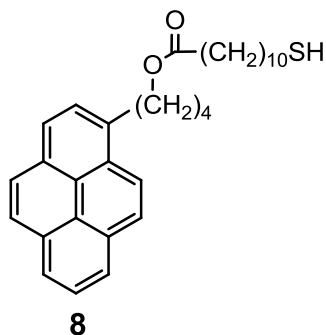
Figure 3.8: Chemical structure of 4-pyrenebutyl-11-mercapto-undecanoate (8).

NMR-^{1}H (400 MHz, CDCl$_3$) δ: 1.24-1.34 (m, 12 H),   1.53-1.68 (m, 5 H), 1.79-1.86 (m, 2 H), 1.90-1.98 (m, 2 H), 2.32 (t, 2 H, J = 7.4 Hz), 2.46-2.52 (m, 2 H), 3.36 (t, 2 H, J = 7.6 Hz), 4.19 (t, 2 H, J = 6.5 Hz), 7.84-7.86 (d, 1 H, J = 8.0 Hz), 7.98-8.02 (m, 3 H), 8.09-8.12 (m, 2 H), 8.16-8.19 (m, 2 H), 8.24-8.26 (d, 1 H), J = 9.3 Hz).

NMR-^{13}C (100 MHz, CDCl$_3$) δ: 24.5, 24.9, 28.0, 28.2, 28.5, 28.9, 29.0, 29.1, 29.2, 32.9, 33.9, 34.2, 63.9, 123.1, 124.6, 124.7, 124.8, 124.9, 125.0, 125.7, 126.5 (2 C), 127.0 (2 C), 127.1, 127.4, 129.7, 130.7, 131.3, 136.2, 173.8.

HRMS (ESI-TOF) m/z: ([M-H]+Na)$^+$ calculated for $C_{31}H_{38}O_2SNa$: 497.2491 and observed: 497.2508.

3.2.2. Preparation of flexible amine-functionalized multivalent ligands

I. 1,1-Bis(aminomethyl)nonane[77] (12) (Divalent Amine)

a. 1,1-Bis(methylsulfonyloxy)nonane (9)

Methanesulfonyl chloride (0.36 g, 3.1 mmol) in 3 mL of dry pyridine was added to a cooled (0 °C) solution of 2,2-bis(hydroxymethyl)nonane (2) (0.3 g, 1.59 mmol) and the reaction mixture was stirred at (0 - 10 °C) for 3 h. The reaction was quenched by the addition of crushed ice, and extracted with CH_2Cl_2 (3 x 50 mL). The organic layer was washed with 1 N HCl (3 x 100 mL) and a saturated solution of $NaHCO_3$ (100 mL). The organic layer was dried over anhydrous Na_2SO_4 and concentrated under reduced pressure. The crude product was then purified by column chromatography (15% EtOAc/hexane) to give **9** as a pale yellow crystalline solid (0.93 g, yield: 84%), mp 48 - 51 °C. The chemical structure of **9** is shown in Figure 3.10.
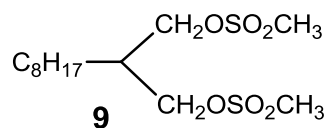
Figure 3.9: Chemical structure of 1,1-bis(methylsulfonyloxy)nonane (9).

NMR-^{1}H (400 MHz, CDCl$_3$) δ: 0.88 (t, 3 H, J = 6.7 Hz), 1.27-1.36 (m, 10 H), 1.36-1.45 (m, 4 H), 2.11-2.20 (m, 1 H), 3.04 (s, 6 H), 4.18-4.22 (m, 2 H), 4.28-4.31 (m, 2 H).
NMR-^{13}C (100 MHz, CDCl$_3$) δ: 14.2, 22.6, 26.5, 27.0, 29.1, 29.3, 29.4, 31.7, 37.2, 38.1 (2 C), 68.2 (2 C).

b) 1,1-Bis(azidomethyl)nonane (10)

9 (0.53 g, 1.5 mmol) was dissolved in dry DMF (10 mL), subsequently sodium azide (NaN$_3$) (0.60 g, 9.23 mmol) was added, and the resulting mixture was stirred overnight at 60 °C. The reaction was then quenched by adding water (10 mL) and extracted with hexane (3 x 25 mL),

dried over Na_2SO_4 and concentrated under reduced pressure to give pure **10** whose structure is shown below as Figure 3.11. The resulting product **10** was a colorless liquid (0.28 g, yield: 78%) which was used without further purification.
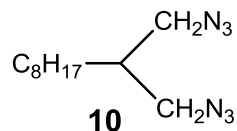
Figure 3.10: The chemical structure of 1,1-bis(azidomethyl)nonane (10).

NMR-^{1}H (400 MHz, CDCl$_3$) δ: 0.86 (t, 3 H, J = 6.7 Hz), 1.25-1.29 (m, 14 H), 1.70-1.77 (m, 1 H), 3.27-3.27 (m, 4 H).

NMR-^{13}C (100 MHz, CDCl$_3$) δ: 14.1, 22.7, 26.5, 26.7, 29.2, 29.4, 29.7, 31.8, 38.7, 52.7 (2 C).

c) 1,1-Bis(aminomethyl)nonane (11) (Divalent Amine)

A solution of **10** (0.27 g, 1.17 mmol) in dry THF (3 mL) was added dropwise to a suspension of LiAlH$_4$ (0.17 g, 4.6 mmol) in THF (10 mL), and the reaction was stirred for 15 h at 60 °C. 15% NaOH was slowly added to the chilled reaction mixture until a white granular precipitate had formed. The mixture was filtered through celite and the filtrate was dried over anhydrous Na_2SO_4 and volatile compounds were evaporated under reduced pressure to afford pure **11** (0.15 g, yield: 53%). The chemical structure of divalent amine is shown in Figure 3.12.

Figure 3.11: Chemical structure of 1,1-bis(aminomethyl)nonane (11).

NMR-^{1}H (400 MHz, CDCl$_3$) δ: 0.88 (t, 3 H, J = 6.7 Hz), 1.22 (s, 4 H), 1.29 (s, 14 H), 1.37-1.44 (m, 1 H), 2.66-2.75 (m, 4 H).

NMR-^{13}C (100 MHz, CDCl$_3$) δ: 14.0, 22.5, 26.9, 29.2, 29.5, 29.7, 29.9, 31.8, 43.6 (2 C), 43.7.

HRMS (ESI-TOF) m/z: (M-H$^-$) calculated for $C_{11}H_{25}N_2$: 185.2018 and observed: 185.2009.

II. 1,1,1-Tris(aminomethyl)nonane[77] (14) (Trivalent Amine)

a) 1,1,1-Tris(methylsufonyloxymethyl)nonane (12)

Methanesulfonyl chloride (0.94 g, 8.24 mmol) was added to a cooled (0 - 10 °C) solution of 5 (0.60 g, 2.74 mmol) in dry pyridine (4 mL) and stirring was continued for 5 h at (0 - 10 °C). The reaction mixture was quenched by pouring it into ice water and the product was extracted with CH_2Cl_2 (3 x 25 mL). The combined organic layers were washed successively with 1 N HCl (50 mL) and saturated aq. $NaHCO_3$ (50 mL). Subsequently, the mixture was dried over Na_2SO_4 and the solvent removed under reduced pressure. The crude product was purified by column chromatography (2% $CHCl_3$/MeOH) to afford pure **12** (structure is shown as Figure 3.13) (0.53 g, yield: 61%) as a pale yellow oil.
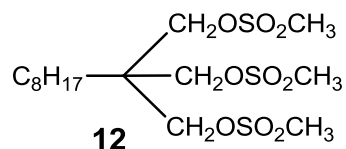
Figure 3.12: Chemical structure of 1,1,1-tris(methylsulfonyloxymethyl)nonane (12).

NMR-^{1}H (400 MHz, CDCl$_3$) δ: 0.88 (t, 3 H, J = 6.7 Hz), 1.27-1.30 (m, 12 H), 1.48-1.50 (m, 2 H), 3.10 (s, 9 H), 4.20 (s, 6 H).
NMR-^{13}C (100 MHz, CDCl$_3$) δ: 13.9, 22.1, 22.4, 29.0, 29.1, 29.7, 31.5, 37.1, 41.7, 67.7 (6 C).

b) 1,1,1-Tris(azidomethyl)nonane (13)

NaN_3 (0.75 g, 11.5 mmol) was added to a solution of **13** (0.58 g, 1.27 mmol) in dry DMSO (4 mL). Subsequently, tertaoctylammonium bromide (TOAB) (0.07 g, 0.12 mmol) was added to the reaction mixture and heating at 120 °C was continued for 5 h. The reaction was then quenched by adding water (4 mL) and the product was extracted with hexane (3 x 25 mL), dried over Na_2SO_4 and concentrated under reduced pressure to give pure **13** (0.31 g, yield: 84%) as a

colorless liquid. The structure of **13** is shown in Figure 3.14 and the compound was used in the next step without purification.
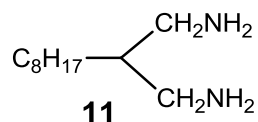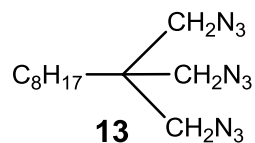

Figure 3.13: The chemical structure of 1,1,1-tris(azidomethyl)nonane (13).

NMR-^{1}H (400 MHz, CDCl$_3$) δ: 0.88 (t, 3 H, J = 6.7 Hz), 1.19-1.28 (m, 2 H), 1.28-1.33 (m, 12 H), 3.27 (s, 6 H).

NMR-^{13}C (100 MHz, CDCl$_3$) δ: 14.0, 22.5, 22.6, 29.1, 29.3, 30.0, 31.1, 31.8, 42.7, 53.5 (3 C).

c) 1,1,1-Tris(aminomethyl)nonane (14) (Trivalent Amine)

13 (0.31 g, 1.1 mmol) in THF (5 mL) was added dropwise to a solution of LiAlH$_4$ (0.14 g, 3.8 mmol) in dry THF (3 mL) at 0 °C. The reaction mixture was stirred at 60 °C overnight. The reaction was then quenched by cautious addition of 15% NaOH solution until a white granular precipitate appeared. The solution was filtered through celite, dried over Na$_2$SO$_4$, and the solvent was evaporated under reduced pressure to afford pure **14** (0.22 g, yield: 81%). The structure of the trivalent amine is shown below as Figure 3.15.

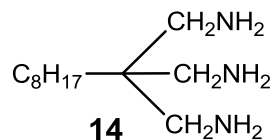**Figure 3.14:** Chemical structure of 1,1,1-tris(aminomethyl)nonane (14).

NMR-^{1}H (400 MHz, CDCl$_3$) δ: 0.88 (t, 3 H, J = 7.0 Hz), 1.20 (s, brs, 10 H), 1.32 (brs, 10 H), 2.58 (s, 6 H).

NMR-^{13}C (100 MHz, CDCl$_3$) δ: 14.0, 22.5, 22.8, 29.2, 29.5, 30.6, 31.2, 31.7, 41.6, 44.7 (3 C).

HRMS (ESI-TOF) m/z: (M+H)$^+$ calculated for C$_{12}$H$_{30}$N$_3$: 216.2439 and observed: 216.2445.

56

3.3. Synthesis of nanoparticles

All glassware used for the synthesis of nanoparticles was washed with aqua regia (3:1, conc. HCl: conc. HNO$_3$) and distilled water. **Caution!** *Aqua regia should be handled with extreme care*.

3.3.1. Synthesis of gold nanoparticles

I. Synthesis of pyrene thiol stabilized gold nanoparticles

a) Synthesis of pyrene thiol coated gold nanoparticles (Au-small)

The pyrene thiol capped gold nanoparticles were synthesized by a reported procedure[50] with a minor modification. 6.00 mg of pyrene thiol was added to chloro(triphenylphosphine)gold (I) (AuPPh$_3$Cl) (0.015 g, 0.03 mmol) in 1.5 mL of chloroform to form a clear solution. 0.027 g of tert-butylamine-borane complex (0.3 mmol) in CHCl$_3$ (1.5 mL) and ethanol (0.6 mL) were added and the mixture was stirred for 24 h. A color change from colorless to brown was observed, indicating the formation of gold nanoparticles. Then the nanoparticles were centrifuged at 100 g for 10 min and subsequently the supernatant was removed. This procedure was repeated until the fluorescence signal from the dye in the supernatant became negligibly small. Then the pyrene thiol bound Au-small nanoparticles were dried *in vacuo* and stored under an argon atmosphere.

b) Synthesis of pyrene thiol capped gold nanoparticles (Au-medium)[27]

Chloroauric acid (HAuCl$_4$) (0.017 g, 0.05 mmol) dissolved in water (3 mL) was added TOAB (0.11 g, 0.2 mmol) in CHCl$_3$ (2 mL). The mixture was stirred until the aqueous layer became colorless, whereas the organic phase became deeply red, indicating complete transfer of the gold ions to the organic layer. 10 mg of pyrene thiol (0.02 mmol) was added to the organic layer. Subsequently, a freshly prepared solution of sodium borohydride (NaBH$_4$) (0.02 g, 0.5 mmol) in

3 mL of water was added as a single aliquot. A color change from red to brown was observed, indicating the formation of gold nanoparticles. After that, particles were centrifuged at 1000 g for 10 min and subsequently the supernatant was removed. This washing procedure was repeated until the fluorescence signal from dye in the supernatant became negligibly small. The pyrene thiol coated Au-medium nanoparticles were dried *in vacuo* and stored under an argon atmosphere.

c) Synthesis of pyrene thiol coated gold nanoparticles (Au-large)

Large sized dye-capped gold nanoparticles were synthesized by a modification of a reported procedure.[115] A solution of $HAuCl_4$ (8.50 mg, 0.025 mmol) in water (1.4 mL) was added to a solution of TOAB (0.054 g, 0.1 mmol) in $CHCl_3$ (2.5 mL). The mixture was stirred for 22 h and then the aqueous layer was discarded. 4.7 mg of Pyrene thiol (0.1 mmol) was added, followed by a freshly prepared solution of $NaBH_4$ (0.01 g, 0.25 mmol) in water (1.5 mL) was added as one aliquot. The reaction mixture was stirred for another 2 h, after which a color change from red to brown confirmed the formation of gold nanoparticles. After that, the particles were centrifuged at 1000 g for 10 min and subsequently, the supernatant was removed. This procedure was repeated until the fluorescence signal from the dye in the supernatant became negligibly small. The pyrene thiol stabilized Au-large particles were dried and stored under an argon atmosphere.

3.3.2. Synthesis of silver nanoparticles

I. Synthesis of pyrene thiol stabilized silver particles

Silver nitrate ($AgNO_3$) (2.20 mg, 0.013 mmol) in water (0.4 mL) was added to TOAB (0.047 g, 0.0867 mmol) in $CHCl_3$ (1.5 mL). The reaction mixture was stirred for 45 minutes to ensure complete transfer of silver ions from the aqueous phase to the organic phase. Pyrene thiol (2.50 mg, 5.2 μmol) was added to the organic phase and after stirring for 15 minutes, $NaBH_4$ (7.0 mg, 0.18 mmol) in water (0.5 mL) was added dropwise to the reaction mixture. The reaction was allowed to continue overnight until the color had changed from colorless to brown, confirming

nanoparticles formation. After that, the particles were centrifuged at 1000 g for 10 min and subsequently the supernatant was removed. This procedure was repeated until the fluorescence signal from the dye in the supernatant became negligibly small. The pyrene thiol functionalized silver nanoparticles were subsequently dried *in vacuo* and stored under argon.

II. Synthesis of mono-, di, and trivalent amine ligand-stabilized silver nanoparticles at 120 °C

For the first time a new procedure was developed to prepare multivalent amine coated silver nanoparticles at 120 °C using silver(II) acetylacetonate (Ag(acac)$_2$). Mono-, di-, or trivalent amine (1 mmol) and 1,2-hexadecanediol (1.3 g, 5.0 mmol) were added to a solution of (Ag(acac)$_2$) (0.10 g, 0.5 mmol) in octyl ether (5 mL) under argon follow and the solution was heated to 120 °C. The color of the solution turned from yellow to brown at 80 °C, indicating spontaneous formation of nanoparticles. Next, the reaction mixture was stirred for 30 min at 120 °C and cooled to room temperature. The nanoparticles were precipitated by addition of ethanol (6 mL). The brown product was isolated by centrifugation and the supernatant are decanted. The particles were washed three times with ethanol to remove excess amine and the particles were dried *in vacuo* and stored under argon.

3.3.3. Synthesis of mono-, di-, and trivalent amine ligand-stabilized platinum nanoparticles at 200 ° C

A novel procedure was developed to prepare platinum nanoparticles coated by multivalent amines at 200 °C using platinum (II) acetylacetonate (Pt(acac)$_2$). Mono-, or di-, or trivalent amine (1 mmol) and 1,2-hexadecanediol (1.3 g, 5 mmol) were added to Pt(acac)$_2$ (0.20, 0.5 mmol) in octyl ether (5 mL) under argon atmosphere and the solution was heated to 200 °C. The color of the solution turned to blackish brown immediately in the case of the monovalent amine and within 5 minutes in the case of the di- and trivalent amine ligands, indicating the spontaneous formation of nanoparticles. Then, the reaction mixture was stirred for 5 minutes at 200 °C for the monovalent amine and for 30 minutes at the same temperature for the di- and

trivalent amines. After cooling to room temperature the nanoparticles were precipitated by addition of ethanol (6 mL). The black product was isolated by centrifugation and subsequently the supernatant was discarded. The particles were washed three times with ethanol to remove the excess of amines.

3.3.4. Synthesis of mono-, di-, and trivalent amine-coated silver and platinum nanoparticles at different temperatures.

A new procedure was developed to prepare multivalent amine-coated platinum or silver nanoparticles at high temperatures using $(Pt(acac)_2)$ or $(Ag(acac)_2)$, respectively. The synthesis of mono-, or multivalent amine capped silver or platinum nanoparticles at different temperatures was carried out under an argon atmosphere. The particles were synthesized at 80 - 120 °C in case of silver and at 160 - 200 °C in case of platinum particles, respectively. Mono- or multivalent amine ligand (2 equiv) and 1,2-hexadecanediol (10 equiv) were added to silver(II) or platinum(II) acetylacetonate (1 equiv) in octyl ether (5 mL) and the solution was heated to 80 °C and 160 °C for silver or platinum nanoparticles, respectively. The reaction mixture was heated for 30 minutes. Subsequently, the temperature was raised by 10 °C every 30 minutes until 120 °C and 200 °C was reached for silver or platinum nanoparticles, respectively. This temperature was maintained for 30 minutes. Samples were collected from the reaction mixture at each temperature step.

4. Results and discussions

4.1. Binding kinetics studies of flexible thiol-functionalized multivalent ligands on gold nanoparticles

This Section deals with the kinetics of the exchange reaction of mono- and multivalent flexible thiol-functionalized ligands on gold nanoparticles of three different sizes, are considered. Thiol ligands are well-known and well established as excellent stabilizers for gold nanoparticles.[48] In the past, the ligand exchange kinetics of thiols on metal nanoparticles have been studied using NMR[24, 25] and EPR[26] spectroscopy (see Section 2.5 for more details). With both techniques, it is quite difficult to study the kinetics and, hence, to derive the mechanism for the fast reactions. Both techniques need ≥ 15 s as an acquisition time to take one spectrum, which results in intervals of at least 1-5 min in time resolved measurements. This impedes to explore the kinetics of fast ligand exchange reactions, since an accurate knowledge of the kinetics of the initial stage of the ligand exchange reaction is required to derive the mechanism of such exchange reactions. To overcome these difficulties Montalti et al. used time-resolved fluorescence spectroscopy to monitor fast ligand exchange reactions.[27] These authors investigated the exchange of the fluorescencing dye 4-pyrenebutyl-11-mercaptoundecanoate on gold nanoparticles against dodecanethiol at different concentrations. They estimated the reactions rates and evaluated the reaction mechanism. The key concept of this method is to exploit the fact that the quenched fluorescence of particle-bound dyes completely recovers when they are exchanged against dodecanethiol ligands when they are released in solution. The recovery of this fluorescence signal is monitored as a function of time and, hence, gives detailed information on the kinetics of this ligand exchange reaction.

In the present work, this concept used to investigate the exchange kinetics of 4-pyrenebutyl-11-mercaptoundecanoate (pyrene thiol) bound on metal gold particles against thiol-functionalized flexible ligands. To the best of our knowledge, the binding kinetics of multivalent ligands on gold nanoparticles has not yet been reported apart from our own publication.[116]

4.1.1. Study of the binding kinetics of flexible thiol-functionalized multivalent ligands on gold nanoparticles

The binding kinetics of thiol ligands on nanoparticles are first investigated on gold nanoparticles. This Section will describe the binding kinetics of thiol-functionalized multivalent ligands on gold nanoparticles with three different sizes. For this, pyrene thiol (4-pyrenebutyl-11-mercaptoundecanoate) was synthesized using a reported procedure (see Scheme 4.3).[27] To exchange pyrene thiol ligands against flexible thiol ligands, the ligands are chosen in such a way that the lengths of the alkyl chains of the ligands are almost the same as that of pyrene thiol so that the results can be compared to each other. Commercially available dodecanethiol is chosen as a monovalent thiol model compound (see Figure 4.1), 1,1-bis(mercaptomethyl)nonane as a divalent thiol (see Scheme 4.1), and 1,1,1-tris(mercaptomethyl)nonane as a trivalent thiol (see Scheme 4.2). The divalent and trivalent ligands are synthesized using reported procedures.[32, 68, 113, 114]

a) Dodecanethiol (flexible monovalent thiol)

The monovalent (dodecanethiol) thiol is commercially available and is used as received (see Figure 4.1)
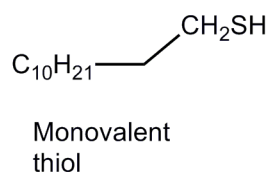
Figure 4.1: Chemical structure of dodecanethiol.

b) 1,1-Bis(mercaptomethyl)nonane[68, 113] (Divalent Thiol (4))

The reaction of sodium methoxide with n-octyl bromide and diethylmalonate gave dimethyl 2-octylmalonate **1**. Then, 1,1-bis(hydroxymethyl)nonane **2** was prepared by reducing **1** using lithium aluminium hydride (LiAlH$_4$). Subsequently, **2** was transformed into the thioacetate **3** using a Mitsunobu reaction, in which **2** was treated by thioacetic acid (AcSH) in the presence of

triphenyl phosphine (PPh₃) and diisopropyl azodicarboxylate (DIAD). The obtained 2-octylpropane-1,3-dithioacetate **3** was reduced using LiAlH₄ to give the target molecule 1,1-bis(mercaptomethyl)nonane **(divalent thiol)** with a yield of 88% (see Scheme 4.1).
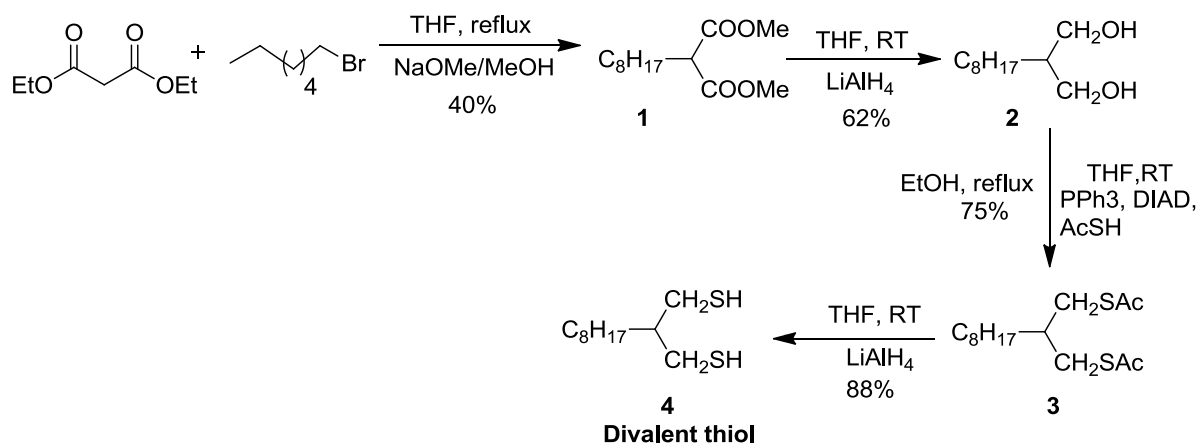
Scheme 4.1: Preparation of 1,1-bis(mercaptomethyl)nonane

c) 1,1,1-Tris(mercaptomethyl)nonane[32, 68, 114] (Trivalent Thiol (7))

Decanal was treated with formaldehyde in 50% aq. ethanol in the presence of potassium hydroxide to give 1,1,1-tris(hydroxymethyl)nonane **5**, which in turn was converted into the corresponding 1,1,1-tris(thioacetate) by reacting triol **5** with AcSH acid in the presence of PPh₃ and DIAD. The resulting 1,1,1-tris (thioacetoxymethyl)nonane **6** was reduced using LiAlH₄ to give 1,1,1-tris(mercaptomethyl)nonane (t**rivalent thiol)** with a 49% yield (see Scheme 4.2).
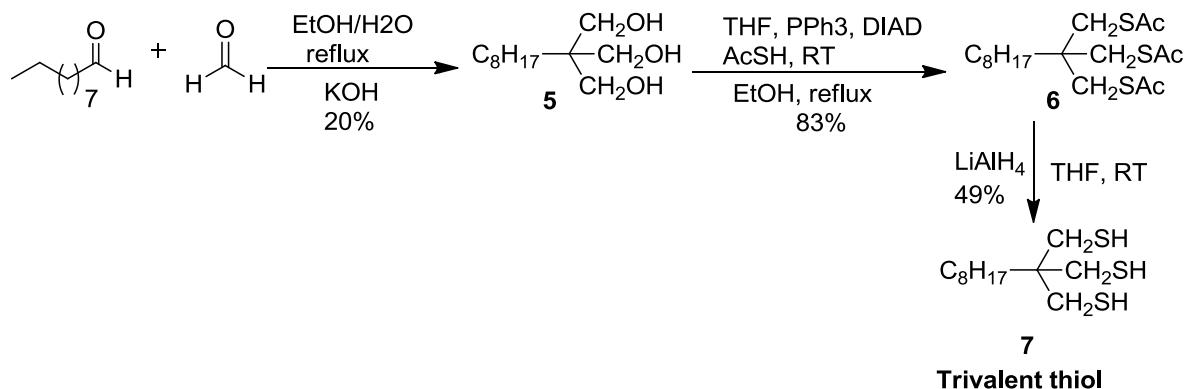
Scheme 4.2: Preparation of 1,1,1-tris (mercaptomethyl) nonane (trivalent thiol)

d) 4-Pyrenebutyl-11-mercaptoundecanoate[27] (Pyrene Thiol)

11-mercaptoundecanoic acid and 4-pyrene butanol are stirred together in presence of N,N'-dicyclohexylcarbodiimide (DCC) and 4-dimethylamino pyridine at room temperature for 3 h to yield **pyrene thiol** with 70% yield (see Scheme 4.3).
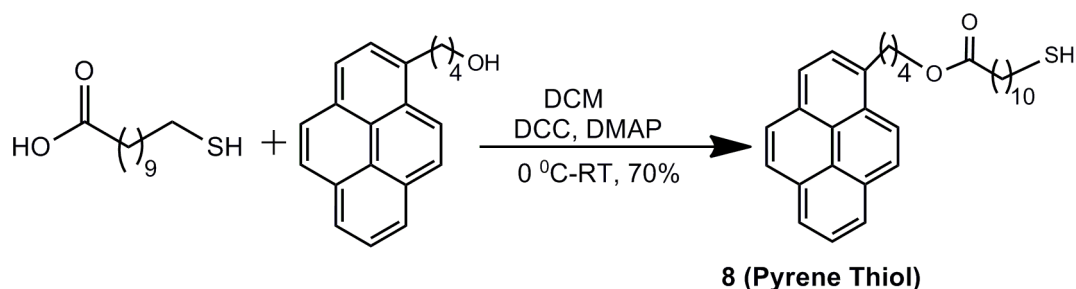
Scheme 4.3: Preparation of 4-pyrenebutyl-11-mercaptoundecanoate (pyrene thiol)

4.1.2. Synthesis of pyrene thiol-stabilized gold nanoparticles in the size range from 2.2 – 4.4 nm (samples 'Au-small', 'Au-medium', and 'Au-large')

Pyrene thiol-capped gold nanoparticles were synthesized using wet colloidal chemistry. To investigate the influence of ligand's multivalency and size of the particles by kinetics studies, gold nanoparticles samples with three different average diameters are prepared, sample Au-small with 2.2±0.4 nm, sample Au-medium with 3.2±0.7 nm, and sample Au-large with 4.4±0.9 nm diameter. Different types of gold salts are used to synthesize the particles of different size.[27, 50, 115] To prepare stable and almost monodisperse gold nanoparticles, the ratio of the dye molecules to the gold salts and the reaction time were optimized from the reported procedures (see Section 4.1.3).

Pyrene thiol **8**, chloro(triphenylphosphine) gold (I) (AuPPh$_3$Cl) and tert-butylamine-borane were stirred together in chloroform and ethanol which resulted in the formation of Au-small nanoparticles with 2.2±0.4 nm diameter, in the following marked as 'Au-small'.[50] Medium and larger particles were prepared by stirring chloroauric acid (HAuCl$_4$) in water and tertaoctylammonium bromide (TOAB) in CHCl$_3$ until the water phase was discolored and the

organic phase turned into a deep red. Pyrene thiol **8** was added to the organic phase followed by sodium borohydride in water, which reduced the $AuCl_4^-$ ions to obtain dye capped Au-medium and Au-large nanoparticles.[27, 115] In the first case, $HAuCl_4$ and TOAB were stirred only for 10 min and immediately after that the gold salt in the organic phase was reduced using sodium borohydride, which led to the formation of medium size gold nanoparticles. However, in the second case $HAuCl_4$ and TOAB were stirred for 24 h.[115] After this, by reducing the gold in the organic phase using sodium borohydride, yielded larger size pyrene thiol coated gold nanoparticles.

In each case, the pyrene thiol-stabilized gold nanoparticles were precipitated by the addition of ethanol and centrifuged at 1000 g for 10 minutes. The supernatant was collected to calculate the amount of pyrene thiol bound to the particles (see paragraph below in this Section). This procedure was repeated until the intensity of the fluorescence signal from the dye in the supernatant became negligibly low; ensuring that any free pyrene thiol that had not been bound to the particles was removed.

TEM images of small, medium, and large-sized pyrene thiol-stabilized gold nanoparticles are shown in Figure 4.2. These images show that all three varieties of nanoparticles obtained from the different syntheses have a nearly spherical shape and the aggregation of the nanoparticles is not taking place. An analysis of the TEM images gave the following diameters for the nanoparticles: 2.2±0.4 nm (Au-small), 3.2±0.7 nm (Au-medium), and 4.4±0.9 nm (Au-large). The three samples have a polydispersity of about 20%. Different batches of gold nanoparticles prepared by the same modified procedure yield reproducible particle sizes within ±0.2 nm.
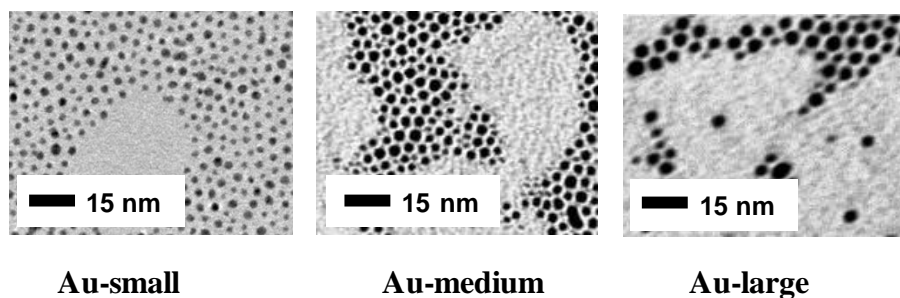

Au-small   **Au-medium**   **Au-large**

Figure 4.2: Transmission electron microscopy images of pyrene thiol coated Au-small, Au-medium, and Au-large nanoparticles.

It is known that the fluorescence of pyrene ligands bound to gold nanoparticles is entirely quenched.[27, 72, 117] This is due to an electron transfer from the excited state of the dye to the nanoparticles. Quenching of the fluorescence on gold surfaces depends on the distance between the chromophore and the gold surface.[118] Pyrene derivatives with a long alkyl chain (C_8-C_{14}), of the kind used in this work, are expected to be oriented to the gold surface at an angle of 45˚ - 48˚ according to recent calculations by Battistini et al..[117] Hence, the probability of charge transfer to gold is high and the fluorescence of the dye is completely quenched. It is assumed that the fluorescence of the dye molecules completely recovers when they are released from the gold surface.[27] Therefore, an increase in fluorescence intensity of the released dye is a quantitative probe for ligand exchange, facilitating studies of the kinetics of the exchange process. The number of pyrene ligands bound to the gold nanoparticles can be quantified from the amount of free dye in solution after purification of the nanoparticles, assuming that all dye molecules used in the synthesis are either found in the supernatants removed during purification or bound to the gold particles. The total mass of the free pyrene thiol is calculated by comparing the UV-Vis absorption intensity at 344 nm to a calibration curve shown in Figure 4.3 for solutions of pure pyrene thiol in dichloromethane with a known concentration. In this way, the initial number of pyrene ligands bound to gold nanoparticles at the beginning of the kinetic experiments can be accurately derived.
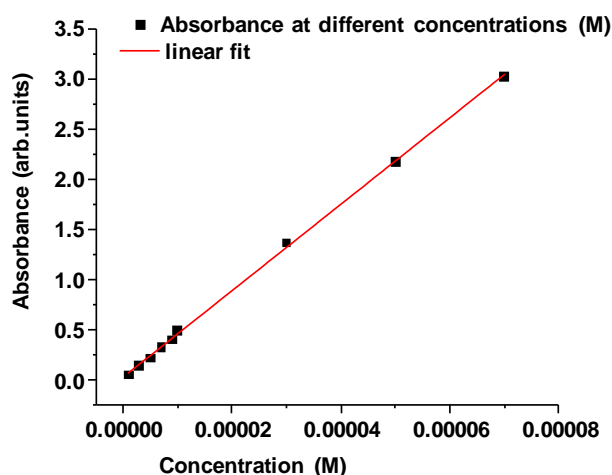
Figure 4.3: UV-Vis calibration curve for the pyrene thiol concentration in dichloromethane. The absorbance is measured at 344 nm.

Figure 4.4(a) shows the fluorescence intensity of different concentrations of the pyrene thiol in dichloromethane at 376 nm after excitation at 328 nm. This plot demonstrates that quenching of the dye starts at a concentration of $3 \cdot 10^{-5}$ M. To exclude quenching of the dye, the kinetic experiments are carried out at concentrations below $(2.79 \pm 0.31) \cdot 10^{-6}$ M. Fluorescence quenching due to oxygen is also ruled out by preparing the particles and carrying out all exchange reactions in an argon atmosphere. A calibration line for the initial linear part of the data shown in Figure 4.4(a) is shown in Figure 4.4(b). This calibration is used to quantify the amount of pyrene thiol released after the ligand exchange reaction (see Section 4.1.3).

Figure 4.4: (a) Fluorescence intensity at 376 nm of pyrene thiol in dichloromethane as a function of the concentration; (b) Calibration line for the initial linear part of the data shown in Figure (a). The excitation wavelength was 376 nm.

4.1.3. Kinetics studies of the binding of flexible mono- and multivalent thiols on gold nanoparticles of three different sizes (samples Au-small, Au-medium, and Au-large nanoparticles)

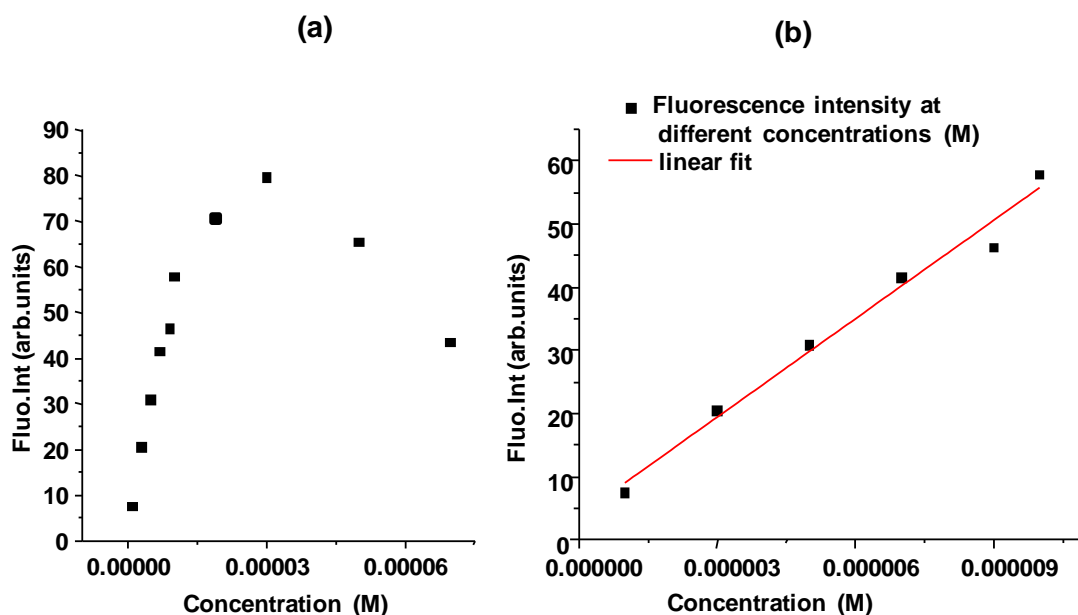The effect of the ligand multivalency on their exchange kinetics on gold nanoparticles with different sizes and the influence of the size of the particles on the ligand exchange reaction are discussed in this Section. The reaction rates that are influenced by ligand's multivalency and the sizes of the nanoparticles are evaluated using time-resolved fluorescence measurements. The kinetic data are fitted using various fit models, such as mono-exponential, bi-exponential, Langmuir first order, and second order models, as well as first order and second order diffusion-limited Langmuir models. The motivation to use these fit models are discussed in the following and the best fit models are chosen. Further, the validity of the bi-exponential and the Langmuir second order diffusion models are explained by a co-operative and diffusion models, respectively.

4.1.3.1. Ligand exchange measurements

In a typical ligand exchange experiment, a dilute dispersion of the pyrene thiol capped Au-small, Au-medium, or Au-large nanoparticles in dichloromethane was placed in a quartz stirring cell. Subsequently, the mono-, di- or trivalent thiol at the concentrations indicated in Table 4.1, were quickly added to the dispersion at 20 °C. The concentration of mono-, di-, or trivalent thiol ligands are chosen to be about three orders of magnitude higher than the pyrene thiol concentration in order to achieve a complete ligand exchange (see Table 4.1).

Table 4.1: Concentrations of each ligand used in the ligand exchange kinetics measurements

Ligand	Monovalent thiol	Divalent thiol	Trivalent thiol
Concentration (mM)	3.78±0.02	1.89±0.02	1.26±0.02

Figure 4.5 provides a schematic representation of the ligand exchange reaction in which the pyrene thiol is exchanged by the mono-, di-, or trivalent thiol ligand. The increase in fluorescence intensity (see Figure 4.5) of the out coming pyrene thiol as a function of time reflects the exchange of pyrene thiol bound to gold nanoparticles with the mono- or multivalent ligand. Since no spectral shifts in the fluorescence spectrum of the pyrene thiol were observed during the ligand exchange reactions, the ligand exchange kinetics were studied by measuring the fluorescence intensity of the pyrene thiol at 376 nm as a function of time (see Figures 4.5). The fluorescence intensity at the emission maximum at 376 nm was recorded at identical time intervals with an initial temporal resolution of about 0.25 s for the first 500 s. This was followed by temporal steps of 120 s for typically 16-30 h. No quenching effects were observed for pure pyrene thiol below a concentration of $(3.00\pm0.04)\cdot10^{-5}$ M (see Figure 4.4) under an air or argon atmosphere. Repeated experiments with practically identical results indicate that the temporal evolution of the fluorescence signal is reproducible. All kinetics data and rate constants shown in this thesis were obtained from at least three independent data sets.
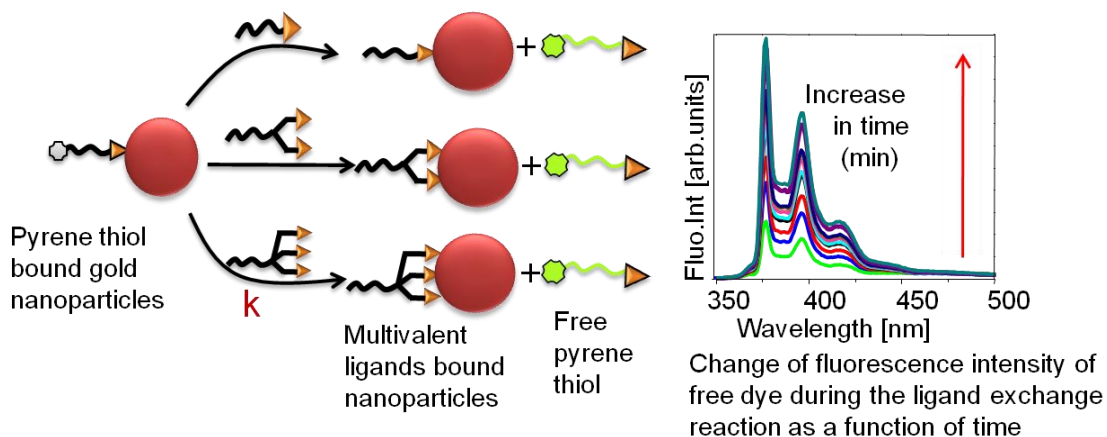

Figure 4.5: Ligand exchange kinetics studied by fluorescence spectroscopy. Pyrene thiol ligands (4-pyrenebutyl-11-mercaptoundecanoate) bound on gold particles are exchanged by mono-, di-, or trivalent thiol ligands.

4.1.3.2. Multivalency effects

The concentration of the competing thiol groups (mono-, di- or trivalent thiol) was kept constant in order to study multivalency effects on ligand exchange. During the ligand exchange, the pyrene thiol molecules bound to the particle were replaced by monovalent thiol (3.78 mM), divalent thiol (1.89 mM), or trivalent thiol (1.26 mM) ligands. Figure 4.6(a) shows the fluorescence intensity at 376 nm for the first 500 s of the ligand exchange reaction with these three ligands on Au-medium (3.2±0.7 nm) gold nanoparticles as a function of time. After a steep rise in fluorescence intensity at the beginning of the reaction, all curves flatten out considerably, as shown in Fig 4.6(b). Notably, the steep increase in fluorescence intensity signifies a ligand exchange, which is too fast to be monitored by NMR but can easily be probed by fluorescence spectroscopy. Figure 4.6(b) shows that the free pyrene thiol concentration reaches saturation during ligand exchange, corresponding to a concentration of pyrene thiol bound to gold nanoparticles of $(2.79±0.31)\cdot10^{-6}$ M (see above).

The fluorescence intensity was identical after 16 h within the limit of experimental errors in all three cases. The equilibrium of the reaction lies completely on the side of the product, due to the large excess (about 385 fold) of the competing ligand. Hence, a significant reverse reaction was not observed. After significantly longer reaction times of up to 30 h no changes in fluorescence intensity were observed. The reproducibility of these experiments was further confirmed by kinetics studies using different, freshly prepared batches of nanoparticles as well as nanoparticles stored as a dry precipitate at 25 °C under argon for at least one month.
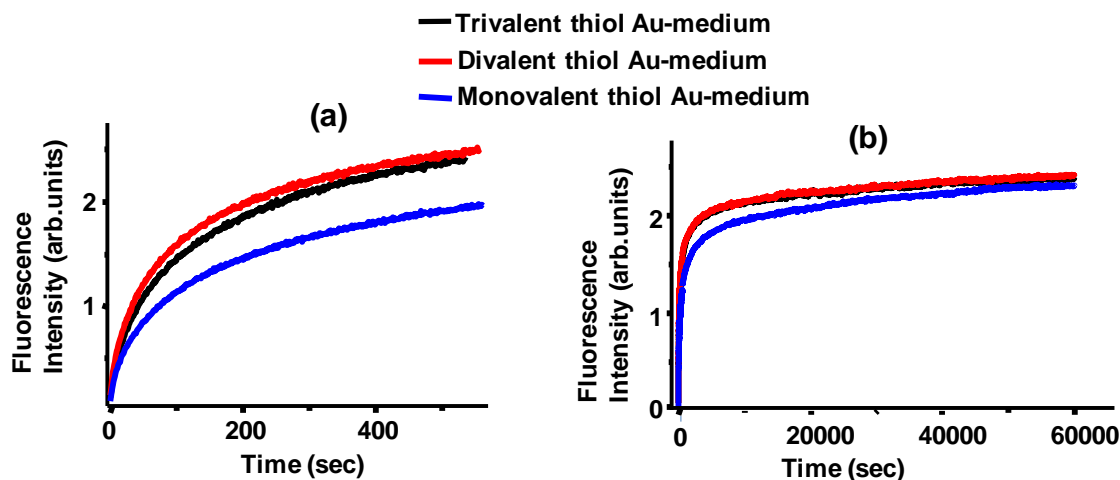
Figure 4.6: (a) Changes in fluorescence intensity at 376 nm as a function of time for the initial part of the ligand exchange reaction of mono-, di-, and trivalent thiol ligands against pyrene thiol on Au-medium (3.2±0.7 nm) gold nanoparticles. Figure (b) shows the kinetics of the same reaction in a wider time interval.

Previous kinetics studies have concluded that ligand exchange reactions occur either via dissociative[99, 119, 120] or associative[8, 27, 121] mechanisms. In some cases a combination of associative and dissociative mechanisms is involved.[122] A general overview of the mechanism of ligand exchange reactions on Au nanoparticles, especially with thiols, has been provided by Caragheorgheopol et al..[20] Furthermore, Montalti et al.[27] have shown that exchange reactions of pyrene thiol-coated gold nanoparticles at different concentrations of monovalent alkanethiol most likely follow an associative pathway. Therefore, it is reasonable to assume that the present exchange reaction also occurs via an associative mechanism. Previous kinetics studies indicate that a variety of different mechanisms can be used to fit the experimental results of ligand exchange reactions on gold nanoparticles[22, 27, 72, 83, 85] and gold clusters.[24, 25] These include pseudo-first order (mono-exponential) and second-order mechanisms,[22, 24, 25, 83, 94, 99] various types of Langmuir models (first order, second order, diffusion-limited first order, and diffusion-limited second order),[85] as well as bi-exponential fit functions.[27, 72, 94] Herein, bi-exponential and mono-exponential functions, first and second order Langmuir diffusion models, as well as first and second order Langmuir models are used to explain the experimental results. The

72

kinetics data from pyrene thiol exchanged on Au-small with monovalent thiol are chosen to show the agreement between the measured data and calculated curves obtained from different fit models. The agreement between the fit curves and the experimental data as well as the derived correlation coefficients R^2 values are discussed in greater detail in the following.

The analysis of the experimental data for exchange kinetics started with the simplest fit function, a mono-exponential fit model (see Equation 4.1)

$$I(t) = I_{f,1}(1 - e^{-k_1 t})$$

4.1

where $I_{f,1}$ is the fluorescence intensity after the complete exchange of pyrene thiol with the incoming thiols, k_1 is the reaction rate constant, and t is the time (see also Equation 4.4). The representative fit of averaged data from three independent data sets of the exchange of pyrene thiol molecules against monovalent thiol ligands on Au-small is shown as Figure 4.7. The mono-exponential fit function significantly deviates from the experimental data (see Figure 4.7) correspondingly, the R^2-value is only 0.851. For di- and trivalent ligands on Au-small and for all three types of ligands on Au-medium particles even less agreement between fit and experiments are found (see Table 4.2). The obtained R^2 values are in the range of 0.49-0.85. In general, slightly higher R^2 values are found for the ligand exchange on Au-small particle. Further, this fit model does not explain the differences of the reactivity on various binding sites of the nanoparticles (see below in this Section) and is not further considered for describing the experimental data.
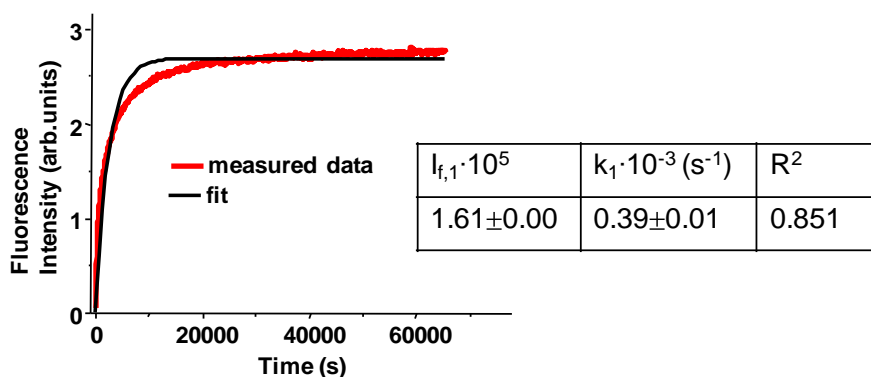
Figure 4.7: Changes in fluorescence intensity at 376 nm as a function of time for the ligand exchange reaction of monovalent thiol ligands against pyrene thiol bound on Au-small particles. The resulting experimental curve was fitted by a mono-exponential function shown in Equation 4.1.

Table 4.2: Rate constants for the exchange reaction of pyrene thiol on Au-small and Au-medium nanoparticles with mono- and multivalent thiol ligands obtained from a fit of the data in Figures 4.6 and 4.13 using a mono-exponential function (see Equation 4.1)

Particle	Fit parameters	Ligand		
		Trivalent thiol (1.26 mM)	Divalent thiol (1.89 mM)	Monovalent thiol (3.78 mM)
Au-medium (3.2±0.7 nm)	$k_1 \cdot 10^{-3}$ (s^{-1})	1.23±0.03	1.36±0.03	65.86±0.01
	$I_{f,1} \cdot 10^5$	1.76±0.01	1.76±0.01	1.82±0.01
	R^2	0.54±0.01	0.49±0.01	0.63±0.01
Au-small (2.2±0.4 nm)	$k_1 \cdot 10^{-3}$ (s^{-1})	28.60±0.04	1.09±0.02	39.8±0.04
	$I_{f,1} \cdot 10^5$	1.63±0.01	1.64±0.01	1.66±0.01
	R^2	0.79±0.01	0.72±0.01	0.85±0.01

Next, bi-exponential functions are applied to fit the experimental data. The use of a bi-exponential fit function is further motivated by the assumption that inhomogeneities in the particle surface lead to a rapid ligand exchange at defect sites, whereas the remaining non-defect

sites are subsequently exchanged.[24, 25, 27, 72, 83] According to Murray and co-workers, the necessity for a description of the exchange kinetics by a bi-exponential function is due to the fact that different sites of the gold nanoparticles that are edges, vertices, and faces exhibit different reactivities.[24, 83] This is explained in greater detail in the Section 2.4 and 2.5. The experimental data are fitted by a bi-exponential fit function shown in Equation 4.2.

$$I(t) = I_{f,1}\left(1 - e^{-k_1 t}\right) + I_{f,2}\left(1 - e^{-k_2 t}\right)$$

4.2

where, $I_{f,1}$ and $I_{f,2}$ are the amplitudes of the fluorescence intensity and k_1 and k_2 are the reaction rate constants. A representative bi-exponential fit of averaged data from three independent data sets of the exchange kinetics of monovalent thiols on Au-small particles is shown in Figure 4.8. The rate constant k_1 which represents the faster process of the reaction at the beginning of the ligand exchange is about $(2.00\pm0.04)\cdot10^{-3}$ s^{-1} (see the inset Table in Figure 4.8), whereas the rate constant k_2 which describes a slower process occurring at longer reaction times is about $(13.85\pm0.12)\cdot10^{-5}$ s^{-1}. Here, the fit function describes well the experimental data and the R^2 value is 0.99.

$I_{f,1}\cdot10^5$	$I_{f,2}\cdot10^5$	$k_1\cdot10^{-3}$ (s^{-1})	$k_2\cdot10^{-5}$ (s^{-1})	R^2
0.89±0.01	0.76±0.01	2.00±0.04	13.85±0.12	0.987
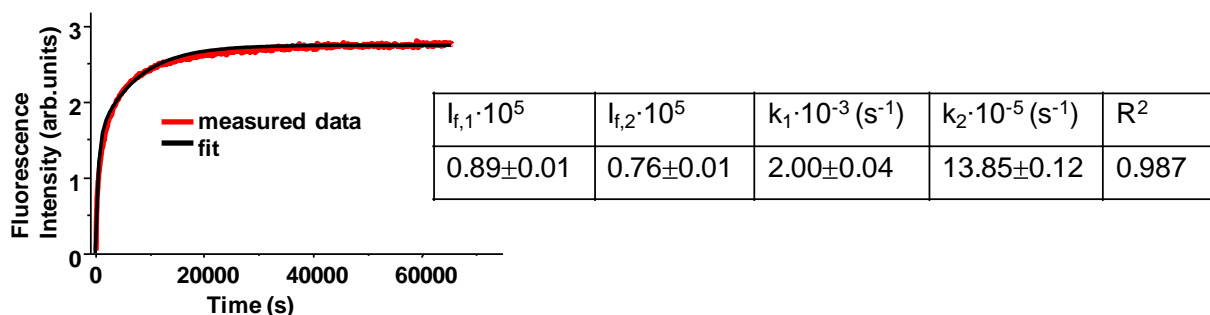
Figure 4.8: Changes in fluorescence intensity at 376 nm as a function of time for the exchange kinetics of monovalent thiol ligands against pyrene thiol bound on Au-small particles. The resulting experimental curve is fitted by a bi-exponential function (see Equation 4.2).

The rate constants obtained from fitting the experimental data of the exchange kinetics of mono-, di-, and trivalent thiols on Au-small and Au-medium particles using Equation 4.2 are summarized in Table 4.3. R^2 values in the range of 0.96-0.99 confirm full agreement between the bi-exponential fit function and the experimental data for all systems under study. The k_1 values significantly dependent on the ligand multivalency and the particle sizes, whereas such

correlation is not observed for the k_2 values. Thus, only the k_1 values are taken in account for the subsequent discussion. A comparison of the k_1 values shown in Table 4.3 reveals that exchange of pyrene thiol against, the trivalent thiol on Au-medium particles is 1.49 times faster than the exchange against the monovalent thiol. The exchange of pyrene thiol against the divalent thiol on medium size particles is 1.43 times faster than the exchange process of the monovalent one. On small size gold nanoparticles, the exchange rate of the trivalent thiols are much slower than that of the monovalent ones. In contrast, the divalent thiol exchanges 1.2 times faster than the monovalent ones do on small size particles. However, the ratio of the amplitudes $I_{f,1}$ and $I_{f,2}$ varies significantly for the different types of ligands, especially in case of the monovalent thiol ligands, this ratio is significantly smaller than the di- and trivalent ones (see Table 4.3).

Table 4.3: Rate constants of the exchange reaction of mono- and multivalent thiol ligands against pyrene thiol on Au-small and Au-medium nanoparticles obtained from a fit of the data in Figures 4.6 and 4.13 using a bi-exponential function (see Equation 4.2). The parameters k_1, k_2, $I_{f,1}$, and $I_{f,2}$ are free fit parameters.

Particle	Fit values	Ligand		
		Trivalent thiol (1.26 mM)	Divalent thiol (1.89 mM)	Monovalent thiol (3.78 mM)
Au-medium (3.2±0.7 nm)	$k_1 \cdot 10^{-3}$ (s^{-1})	3.84±0.34	3.68±0.50	2.57±0.55
	$k_2 \cdot 10^{-5}$ (s^{-1})	6.60±1.13	4.08±2.06	4.62±0.66
	$I_0 \cdot 10^5$	1.92±0.05	2.03±0.02	1.90±0.09
	$I_{f,1}/I_{f,2}$	3.67±0.30	3.43±0.21	2.33±0.13
	R^2	0.96±0.01	0.96±0.01	0.97±0.01
Au-small (2.2±0.4 nm)	$k_1 \cdot 10^{-3}$ (s^{-1})	1.16±0.09	2.68±0.14	2.09±0.17
	$k_2 \cdot 10^{-5}$ (s^{-1})	7.34±1.40	8.63±1.11	15.00±2.04
	$I_0 \cdot 10^5$	1.68±0.05	1.68±0.05	1.66±0.06
	$I_{f,1}/I_{f,2}$	1.61±0.01	4.23±0.78	1.11±0.12
	R^2	0.99±0.01	0.96±0.01	0.98±0.01

Thus, an attempt was made to scale the two amplitudes to the number of gold atoms on the edges and vertexes (corresponding with the first amplitude of the faster process, I_{f1}), and the number of gold atoms on face sites (corresponding to the second amplitude of the slower process I_{f2}). For this model calculation it was assumed that the gold nanoparticles were regular icosahedra and the number of atoms on the edges and vertexes are calculated as communicated by Benfield et al..[123] However, this calculation predicted a 3-7 times lower value for I_{f1}/I_{f2} than the ratios obtained from a free fit with Equation 4.2. In addition, no agreement was found between the ratio of the different sites of the gold nanoparticles and the amplitude ratio for the smaller and larger particles as shown in the Table 4.3. Hence, the different reaction rates cannot merely be ascribed to different geometric positions of the ligands in perfectly shaped icosahedra, since a systematic dependency of this amplitude ratio on the multivalency of the ligands or the size of the nanoparticles is not found.

For this reason, the ratio $I_{f,1} / I_{f,2}$ was set to the constant value of 2.5, which corresponds to the average ratio of these parameters obtained from the exchange kinetics (see Table 4.3). The rate constants were derived by fixing the amplitudes ratio to 2.5 are given in Table 4.4 and a representative fit of the exchange of pyrene thiol against the monovalent thiol on Au-small size particles by using Equation 4.2 with $I_{f,1} / I_{f,2} = 2.5$ is shown in Figure 4.9. The representative fit shows good agreement with the experimental results and a R^2 value of 0.97 is obtained from this analysis. According to Equation 4.2, $I_0 = I_{f,1} + I_{f,2}$ is the value of the fluorescence intensity after the complete exchange of pyrene thiol against the incoming ligands ($t = \infty$). For example, the plot shown in Figure 4.9 the fitted value of $I_0 = (1.65\pm0.02)\cdot10^5$ corresponds to a concentration of pyrene thiol of $(2.47\pm0.63)\cdot10^{-6}$ M according to the calibration curve shown in Figure 4.4(b). This value agrees within the experimental error with the estimated concentration of the pyrene thiol on the nanoparticles of $(2.79\pm0.31)\cdot10^{-6}$ M (see above).
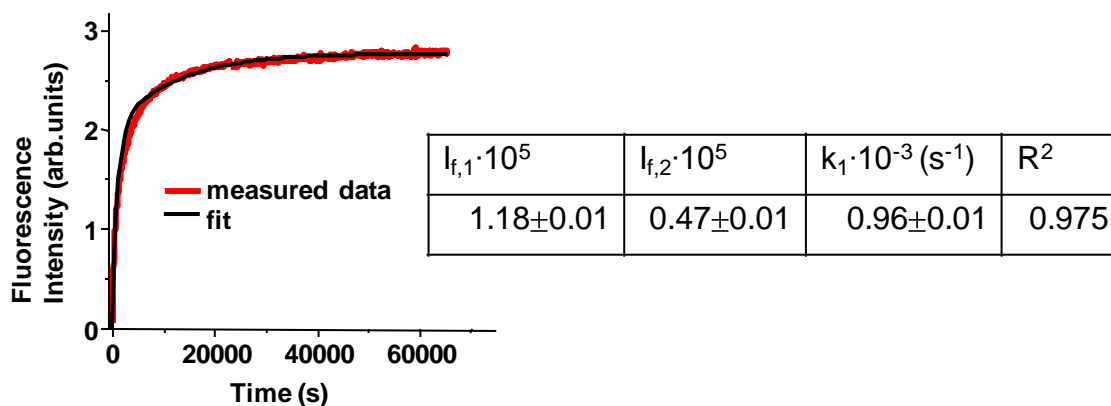
Figure 4.9: Changes in fluorescence intensity at 376 nm as a function of time for the exchange of pyrene thiol bound on Au-small nanoparticles against the monovalent thiol. The resulting curve was fitted by a bi-exponential function with fixed amplitudes ($I_{f,1}/I_{f,2}$=2.5) (see Equation 4.2).

The R^2 values in Table 4.4 are in the range of 0.92-0.97 and confirm that the bi-exponential fit function, where the ratio $I_{f,1}/I_{f,2}$ is set to a fixed value of 2.5 and describes well the experimental data. A comparison of the reaction rates from Table 4.4 shows that the trivalent thiol exchanges 2.25 times faster against the pyrene thiol on Au-medium size than the monovalent thiol does. The divalent thiols exchange 2.16 times faster than the monovalent thiols on the Au-medium particles. The exchange rate of the trivalent thiol is much smaller than that of the monovalent thiol on the Au-small size nanoparticles. In contrast, the divalent thiols exchanges 4.1 times faster than the monovalent thiol on the Au-small size nanoparticles. Since the fits of the experimental data using fixed amplitudes of the bi-exponential fit function give R^2 values close to one and yield more defined k_1 values, the data obtained from this fitting procedure are discussed in detail (see Section 4.1.3.4).

Table 4.4: Rate constants of the exchange reaction of mono-, and multivalent thiol ligands against pyrene thiol on Au-small and Au-medium nanoparticles obtained from a fit of the data in Figures 4.6 and 4.13 by a bi-exponential function (using Equation (4.1)), where the ratio $I_{f,1}/I_{f,2}$ is set to a fixed value of 2.5:

Particle	Fit parameters	Ligand		
		Trivalent thiol (1.26 mM)	Divalent thiol (1.89 mM)	Monovalent thiol (3.78 mM)
Au-medium (3.2±0.7 nm)	$k_1 \cdot 10^{-3}$ (s^{-1})	5.75±0.85	5.52±0.35	2.55±0.56
	$I_0 \cdot 10^5$	1.92±0.05	2.03±0.02	1.90±0.09
	R^2	0.93±0.01	0.92±0.02	0.97±0.01
Au-small (2.2±0.4 nm)	$k_1 \cdot 10^{-3}$ (s^{-1})	0.85±0.07	3.93±0.63	0.94±0.03
	$I_0 \cdot 10^5$	1.68±0.05	1.68±0.05	1.66±0.06
	R^2	0.96±0.02	0.94±0.02	0.97±0.00

In the past, several groups have successfully used Langmuir models to fit experimental kinetic data of ligand exchange reactions and related processes.[85, 124-127] However, in the most cases such Langmuir models are used to calculate the adsorption rate of ligands on flat gold surfaces.[124-127] Kassam et al.[85] successfully fitted the kinetics of the ligand exchange of alkylthiols on 2.2 nm gold nanoparticles using a second-order Langmuir diffusion-limited model. They observed that only this Langmuir model yields an excellent fit, whereas other Langmuir models (first- and second-order Langmuir model and first-order Langmuir diffusion-limited model) failed. This result motivated us to test the suitability of Langmuir models also for the description of the kinetics of the present system. In a classical Langmuir model $\theta(t)$ is the time-dependent fractional coverage of the surface, where it is assumed that all active sites are equivalent and independent to each other.[127] In the present ligand exchange process, $\theta(t)$ is the fraction of the incoming thiol ligands, which are already chemically bound on the gold surface. The adsorption rate can be described by a generalized Langmuir model (see Equation 4.3),

$$\frac{d\theta(t)}{dt} = k.c(1 - \theta(t))^x$$

4.3

where the coefficient x is the order of the Langmuir model and c is the concentration of the ligand that is assumed to be constant, and k is a constant. It is assumed that the number of surface-bound mono-, di-, or trivalent thiol ligands is proportional to the number of released pyrene thiol from the gold surface. Thus, the number of surface-bound mono-, or multivalent thiol ligands is proportional to the increase in fluorescence intensity $I(t)$. This implies that $\theta(t)$ is proportional to $I(t)/I_0$ in Equation 4.3. Hence, Equation 4.3 can be replaced by Equation 4.4:

$$\frac{d\frac{I(t)}{I_0}}{dt} = k.c(1 - \frac{I(t)}{I_0})^x$$

4.4

For a first order Langmuir process, x in Equation 4.4 is 1. Then the adsorption rate is proportional to the number of available sites, which in the present case corresponds to the number of pyrene thiol ligands that are still bound to the gold surface. Integration of Equation 4.4 yields the mono-exponential function Equation 4.5 which is equivalent with Equation 4.1.[124]

$$I(t) = I_0(1 - e^{-k_{L1}t})$$

4.5

In Equation 4.5 $k_{L1} = k \cdot c$ is the rate constant. However, a fit of our experimental data to such a mono-exponential function agrees only poorly with the experimental data as shown above (see Figure 4.7 and Table 4.2).

For a second order Langmuir process, x in Equation 4.4 will be set to 2, and then the adsorption rate is proportional to the number of bound pyrene thiol ligands and according to a model of Yan et al.[127] to the number of physisorbed thiol ligands on the gold surface which is also proportional to $(1-\theta(t))$. Then the time dependent concentration $I(t)$ is:

$$I(t) = \frac{I_0 k_{L2} t}{1 + k_{L2} t}$$

4.6

where $k_{L2} = k \cdot c$ is the rate constant.

A fit of the experimental data obtained from the exchange reaction of pyrene thiol against monovalent thiols on Au-small nanoparticles with a second-order Langmuir model according to Equation 4.6 is shown in Figure 4.10. The fit and the experimental data agree well and $R^2 = 0.97$. The I_0 value for the example curve shown in Figure 4.10 is $(1.69 \pm 0.00) \cdot 10^5$, correspond to the concentration of the pyrene thiol according to the calibration curve shown in Figure 4.4b is $(2.58 \pm 0.66) \cdot 10^{-6}$ M. This value agrees within the experimental error with the concentration of the pyrene thiol bound on the nanoparticles before the ligand exchange reaction, which is $(2.79 \pm 0.31) \cdot 10^{-6}$ M (see above).
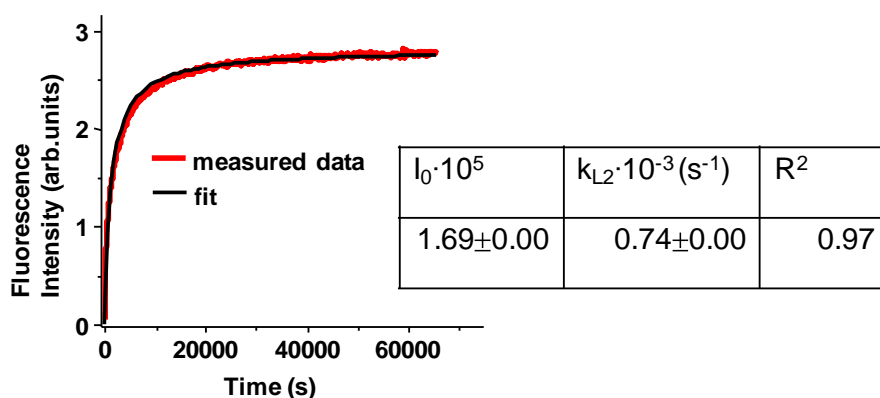

	$I_0 \cdot 10^5$	$k_{L2} \cdot 10^{-3} (s^{-1})$	R^2
	1.69 ± 0.00	0.74 ± 0.00	0.97

Figure 4.10: Changes in fluorescence intensity at 376 nm as a function of time for the ligand exchange reaction of monovalent thiols against pyrene thiol bound on Au-small nanoparticles fitted by a second order Langmuir model according to Equation 4.6.

Application of this second order Langmuir model (Equation 4.5) gives also good agreement between fit function and experimental data for the exchange of pyrene thiol ligands against di- and trivalent alkyl ligands on Au-small particles, where R^2 lies in the range of 0.93-0.98. For the Au-medium particles, the quality of such a fit is poor with R^2 values in the range of 0.74-0.84. The exchange rate k_{L2} of the trivalent or divalent thiols against the pyrene thiol are higher than that of the monovalent ones on Au-medium particles. However, in the case of the Au-small particles the exchange rate k_{L2} of the trivalent thiol is much slower than that of the monovalent one. Similar trends are obtained from using a bi-exponential fit function (see above). However, the R^2 values for the medium size particles are significantly smaller than one and hence, the

results from this second order Langmuir model are not considered in the further discussion of the ligand exchange kinetics.

Table 4.5: Rate constants for the exchange of pyrene thiol with mono-, di-, and trivalent thiol ligands on Au-small and Au-medium nanoparticles obtained from the second order Langmuir fit equation (see Equation 4.5)

Particle	Fit Parameters	Ligand		
		Trivalent thiol (1.26 mM)	Divalent thiol (1.89 mM)	Monovalent thiol (3.78 mM)
Au-medium (3.2±0.7 nm)	$k_{L2} \cdot 10^{-3}$ (s^{-1})	2.33±0.27	1.76±0.48	1.07±0.15
	$I_0 \cdot 10^5$	1.89±0.05	1.92±0.12	1.81±0.09
	R^2	0.83±0.03	0.74±0.08	0.84±0.05
Au-small (2.2±0.4 nm)	$k_{L2} \cdot 10^{-3}$ (s^{-1})	0.55±0.07	2.26±0.04	0.75±0.03
	$I_0 \cdot 10^5$	1.69±0.04	1.66±0.05	1.69±0.06
	R^2	0.96±0.01	0.93±0.01	0.98±0.01

As the first- and second- order Langmuir models did not yield fits of sufficient quality, diffusion-limited Langmuir model are also considered. In diffusion-limited Langmuir models, an additional term for the flux $J_A(t)$ of the incoming ligands is considered. Thus, the adsorption rate is also proportional to $J_A(t)$.[127] Therefore, the diffusion-limited Langmuir model can be described by Equation 4.7.[127]

$$\frac{d\frac{I(t)}{I_0}}{dt} = k' \cdot J_A (1 - \frac{I(t)}{I_0})^x = kc(1 - \frac{I(t)}{I_0})^x t^{-1/2}$$

4.7

The flux $J_A(t)$ is proportional to the concentration of the ligands c and reciprocally proportional to the square root of the time ($t^{-1/2}$) and k' and k are constants. Integration of Equation 4.7 with x=1 (first order diffusion-limited Langmuir model) yields Equation 4.8.

$$I(t) = I_0(1 - e^{-2k_{LD1}t^{1/2}})$$

4.8

where $k_{LD1}=k.c$ is the rate constant.

A first order Langmuir diffusion-limited model gives agreement between fit and experiment for the ligand exchange reaction with monovalent thiols on Au-small particles see the fit in Figure 4.11 where R^2 is 0.99.

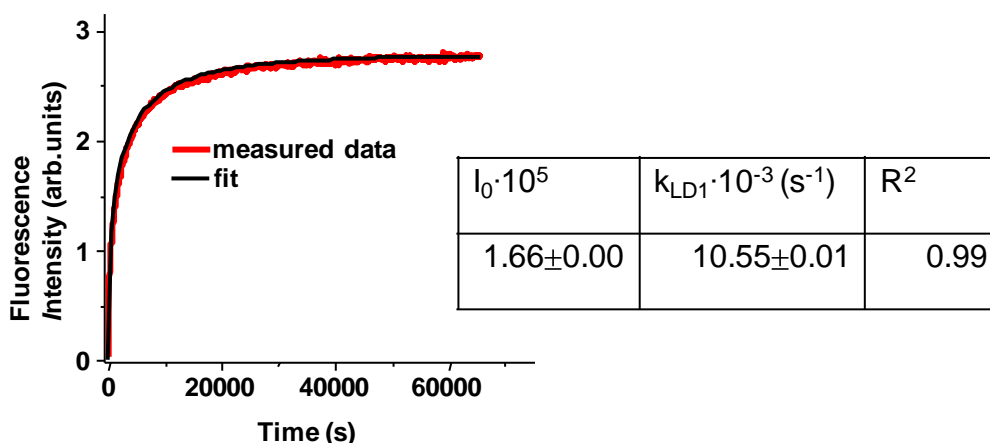| $I_0 \cdot 10^5$	$k_{LD1} \cdot 10^{-3}$ (s^{-1})	R^2
1.66±0.00	10.55±0.01	0.99

Figure 4.11: Changes in fluorescence intensity at 376 nm as a function of time for the ligand exchange of pyrene thiol with monovalent thiol ligands on Au-small fitted by a first order diffusion-limited Langmuir model (see Equation 4.8).

The rate constants for the exchange of mono- and multivalent thiols against pyrene thiol on Au-small and Au-medium particles obtained from a first order diffusion-limited Langmuir model according to Equation 4.8 are shown in Table 4.6. R^2 values between 0.92 and 0.99 reflect good agreement between the first order diffusion-limited Langmuir model and experimental data for the Au-small particles. However, for the Au-medium particles the quality of the fit is not sufficient and R^2 values in the range of 0.75-0.88 are derived. Because of these poor R^2 values the result from fitting the experimental data by a first order diffusion-limited model are not taken into account.

Table 4.6: Rate constants, I_0 values, and correlation coefficients of the exchange of mono-, and multivalent ligands against pyrene thiol on Au-small and Au-medium nanoparticles obtained from a first order diffusion-limited Langmuir model according to Equation 4.8

Particle	Fit Parameters	Ligand		
		Trivalent thiol (1.26 mM)	Divalent thiol (1.89 mM)	Monovalent thiol (3.78 mM)
Au-medium (3.2±0.7 nm)	$k_{LD1} \cdot 10^{-3}$ (s^{-1})	17.12± 1.03	14.42± 2.34	11.58± 0.81
	$I_0 \cdot 10^5$	1.85±0.04	1.91±0.13	1.80±0.08
	R^2	0.84±0.03	0.75±0.09	0.88±0.04
Au-small (2.2±0.4 nm)	$k_{LD1} \cdot 10^{-3}$ (s^{-1})	8.85±0.68	17.46±1.54	10.71±0.30
	$I_0 \cdot 10^5$	1.67±0.04	1.65±0.05	1.66±0.06
	R^2	0.99±0.01	0.92±0.02	0.99±0.01

The integration of Equation 4.6 with x=2 gives Equation 4.9, corresponding to a second order Langmuir diffusion-limited model.

$$I(t) = \frac{I_0 \cdot k_L \sqrt{t}}{1 + k_L \sqrt{t}}$$

4.9

where $k_L = k.c$ is the rate constant

Results from fitting the ligand exchange kinetics of mono- and multivalent thiols on Au-medium and Au-small gold particles by a second order Langmuir diffusion-limited model fit are summarized in Table 4.7. The obtained R^2 values in the range between 0.94 and 0.99, show good agreement with the experimental data. A representative fit of the kinetics of the exchange of pyrene thiol against monovalent thiols on Au-small nanoparticles is displayed in Figure 4.12, where R^2 is 0.97.

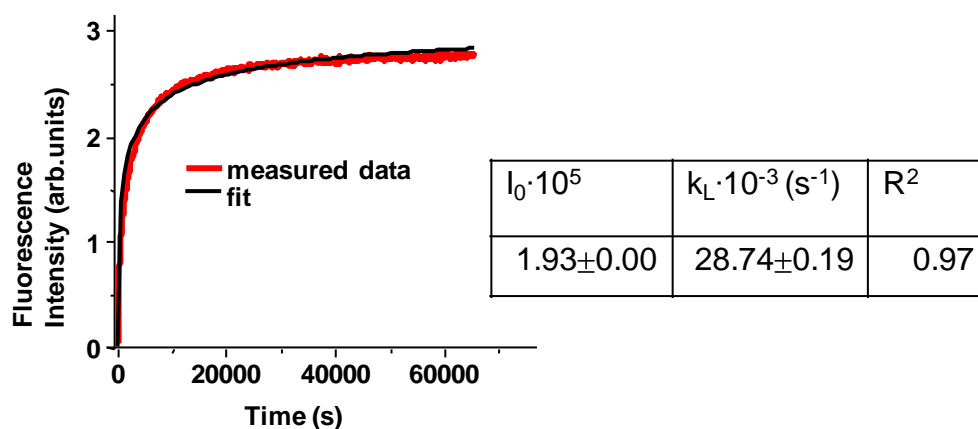| $I_0 \cdot 10^5$	$k_L \cdot 10^{-3}$ (s^{-1})	R^2
1.93±0.00	28.74±0.19	0.97

Figure 4.12: Changes in fluorescence intensity at 376 nm as a function of time for the ligand exchange of pyrene thiol with monovalent alkyl thiol ligands on Au-small fitted by a second order diffusion-limited Langmuir model (Equation 4.9).

A comparison of the reaction rates k_L from Table 4.7 reveals that the trivalent thiol on Au-medium size nanoparticles exchanges 1.77 times faster against pyrene thiol than the monovalent thiol. The exchange rate of the divalent thiol against pyrene thiol on Au-medium size particles is 1.46 times higher than the exchange rate of the monovalent thiol. On the Au-small size nanoparticles, the divalent thiol exchanges 2.25 times faster than the monovalent one. However, the k_L value of the trivalent thiols is about 1.29 times lower than k_L of the monovalent thiol. The reasons for this effect are explained below in Section 4.1.3.5.

Table 4.7: Rate constants, I_0 values, and correlation coefficients of the exchange reaction of mono-, and multivalent alkyl thiol ligands against pyrene thiol on Au-small and Au-medium nanoparticles obtained from fitting the experimental data by a second order diffusion-limited Langmuir model (see Equation 4.9)

Particle	Fit Parameters	Ligand		
		Trivalent thiol (1.26 mM)	Divalent thiol (1.89 mM)	Monovalent thiol (3.78 mM)
Au-medium (3.2±0.7 nm)	$k_L \cdot 10^{-3}$ (s^{-1})	61.54± 5.78	50.83± 7.67	34.67± 3.61
	$I_0 \cdot 10^5$	2.02±0.40	2.09±0.13	2.04±0.11
	R^2	0.98±0.01	0.94±0.03	0.98±0.01
Au-small (2.2±0.4 nm)	$k_L \cdot 10^{-3}$ (s^{-1})	22.71±2.84	66.3±8.42	29.4±1.20
	$I_0 \cdot 10^5$	1.97±0.07	1.78±0.04	1.92±0.06
	R^2	0.99±0.01	0.97±0.01	0.96±0.01

Fitting the experimental data with various models reveals that only the bi-exponential and the second order Langmuir diffusion-limited fit function yields good agreement between experiment and model function, whereas other fit models (mono-exponential, first and second order Langmuir and first order Langmuir diffusion–limited equations) cannot be used to describe sufficiently a part or all experimental data. Hence, only the results from the bi-exponential and the second order Langmuir diffusion-limited functions are considered in the further discussion. The multivalent enhancement factors, that are the ratio between the multivalent and the monovalent rate constants for the ligand exchange reaction on Au-small and Au-medium nanoparticles, are summarized in Table 4.8. The multivalent enhancement factors of the di- and trivalent thiols obtained from applying both fit functions, which are within the experimental error identical on Au-medium size particles. The fact, that the rate constant of the trivalent thiol is not enhanced might be explained by steric hindrance of the trivalent thiol which effectively hinders its penetration through the ligand shell and hence, significantly reduces the reaction rate. Notably, this result does not necessarily imply that only two thiol groups of the trivalent thiol ligands can bind to the gold nanoparticles, since the concentration of thiol groups is kept constant

and not the ligand concentration. Thus, if all the trivalent thiol ligands were bound only with two thiol groups, each trivalent thiol would replace only two pyrene thiol ligands from the gold surface. Consequently, if the concentration of thiol groups remains constant and it is assumed that the number of gold-thiol bonds per particle also remains constant, the trivalent thiols would replace only $^2/_3$ of the pyrene thiol ligands which would be replaced by the divalent thiols under identical conditions. As a result, the rate constant of the trivalent thiols should be considerably lower than that of the divalent thiols. Regarding the small size nanoparticles, a comparison of the rate constant reveals that the trivalent thiols exchanges much slower than the monovalent thiol exchanges against the pyrene thiol. The reason for this is explained below in Section 4.1.3.4. However, the divalent thiol exchanges 4.16±0.78 times faster according to the bi-exponential model and 2.26±0.38 time faster according to the second order Langmuir diffusion-limited model than the monovalent thiol exchanges with pyrene thiol. The reasons why the multivalent enhancement factor of the divalent thiol on Au-small particles is almost twice as high as on Au-medium particles are explained in greater detail in Figure 4.15 (see Section 4.1.3.4).

Table 4.8: Comparison of the multivalency enhancement factors, i.e., the ratio between the multivalent and the monovalent rate constants calculated from either the k_1 or the k_L values on medium-sized (Au-medium) and small-sized (Au-small) gold nanoparticles by using either a bi-exponential fit function (see Equation 4.2) ratio or a second order diffusion-limited Langmuir model (see Equation 4.9).

Particle	Ratio of rate constants (bi-exponential fit function with fixed amplitude ratio $I_{f,1}/I_{f,2}=2.5$))		Ratio of rate constants (second order diffusion-limited Langmuir model)	
	Trivalent/Monovalent thiol	Divalent/Monovalent thiol	Trivalent/Monovalent thiol	Divalent/Monovalent thiol
Au-medium (3.2±0.7 nm)	2.25±0.83	2.16±0.61	1.77±0.35	1.47±0.37
Au-small (2.2±0.4 nm)	0.90±0.10	4.16±0.78	0.77±0.13	2.26±0.38

4.1.3.3. Particle size effects

Particle size effects on the ligand exchange kinetics were investigated using mono- and multivalent alkyl thiols binding to gold nanoparticles of three different sizes: 2.2±0.4 nm (Au-small), 3.2±0.7 nm (Au-medium), and 4.4±0.9 nm (Au-large). The surface curvature of the smaller particles is increased, and therefore, it is expected that the binding of mono- and multivalent thiol ligands on the particle surface should be strongly influenced by the particle size. Figure 4.13 (a) shows the fluorescence intensity at 376 nm as a function of time for the first 500 s of the ligand exchange reaction for the mono-, and multivalent ligands against pyrene thiol on Au-small and Au-medium particles. The kinetics curves in Figure 4.13(a) clearly indicate that for identical incoming thiol molecules the rate of the initial ligand exchange on the Au-small particles (2.2 nm) is significantly lower than on the Au-medium particles (3.2 nm). Figure 4.13(b) depicts the kinetics of the ligand exchange reaction over a wider time frame. After about 16 h the fluorescence intensity of all samples is identical within the experimental error, regardless of the ligand type and particle size. This supports the assumption that a reversible reaction can be excluded and a complete exchange takes place on the Au-small nanoparticles. The Au-small nanoparticles reach the same final fluorescence intensity as Au-medium nanoparticles, which correspond to the total amount of pyrene thiol molecules bound to the nanoparticles ($2.79±0.31·10^{-6}$ M). The rate constants obtained by using bi-exponential (Equation 4.2) and second order Langmuir diffusion-limited (Equation 4.9) fit functions to fit the exchange kinetics on Au-small and Au-medium particles are summarized in Tables 4.4 and 4.7. The reaction rates are significantly slower for Au-small particles than for the Au-medium particles. Remarkably, for the Au-small particles the rate constants are lower for the trivalent thiol than for the monovalent thiol.
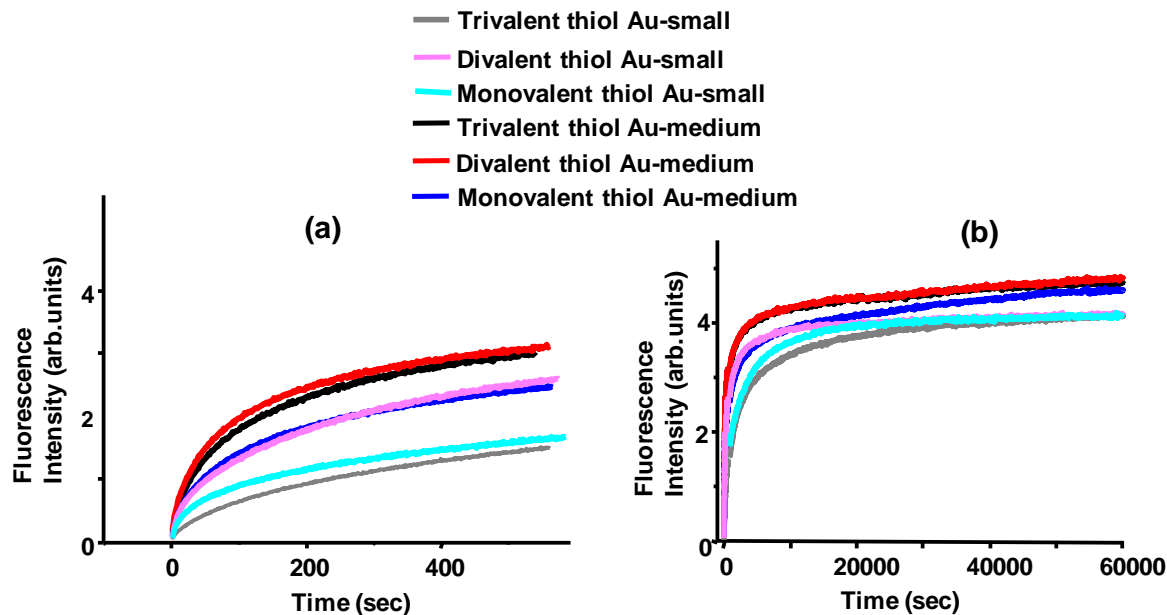
Figure 4.13: (a) Changes in the fluorescence intensity at 376 nm as a function of time for the initial period of the exchange of pyrene thiol with mono-, di-, and trivalent thiols on Au-small (2.2±0.4 nm) nanoparticles. Curves for Au-medium (3.2±0.7 nm) nanoparticles are included for comparison; (b) kinetics of the same reactions in a wider time scale.

Finally, the ligand exchange kinetics was investigated for particles with an average diameter of 4.4 nm (Au-large). These particles showed partial precipitation during the exchange reaction studies, probably due to insufficient surface stabilization of the gold nanoparticles after ligand exchange. The aliphatic thiol ligands which replace pyrene on the particle surface are less bulky than the pyrene thiol and hence, may not provide sufficient steric stabilization. This effect becomes more significant as the particle size increases. As a consequence, at larger particle sizes, only incomplete exchange reactions are observed. For a comparison, the initial (first 80 s) of the exchange kinetics curves for the mono- and multivalent ligands against pyrene thiol on Au-small, Au-medium and Au-large particles are displayed in Figure 4.14. A quantitative analysis of the initial 80 s of the exchange kinetics data of the samples Au-small, Au-medium and Au-large was not possible. The application of a bi-exponential fit function with free or fixed amplitudes (see Equation 4.2) as well as a second order Langmuir diffusion-limited fit function (see Equation 4.9) results in different I_0 values for differently sized nanoparticles. This is in contradiction to

those results which are obtained from the same data analysis and fit functions over longer time periods (see Section 4.1.3.2). This result indicates that the kinetics data of the initial time period are insufficient to describe the complete ligand exchange process properly. The use of a mono-exponential fit function is also not possible since it does not adequately model the experimental data (see Section 4.1.3.2). However, in agreement with the results discussed above, the kinetics data in Figure 4.14 clearly show that the rate of the ligand exchange systematically increases with particle size. This is also true in the case of Au-large particles, where the ligand exchange by the multivalent thiols is significantly faster than with the monovalent thiols.
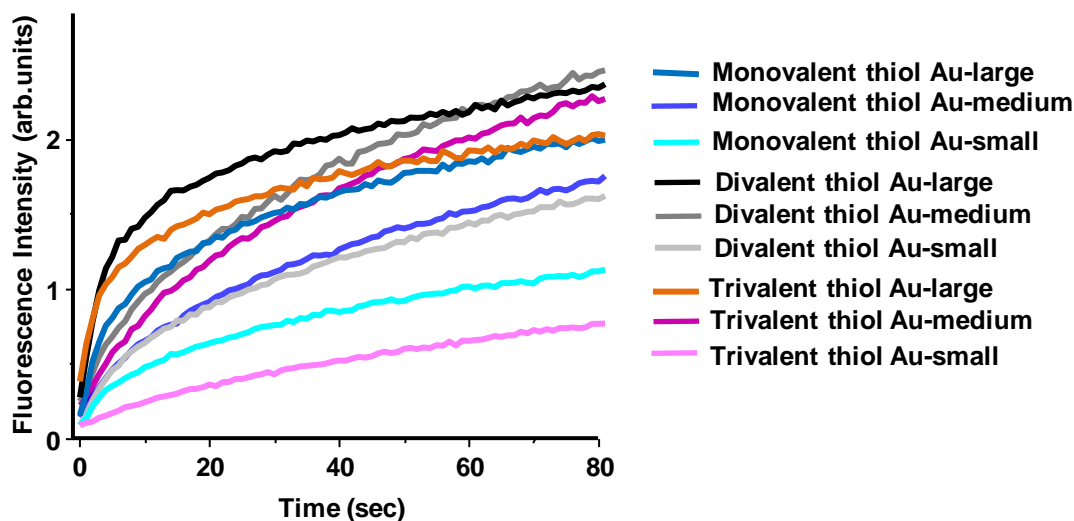

Figure 4.14: Changes in the fluorescence intensity at 376 nm as a function of time for the initial part of the ligand exchange reaction of divalent and monovalent thiols on Au-small (2.2±0.4 nm), Au-medium (3.2±0.7 nm), and Au-large (4.4±0.9 nm) nanoparticles.

In all cases investigated in the present work, the reaction rate increases with particle size (see Figure 4.14). In contrast, Guo et al.,[24] observed that for the exchange of phenylethanethiolate by *p*-nitrothiophenol on small Au_{38} and Au_{140} clusters, the initial ligand exchange is independent of the cluster size. This is explained by the fact that the initial ligand exchange mainly takes place at the nanocrystal vertices. In addition, the rates of later stages of ligand exchange are significantly lower for Au_{140} than on Au_{38}, which is ascribed to their increased terrace-like surface atom content.[83] It has been clearly shown in previous works on clusters[24, 128, 129] that the ratio of

terrace/face to edge/vertex sites is size dependent. Kell et al. reported that the reactivity of gold nanoparticles with average gold core sizes of 1.7 nm, 2.2 nm, and 4.5 nm functionalized by aryl ketones decreases with increasing particle size.[93] However, Wan et al. observed for gold nanoparticles of 5-20 nm a higher efficiency of the polymerase chain reaction on larger particles than on smaller sized nanoparticles.[94] The results observed by Wan et al.[94] are similar to the results presented in this Section that the reaction rates are increasing with increase in particle size.

The present experimental results are well-described by bi-exponential and second order diffusion-limited fit functions. In order to explain the molecular processes justifying the application of these functions, two different models are discussed in the following: a cooperative model which corresponds to a bi- or multi-exponential fitting function and a diffusion model for explaining a kinetic process described by a second order diffusion-limited Langmuir model.

4.1.3.4. Cooperative model

In all cases the reaction rate was found to increase with particle size (see Figure 4.14), apparently contradicting the increased reactivity of small particles observed by Kell et al.,[93] and Guo et al..[24] This observation might be explained by applying a theoretical model developed by Montalti et al..[27] According to this model the ligand displacement of pyrene thiol by functionalized thiols bound to a gold surface occurs through the interaction between several ligands. It is assumed that pyrene thiol ligands form stacked layers on gold surfaces, where all molecules have almost the same tilt angle, maximizing intermolecular pyrene-pyrene interactions.[117, 130] As a result, the insertion of a thiol weakens the thiol-gold bond of several neighboring pyrene thiol ligands. This result clearly implies that in the rate determining step the competing thiol weakens the pyrene thiol-gold bond of more than one pyrene thiol molecule on the gold nanoparticles. The observed experimental results can be explained by using a simplified model of an ideal icosahedral structure for the nanoparticles, as depicted in Figure 4.15. The yellow circle depicts a competing thiol ligand which displaces a pyrene thiol ligand from the surface of the gold nanocrystal (step (a)). It has been assumed that this cooperative effect is less

marked if the nanoparticles are smaller, since for small nanocrystals the area of the face sites are smaller and the edges are shorter than in larger particles (see Figure 4.15(a)). Consequently, the regions, where pyrene thiol ligands stack with the same orientation are particle size-dependent. An incoming ligand weakens on average a decreasing number of pyrene thiol molecules, if the particle size is decreased (see Figure 4.15(a), (b)). If a second thiol ligand is exchanged on the gold particle surface, the probability that it will be bound in a region where the pyrene thiol ligand shell is already weakened is increased with decreasing particle size (Figure 4.15(c), (e)). The binding of another thiol ligand is more probable and the rate constant of the process is increased. If the incoming ligand is divalent (see Figure 4.14(d), (f)), the second thiol group will bind to a gold atom adjacent to the one at which the first thiol group bound. This expectation comes from geometrical arguments, since the distance between two gold atoms on a nanoparticle is of the order of 220-260 pm.[131] The distance between the two gold atoms is similar to the distance between the two thiol groups in the divalent thiol, which is known to be 254 pm.[131] Consequently, in this case the cooperative weakening effect is high and the binding of the second thiol group of the divalent thiol is enhanced relative to that of a second monovalent thiol, in agreement with the present results on ligand exchange kinetics (see Tables 4.4, 4.7, and 4.8 and Fig. 4.14). The preference to divalent binding (chelation) of the second thiol group, compared to a monovalent process increases with decreasing particle size. This can be explained by assuming that the probability that an incoming second monovalent thiol displaces those pyrene molecules where the gold-thiol bond is already weakened is lower on a smaller nanocrystal than on a larger nanocrystal. (see Figure 15(c), (e)). This is in agreement with the observation that the multivalency effect of the divalent thiol is higher for Au-small particles than for Au-medium particles (see Table 4.8).

It should be considered that a competing thiol from the solution more likely will bind to a vertex, a generic surface defect, or to one of the edges of the nanocrystal, than to the crowded center of a face site, as depicted in Figure. 4.15.[130] However, for the Au-medium particles the fraction of vertex atoms, where no cooperative effect is possible, accounts only for about 3% of the surface atoms, if the particle geometry is assumed to be of perfect icosahedral shape. The corresponding values for the Au-small and Au-large particles are 7% and 1.5%, respectively. In addition, steric hindrance has to be considered to explain the reaction rates on highly curved particles. Thus,

nanocrystals of small diameter have a high proportion of surface atoms of either edge- or vertex sites. In the case of trivalent thiols, binding of to an edge- or vertex-site with all three functional groups is not possible due to geometric reasons. Similarly, for a divalent thiol the possibilities for stable binding of both thiol groups are limited, if one thiol group is bound to an edge-site, a vertex-site, or a defect site, such as an adatom. Consequently, for the Au-small particles the reaction rate of the trivalent thiol is even lower than for the monovalent thiol. The observed result that di- and trivalent thiols have same rate constant on Au-medium particles and that the rate constant for divalent thiol is lower on the Au-small particles compared to the Au-medium particles can be satisfactorily explained by simple geometric arguments. Taking into account all these considerations, the present model does not contradict to the previous work from Guo et al..[24] In this study, the authors exchanged thiol-bound phenyl ligands with short ethyl chains. Hence, a strong cooperative effect between phenyl and ethyl ligands is expected, which might explain the different dependence of the particle size of both processes.

This cooperative model is in full agreement with the bi-exponential model, which describes a ligand exchange process on nanoparticles. There, different reactivity at different particle sites, such as vertexes, edges, and defect sites, as well as binding sites on the nanoparticles with an enhanced weakening of the pyrene thiol−gold bond are due to strong cooperative effects. The consideration of cooperative interactions between pyrene thiol ligands also explains why the amplitude ratio I_{f1}/I_{f2} is not simply proportional to the ratio of the edge and vertex sites to the face sites of the gold nanocrystals (see above).
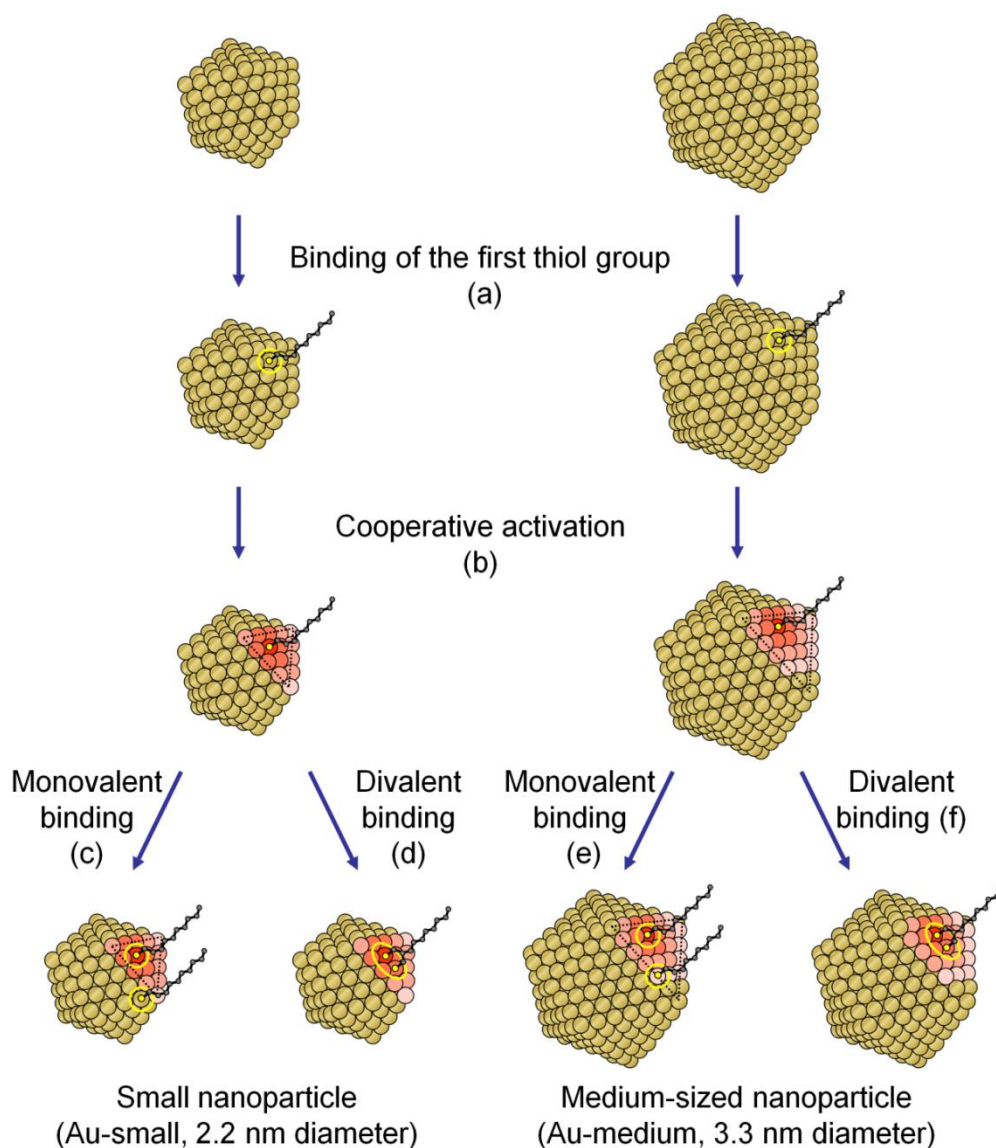
Figure 4.15: Schematic diagram of the cooperative model which explains multivalency and size dependent effects in the exchange of 4-pyrenebutyl-11-mercaptoundecanoate (pyrene thiol) with mono- and multivalent thiol ligands: The yellow circles depict an incoming thiol ligand which displaces a pyrene thiol from the surface of the gold nanocrystal (step (a)). As a consequence, the thiol-gold bond of the pyrene thiol ligands in the vicinity of the displaced pyrene thiol ligand are also weakened (step (b)). The intensity of the red color of the gold atoms qualitatively represents the degree of this cooperative weakening of binding at the gold atoms. Subsequently, either another monovalent thiol (yellow circle, step (c) or (e)) or the second thiol group of the divalent thiol binds to the gold surface in a sequential binding process (step (d) or (f)).

4.1.3.5. Diffusion model

The fit of the experimental results by a second order diffusion-limited Langmuir model (Equation 4.9) also gives good agreement. A schematic diagram of a possible model for the exchange of pyrene thiol bound on gold nanoparticles with mono- and multivalent alkyl thiol ligands according to a second-order Langmuir diffusion-limited model is shown in Figure 4.16. The incoming thiol ligands diffuse through the pyrene thiol ligand shell to the gold surface (see Figure 4.16(a)). Accordingly, it is assumed that this is the rate determining step, if this fitting model is correct. This adsorption rate is in the second order Langmuir process proportional to the number of bound pyrene thiol ligands, and according to a model of Yan et al., to the number of physisorbed alkyl thiol ligands on the gold surface.[127] Both quantities are proportional to 1-θ(t), where θ(t) is the time-dependent fractional coverage of the surface, where it is assumed that all active sites are equivalent and independent of each other.[124-127] Consequently, it might be assumed that, subsequent to the initial diffusion process (see Figure 4.16(a)), the thiol ligands physisorbed on the surface of the gold nanoparticles and displace the 4-pyrenebutyl-11-mercaptoundecanoate molecules on the gold surface (see Figure 4.16(b)). Then, the multivalent thiols are chemisorbed on the gold surface and free pyrene thiol molecules are released into solution (see Figure 4.16(c)).

However, a second order diffusion-limited Langmuir model does not allow us to explain the size and multivalency dependences of the exchange kinetics for the following reasons:

(i) The diffusion-limited Langmuir model implies that the diffusion of the multivalent thiols will determine the reaction rate. Since the multivalent thiols are significantly bulkier than the monovalent ones, it is expected that they diffuse slower through both, the solvent and the pyrene thiol ligand shell because the diffusion constant is inversely proportional to the hydrodynamic diameter.[132] In addition, bulkier thiols can more easily become entangled with surface ligands. However, the experimental results indicate an opposite dependence of ligand exchange kinetics on the thiol multivalency. Moreover, penetration of a thiol ligand through the shell of surface-bound pyrene thiol ligands should be enhanced if the particle surface is significantly curved. If the surface coverage of the nanoparticles is identical, the end groups sticking into the solvent

have a larger distance. This is evidently not in agreement with the observed particle size dependence of the ligand exchange process. If a rate determining diffusive term is not taken into account, which implicates that a first or second order Langmuir model is applied, the model function does not fit the experimental data, as explained in the Section 4.1.3.2.

(ii) In a Langmuir model binding of the incoming thiol at all active sites are assumed to occur independently of each other. This model does not explain why the divalent thiol binds more rapidly than the monovalent thiol. Moreover, if all binding sites are equivalent there should be no differences in reactivity of edge-, vertex-, face-, and defect sites so co-operative effects between several binding sites cannot be explained. Accordingly, the reaction rate of ligand exchange process will be independent of nanocrystal size. This is contradictory to the experimental results, which indicate that the reaction rates decrease with decreasing particle size.
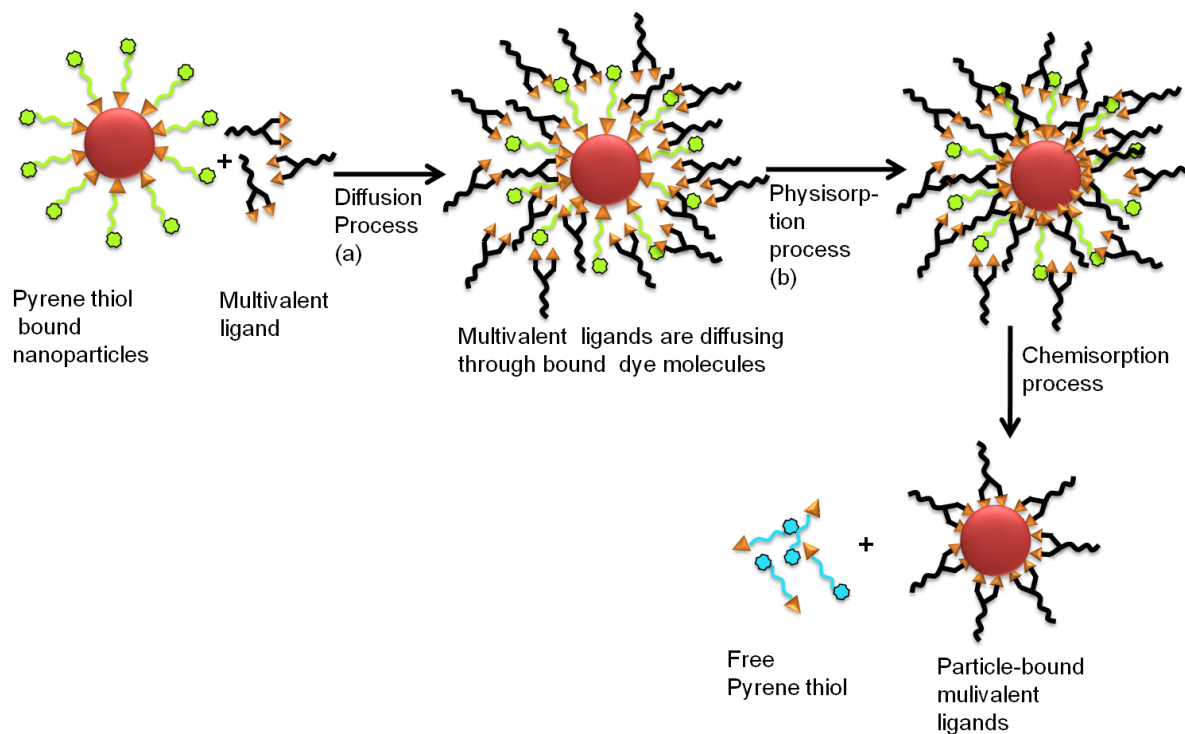
Figure 4.16: Schematic diagram of the ligand exchange process according to a second-order Langmuir diffusion-limited model: (a) Competing ligands diffusing through the ligand shell in a rate-determining step; (b) multivalent ligands undergoing physisorbtion on the gold surface; (c) multivalent ligands displacing the pyrene thiols, and undergoing chemisorption on the nanoparticles surface.

These considerations indicate that although a second order diffusion-limited Langmuir model fits the experimental data well and has been used before by Kassam et al.,[85] the effects predicted by this model are not in agreement with the experiment results observed here. Therefore, this model is discounted and a bi- or multi-exponential model is rather favored, as it fully explains the experimental results, including the size and multivalency dependency of the kinetics.

4.1.3.6. Conclusion

In this Section, a novel approach to quantify the ligand exchange kinetics on gold nanoparticles of 2.2±0.4 nm (Au-small), 3.2±0.7 nm (Au-medium), and 4.4±0.9 nm (Au-large) diameter is discussed. Pyrene thiol ligands bound on the gold surface are exchanged with mono-, di-, and trivalent alkyl thiol ligands. Multivalency and particle size effects are elucidated using time resolved fluorescence spectroscopy. Various models are tried to explain the experimental results. All results from kinetics studies are well fitted by a bi-exponential function as well as a second order Langmuir diffusion model. The use of the bi-exponential is motivated by the assumption that different sites of the nanoparticles have different reactivities, which takes in small gold nanoparticles edge-, vertex-, face-, and defect-sites into account. The second order Langmuir diffusion model describes a diffusion-limited ligand exchange. Systematic investigations of the binding kinetics of the ligand exchange reactions of mono- and multivalent ligands on different sized gold nanoparticles reveal a significant enhancement of the reaction rate of tri- and divalent thiols compared to monovalent ones. In contrast, the exchange rates of the trivalent thiol ligands are similar or even lower than those of the divalent ones. This is explained by steric hindrance of trivalent thiol ligands. Furthermore, a clear particle size dependence of the ligand exchange rate constants is observed. The rate of the reaction increases with increase in particle size. The results are well explained by a cooperative model, where the exchange of one pyrene ligand causes a weakening of the gold-thiol bond of the pyrene thiol ligands in its vicinity. This cooperative mechanism is more effective on larger particles and promotes multivalent thiols binding. This model is in agreement with a bi-exponential fit model of the kinetics, since this model includes different reactivity of different particles sites. In contrast, a diffusion-limited process explains

neither the multivalency effect nor the particle size dependence of the ligand exchange process and is therefore discounted.

4.2. Investigation of binding of rigid aromatic thiol ligands on Au-small, Au-medium and Au-large particles

This Section details about the binding of mono- and divalent rigid aromatic thiols on gold nanoparticles with three different average diameters. To investigate the influence multivalency, rigidity, and particle size on the binding of thiols on gold nanoparticles, the commercially available 4-toluenethiol and 3,4-toluenedithiol are chosen as rigid mono- and divalent ligands respectively (see Figure 4.17). 4-Pyrenebutyl-11-mercaptoundecanoate (pyrene thiol) bound on Au-small (2.2 ± 0.4 nm), Au-medium (3.2 ± 0.7 nm), and Au-large (4.4 ± 0.9 nm) particles is exchanged by 4-toluenethiol and 3,4-toluenedithiol. Results of these ligand exchange experiments are discussed in this Section.

4.2.1. 4-Toluenethiol and 3,4-toluenedithiol (aromatic monovalent and divalent thiols)

4-Toluenethiol (Ar-monovalent thiol) and 3,4-toluenedithiol (Ar-divalent thiol) are used as received from the company (see Figure 4.17)
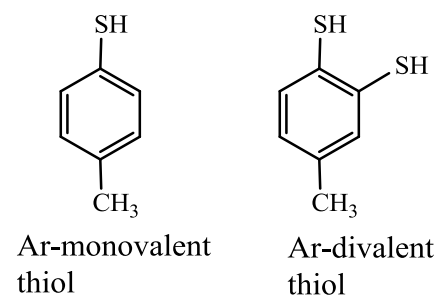
Figure 4.17: Chemical structure of the Ar-monovalent and Ar-divalent thiol.

4.2.2. Binding of aromatic thiols on different sizes of gold nanoparticles

The pyrene thiol (see Section 4.1.1.) on Au-small, Au-medium, and Au-large nanoparticles are exchanged by rigid aromatic thiols, Ar-monovalent and Ar-divalent thiols (see above Figure 4.17) to study the binding of rigid thiols on gold nanoparticles. The idea is to compare the results

of the binding kinetics of rigid thiols on different sizes of gold nanoparticles with the binding kinetics results of flexible thiols (see Section 4.1.3.). For this, the concentration of the competing rigid thiols and pyrene thiols on the particles was kept constant (see Section 4.1.3.). The concentrations of the competing thiols are maintained at 3.78 ± 0.02 mM in case of the monovalent (Ar-monovalent) and at 1.89 ± 0.02 mM in case of the divalent (Ar-divalent) thiol (see Table 4.1). The pyrene thiols bound to gold nanoparticles are maintained at a concentration of $2.79\pm0.31\cdot10^{-6}$ M. As described before in Section 4.1.3, the ligand exchange process was studied by measuring the fluorescence signal of the displaced pyrene thiol during the exchange with the aromatic rigid thiols. Immediately after the addition of the Ar-mono- and Ar-divalent thiol to a dilute dichloromethane dispersion of Au-small and Au-medium particle, either the color of the particles changed to violet or the particles precipitated out, due to aggregation.

In addition, the ligand exchange on particles with an average diameter of 4.4 ± 0.9 nm (Au-large) was also investigated. Here, also aggregation of nanoparticles is observed immediately after the addition of the Ar-mono- and Ar-divalent thiols.

The interactions of arene thiols with gold particles,[133, 134] clusters,[135] and surfaces[136] are well documented. However, the ligand exchange of arene thiols on gold nanoparticles with 1-4 nm in diameter has not yet been reported before. In the previous Section (Section 4.1.3.) the binding kinetics of flexible mono- and multivalent alkyl thiols on Au-small (2.2 ± 0.4 nm), Au-medium (3.2 ± 0.7 nm) and Au-large (4.4 ± 0.9 nm) particles were carried out using fluorescence spectroscopy. Immediate aggregation was not observed for particles of 2.2 ± 0.4 nm and 3.2 ± 0.7 nm in diameter. In contrast, for gold nanoparticles with 4.4 ± 0.9 nm in diameter precipitation was observed, and in this case only the initial part of the kinetics could be studied using fluorescence spectroscopy. But for the systems described in this Section, due to the immediate aggregation of the particles, kinetics studies of binding of rigid thiols are not feasible. Obviously, the rigid Ar-mono- and Ar-divalent thiols do not provide the same degree of steric stabilization as the bulky pyrene thiols and as the long-chain alkyl thiols studied in detail in Section 4.1, which explains the occurrence of aggregation during ligand exchange.

4.2.3. Conclusion

In this Section, the ligand exchange of pyrene thiols by rigid mono- and divalent aromatic thiols on gold nanoparticles by 2.2±0.4 nm (Au-small), 3.2±0.7 nm (Au-medium), and 4.4±0.9 nm (Au-large) diameter is discussed. However, aggregation occurs already immediately after the addition of the aromatic rigid thiol ligands. This is explained by the insufficient steric stabilization of gold nanoparticles with the rigid thiols after ligand exchange.

4.3. Binding kinetics of flexible thiol-functionalized multivalent ligands on silver nanoparticles

In this Section, binding kinetics of flexible mono- and multivalent thiol ligands (see Section 4.1.1) on silver nanoparticles is considered. Further, the results are compared to results obtained from binding of thiol-functionalized mono- and multivalent ligands on gold nanoparticles (see Section 4.1.3). Pyrene thiol stabilized silver nanoparticles are prepared in the same size regime as the gold nanoparticles which are discussed in Section 4.1.3. The pyrene thiols on the silver nanoparticles are exchanged by the same flexible mono- and multivalent thiol ligands as in Section 4.1.3. The concentration of pyrene thiol on particles and the concentrations of the incoming thiol are also maintained, as that used for kinetics studies on gold nanoparticles (see Table 4.1 and Section 4.1.3).

4.3.1. Synthesis of pyrene thiol-stabilized silver nanoparticles

The procedure for the synthesis of pyrene thiol stabilized silver is explained in detail in the Experimental section (Section 3.3). $AgNO_3$ in water is transferred to the organic phase using a phase transfer catalyst (TOAB). After that, the aqueous phase is discarded, and then the pyrene thiol is added to the organic phase followed by the addition of the reducing agent $NaBH_4$. The reduction of silver ions leads to pyrene thiol-stabilized silver nanoparticles. Subsequently, the particles are precipitated by addition of EtOH and centrifuged at 1000 g for 10 minutes. The supernatant is collected to calculate the amount of pyrene thiol bound on the particles (see Section 4.1.1). The washing procedure is repeated until the fluorescence signal from the dye in the supernatant become negligible. Thus, all free pyrene thiol ligands that are not particle-bound are removed. The TEM image of pyrene thiol-stabilized silver nanoparticle is shown in Figure 4.18, the respective particle diameter is 4.6±2.0 nm. Particles obtained from various syntheses consistently exhibit a near-spherical geometry, with polydispersity of around 30-45%.
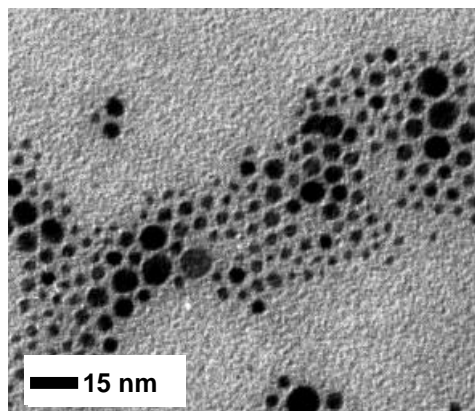
Figure 4.18: TEM image of pyrene thiol-coated silver nanoparticles.

It turned out that it was not possible to prepare silver nanoparticles smaller than 4.6 nm by this approach. Neither a change of the silver precursor, nor a change of the silver to thiol ratio allows for a further reduction of the particle diameter, as it was successfully described for gold nanoparticles (see Section 4.1). Also, in the literature comparable approaches always yield silver particles of at least 5 nm in diameter.

4.3.2. Study of the binding kinetics of thiol-functionalized multivalent ligands on silver nanoparticles.

To investigate the binding kinetics of mono-, and multivalent thiols on silver nanoparticles, pyrene thiol ($2.79\pm0.31\cdot10^{-6}$ M) bound on silver particles (see Figure 4.18) is exchanged against mono- (3.78 mM), di- (1.89 mM), or trivalent (1.26 mM) alkyl thiols. The time-resolved fluorescence intensity of the displaced pyrene thiols in solution are measured at 376 nm. During the exchange, partial precipitation of particles was observed, indicating incomplete reaction and aggregation of the particles (similar to the aggregation observed for the Au-large particles, see Section 4.1.2.). Therefore, a systematic investigation of the binding kinetics is not possible in case of silver nanoparticles. The initial part (first 90 s) of the exchange kinetics plots of mono-, di-, and trivalent thiols against pyrene thiol on silver nanoparticles with 4.6 ± 2.0 nm in diameter are depicted in Figure 4.19. From the kinetics curves shown in Figure 4.19 it is obvious that the

rate of ligand exchange is faster for multivalent ligands, than for the monovalent ones. From the kinetics curve shape it is obvious that I_0 values (the fluorescence intensity values, after the entire dye is released from the silver surface) will be different for the data shown in Figure 4.19 because significant aggregation takes place already in this early stage of the exchange reaction. Due to this, none of the fit functions discussed in Section 4.1.3 could be used to fit the experimental data.
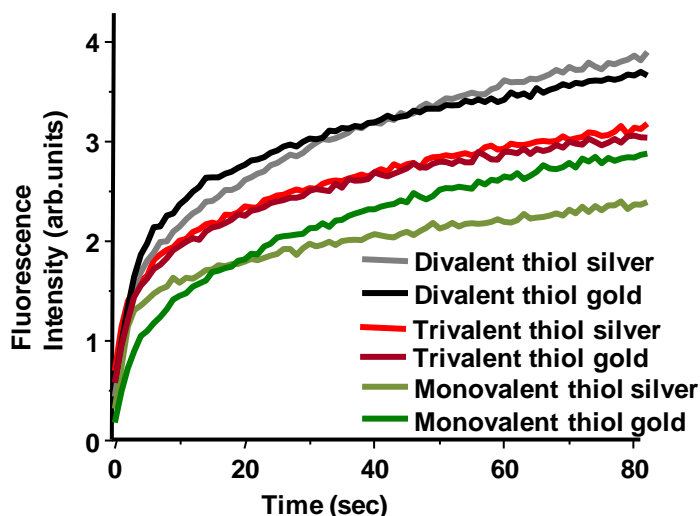
Figure 4.19: Changes in the fluorescence intensity at 376 nm for the exchange of pyrene thiol with mono-, and multivalent thiols on silver nanoparticles (4.6±2.0 nm diameter) and gold nanoparticles (4.4±0.9 nm diameter).

To the best of our knowledge, the binding kinetics of multivalent ligands on silver nanoparticles has not yet been reported. However, for the first time we have studied the binding kinetics of multivalent ligands on gold nanoparticles (see Section 4.1., also ref. [116]). This study on the binding kinetics on gold nanoparticles reveals that the multivalent ligands are exchanging more rapidly than the monovalent ones.[116] The kinetics data shown in Figure 4.19, also indicate that the ligand exchange rate increases with increasing multivalency of the ligands. Moreover, the results for the exchange kinetics of mono-, di-, and trivalent thiol ligands on 4.6±2.0 nm diameter silver particles resemble those observed for the same ligands with 4.4±0.9 nm diameter on gold nanoparticles (see Figure 4.19 and detailed discussion in Section 4.1.3. also ref. [116]). In both cases during ligand exchange reaction one observes a partial precipitation of the particles. This can be explained by the fact that the incoming mono-, di-, and trivalent thiols cannot

provide the same degree of steric stabilization as the pyrene thiol does. Moreover, the exchange rates of pyrene thiol with trivalent and divalent ligands are in same range on both, silver and gold nanoparticles. In case of the monovalent ligands, initially, the exchange rate on silver nanoparticles seems to be faster than on gold nanoparticles. However, after few seconds likely due to the faster aggregation of the silver particles with monovalent ligands, the exchange rates slow down and the exchange rates of pyrene thiol with monovalent ligands on gold nanoparticles become faster. This is due to the softer nature of gold which shows stronger affinity towards thiol ligands than the silver nanoparticles.[137]

4.3.3. Conclusion

In this Section, the ligand exchange kinetics of flexible thiols on silver nanoparticles of 4.6±2.0 nm diameter is discussed. Further, the results are compared with the results gathered during ligand exchange reaction on gold nanoparticles of 4.4±0.9 nm in diameter. Due to the insufficient steric stabilization of the particles with incoming mono- and multivalent thiols partial aggregation of the particles during the ligand exchange reaction is observed. However, the analysis of the initial part of the kinetics curves on both gold and silver particles reveals that the exchange rates of di- and trivalent ligands are faster than those of the monovalent ones. The comparison of the results shows that the exchange rates of pyrene thiols with di- and trivalent thiols on both, silver and gold nanoparticles are similar to each other. Due to the difference in nature of gold and silver, the exchange rates of monovalent ligands with pyrene thiol on silver particles is initially faster, in a later stage the exchange rates on gold nanoparticles appear faster which might be caused by different degrees of aggregation of gold and silver particles.

4.4. Controlled synthesis of platinum and silver nanoparticles using amine functionalized multivalent ligands

4.4.1. Introduction

Tuning of the shape, size, and size distribution of nanomaterials is of interest for controlling the properties of nanoparticles. This is because particles of different size and shape have different physical and chemical properties.[138] Particularly, in case of the noble metal nanoparticles, such as silver and platinum, the shape and size dependence is known.[139] Silver nanoparticles with different shape and size possess unique optical scattering responses. Symmetric spherical particles exhibit only a single scattering peak, whereas particles of anisotropic shape such as rods, triangular prisms, and cubes, exhibit multiple scattering peaks.[139] This is explained by the highly localized charge polarizations at the edges and vertices of metallic nanoparticles.[139] Further, the scattering from smaller particles less than about 50 nm in diameter is negligible[140] and mainly the absorption peak is observed for the particles with diameters larger than 2 nm.[16] A blue-shift of the surface plasmon resonance is observed for silver nanoparticles when the particles size decreases.[16] Platinum nanoparticles exhibit shape and size dependent catalytic properties, which are useful for highly selective catalytic processes.[141] Nanoparticles with different shapes are enclosed by different facets. Therefore, depending on the particle shape, different fractions of atoms are located at different sites, such as faces, corners, or edges. Thus, the catalytic properties of the particles, which have different shapes, are expected to be different in reactivity.[141] In general, platinum and silver nanoparticles are synthesized by different routes, such as reducing metal precursors in solution by colloidal methods,[16, 139] reducing metal precursors by bubbling gaseous hydrogen through the reaction mixture,[65] or by decomposing the precursors under high pressure.[138] During the synthesis of the particles, their shape and size can be controlled by changing the concentration of the reductant or ligands, by varying the metal precursor concentration,[65, 141] by changing the temperatures,[138] by using foreign ions, or by using a seeded growth procedure instead of a one-step reaction.[58, 141] Differences in the nature of the binding of ligands to the metal nanoparticle surface as well as differences in their binding

strength can lead to particles with different shape, and size. These are also responsible for the colloidal and chemical stability of the particles.[16, 58, 65, 138, 139, 141]

Experimental results obtained for noble metal particles prepared by using hydrogen reduction as well as high pressure approaches or two step syntheses, show that the controlled synthesis of nanoparticles with well-defined shape and size is rather complex.[58, 65, 138, 139, 141] Even though, monodisperse particles with a specific, anisotropic shape and a defined size can be in principle obtained from these approaches,[58, 65, 138, 139, 141] the exact relationship between synthesis parameters and morphology of the particles are not yet well understood. Even small, barely controllable variations in the synthesis often lead to undefined, polydisperse, and polymorphic systems.[16, 58, 65, 138, 139, 141]

In this work, amine functionalized mono- and multivalent ligands are used to prepare and to stabilize silver and platinum nanoparticles. The effects of mono- and multivalent amine ligands on the formation of platinum and silver nanoparticles are studied. For this purpose, platinum (II) acetylacetonate ($Pt(acac)_2$) and silver (II) acetylacetonate ($Ag(acac)_2$) are chosen as precursors. The effects of the multivalency of the ligands on the formation of nanoparticles are studied by preparing the particles in a one-step synthesis as well as by stepwise increasing the temperature during the reaction.

4.4.2. Amine functionalized mono- and multivalent ligands

The stabilizing ligands change the chemical and physical properties of nanoparticles.[16, 58, 65, 138, 139, 141] In reported procedures amines,[16, 138, 141, 142] thiols,[58] polymers,[65, 143] and oleic acid[144] are used to stabilize silver and platinum particles. Amine ligands are widely used in the preparation of silver and platinum nanoparticles because of the strong binding of amine ligands to both metals. Zhong et al. prepared relatively monodisperse platinum particles by reducing trans-$Pt(NH_3)_2Cl_2$ in the presence of oleylamine, or hexadecylamine at high temperatures.[145] Ren and coworkers succeeded in the synthesis of platinum nanoparticles of varying shape and size by the control of several variables in the reduction of $Pt(acac)_2$ in toluene under a pressure of 3 bar H_2 in the presence of oleylamine.[138] To the best of our knowledge multivalent ligands

have not been used to stabilize silver and platinum particles before. Recently, we have investigated the binding of multivalent ligands to gold nanoparticles (see Section 4.1).[116] Since multivalent ligands have more than one binding functional group, it has been shown that multivalent ligands stabilize nanoparticles more than the corresponding monovalent ones.[116] In this Section a novel approach to prepare platinum and silver nanoparticles stabilized by mono- and multivalent amines is presented. Here, amine functionalized mono- and multivalent ligands are employed to control the formation of silver and platinum nanoparticles. For this, the ligands are chosen in such a way that the lengths of the ligands are almost the same. Commercially available dodecylamine is chosen as a monovalent amine (see Figure 4.21), 1,1-bis(aminomethyl)nonane (see Scheme 4.4), and 1,1,1-tris(aminomethyl)nonane (see Scheme 4.5) are chosen as di- and trivalent amine ligands, respectively. The divalent and trivalent ligands are synthesized using reported procedures.[77]

a) Dodecylamine (Monovalent Amine)

The monovalent ligand, dodecylamine amine is commercially available and is used as received (see Figure 4.21)
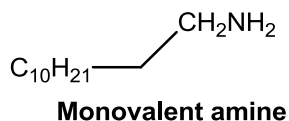
Monovalent amine

Figure 4.21: Dodecylamine (monovalent amine)

b) 1,1-Bis(aminomethyl)nonane[77] (Divalent Amine)

Methanesulfonyl chloride is treated with a chilled solution of 1,1-bis(hydroxymethyl)nonane in pyridine to get 1,1-bis(methylsulfonyloxy)nonane (**10**) which in turn is converted into the corresponding (1,1-bis(azidomethyl)nonane) **11** by treating **10** with NaN_3 (see Scheme 4.4). **11** is reduced by using $LiAlH_4$ to give the product divalent amine (12) with 53% yield.
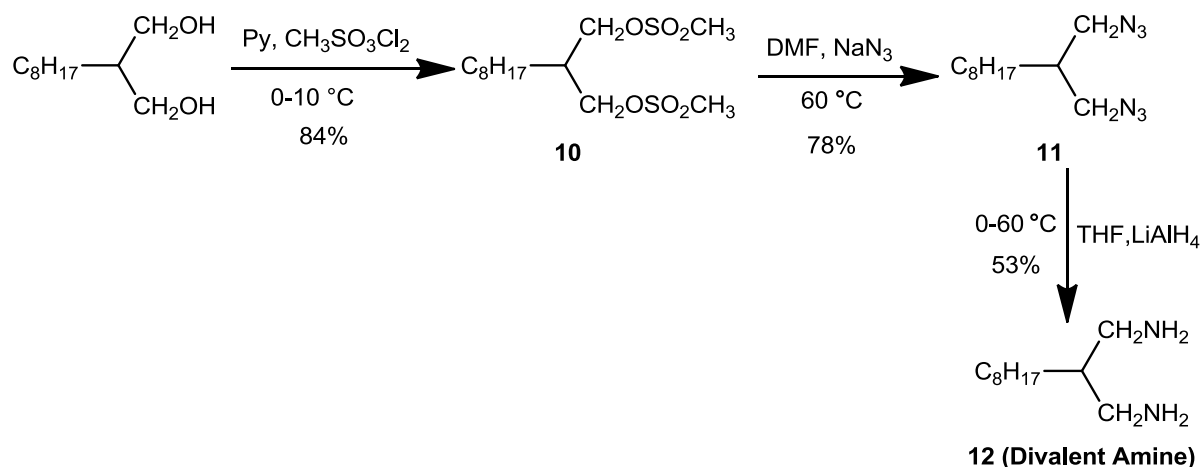
Scheme 4.4: Preparation of 1,1-bis(aminomethyl)nonane

c) 1,1,1-Tris(aminomethyl)nonane[77] (Trivalent Amine)

To a chilled solution of 1,1,1-tris(hydroxymethyl)nonane in pyridine, methanesulfonyl chloride is added to obtain **13** (see Scheme 4.5). When **13** (1,1,1-tris(methylsulfonyloxymethyl)nonane) in DMSO is treated with NaN_3 in the presence of TOAB, it affords 1,1,1-tris(azidomethyl)nonane **(14)**. Then, the resulting **14** is reduced by using $LiAlH_4$ to give 1,1,1-tris(aminomethyl)nonane **(15 trivalent amine)** as a product with 81% yield.
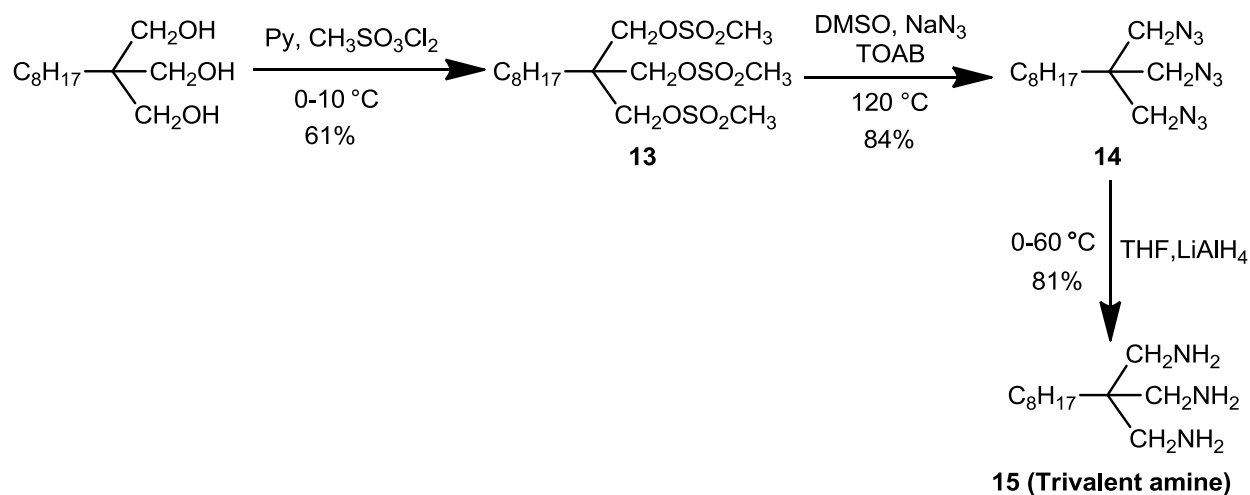
Scheme 4.5: Preparation of 1,1,1-tris(aminomethyl)nonane

4.4.3. Influence of mono- and multivalent ligands on the formation of platinum nanoparticles

In this Section the influence of amine functionalized mono- and multivalent ligands on the formation of platinum nanoparticle is discussed. The investigations are carried out by preparing the particles using a one-step synthesis at 200 °C or by stepwise increasing the temperature in the range from 160 °C to 200 °C in 10 K steps.

4.4.3.1. Platinum nanoparticles synthesized at 200 °C

The synthesis procedure presented here for preparing mono- and multivalent amine coated platinum particles at 200 °C is a simple one-step method. By using this method, well-defined platinum particles stabilized by mono- and multivalent ligands can be quickly prepared by thermal reduction of (Pt(acac)$_2$).

To Pt(acac)$_2$ in octyl ether, the mono- or, di-, or trivalent amine ligands and 1,2-hexadecandiol are added and the reaction mixture is heated to 200 °C. After this temperature is reached, the reaction mixture is heated for another 30 minutes in case of multivalent and for another 5 minutes in case of monovalent amines. After this time period, the reaction mixture is cooled down to room temperature and the nanoparticles are precipitated by the addition of ethanol. Then, the particles are isolated by means of centrifugation at 1000 g for 10 minutes and subsequently, the supernatant is removed. The particles are washed three times with ethanol to remove uncoated amine that is not particle-bound.

The influence of the ligand's multivalency on the formation of the platinum particles is investigated by analyzing during the particle synthesis e.g. the changes in color and the particle size by TEM measurements. When the reaction mixture reaches 200 °C during the preparation of the platinum particles, the color of the reaction mixture turns to blackish brown within 3 minutes, if monovalent amine ligands are used. In the presence of di- or trivalent amine ligands the color of the reaction mixture changes to blackish brown after 5 minutes at 200 °C. This change in color

indicates the spontaneous formation of nanoparticles. The as-prepared di- and trivalent amine ligands stabilized nanoparticles are further heated for 30 minutes at 200 °C, to make sure that all platinum precursors are consumed for nanoparticles formation. Subsequently, the reaction mixture is cooled down to room temperature. Black precipitates are found during longer heating of the spontaneously formed particles stabilized by monovalent ligands which shows that the particles start to aggregate. Therefore, the reaction mixture is allowed to cool already 3 minutes after significant particle formation is observed. Because of this aggregation of the particles stabilized by the monovalent amines, the dichloromethane dispersions of the particles are filtered via a PTFE syringe filter (0.2 μm) before preparing the TEM samples. In contrast, the TEM samples of the nanoparticles stabilized by di- and trivalent amine ligands are prepared from dichloromethane dispersions without any filtration. Platinum nanoparticles stabilized by mono- or multivalent amine ligands are stable in dichloromethane or as dried precipitate under argon for at least one month.

The shape and the size distribution of the particles are obtained from an analysis of TEM images (see Figure 4.22). The platinum nanoparticles stabilized by monovalent ligands have a polyhedral shape (Figure 4.22 (a)), whereas the particles stabilized by multivalent amine ligands have an almost spherical shape, see Figure 4.22 (b) and (c). For the polyhedral shaped particles, the longest diagonal and for the spherical particles the diameters are used to measure the size of the particles. The average size of the polyhedral, nanoparticles stabilized with the monovalent ligands is 5.7±0.6 nm. The average size of the spherical particles with a divalent ligand shell is 2.6±0.5 nm. The particles stabilized by trivalent ligands have a spherical shape with an average diameter of 3.6±0.4 nm. The formation of polyhedral and spherical particles with mono- and multivalent ligands in these size ranges has been reproduced within ±0.5 nm accuracy.
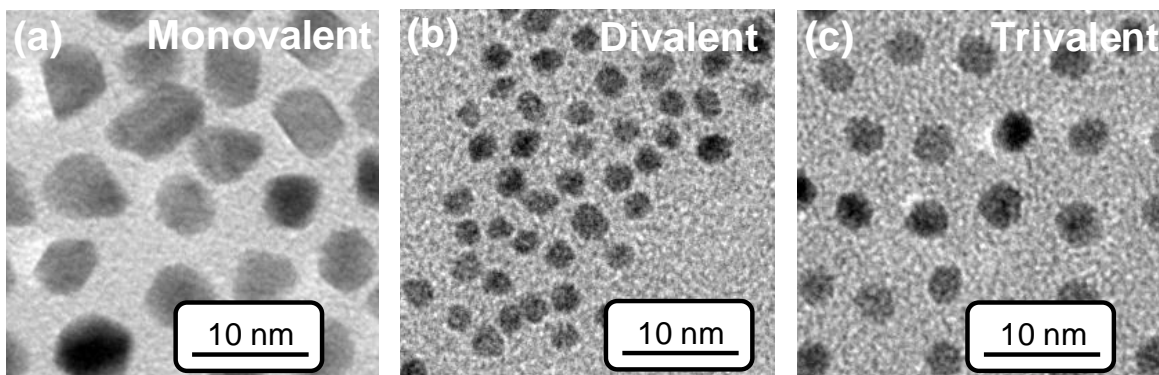
Figure 4.22: High magnification TEM images of platinum nanoparticles stabilized by amine ligands synthesized at 200 °C with (a) monovalent, (b) divalent, and (c) trivalent amine ligands.

It is obvious from the observed changes in color during the syntheses that the growth of the particles is faster in the presence of the monovalent amine ligands than in the presence of di- and trivalent amines. The TEM results indicate that the particles formed in the presence of monovalent ligands grow in an uncontrolled way into irregular shapes. In the presence of di- and trivalent ligands, the significantly slower growth process leads to spherically shaped particles. Black precipitates observed in the presence of monovalent ligands indicate partial aggregation of the particles, which are not observed in the case of nanoparticles stabilized by multivalent ligands. This could be explained by the different affinities of the mono- and multivalent ligands that the binding affinity of the multivalent ligands is higher than the corresponding monovalent ones (see Perumal et al.[116] and Section 4.1). In Section 4.1 and in ref. [142], it has been shown that because of the higher affinity of multivalent thiol ligands, gold nanoparticles stabilized by multivalent thiol ligands are more stable than particles stabilized by monovalent thiol ligands. The thiol ligands used in Section 4.1 have the same structures as the amine ligands used in this Section. Assuming a similar behavior for thiol and amine ligands, the lower stability of the nanoparticles stabilized by the monovalent ligands can be explained by the lower binding strength of the monovalent ligands compared to the di- and trivalent ones. As a consequence, the adsorption/desorption equilibrium of the surface-bound monovalent ligands is more shifted towards desorption than in case of the divalent and trivalent ligands. Thus, the monovalent ligands on platinum particles give an insufficient steric stabilization, and hence, partial aggregation of the nanoparticles results.

A minireview by Cheong et al. surveys the different ways for controlling the shape of platinum nanoparticles.[141] This includes changes in the stabilizing agents, changes in the metal precursors, variations of reductant concentrations, as well as changes in the temperature of the reaction mixtures.[19, 141, 144] Axet et al. controlled the shapes of platinum nanoparticles by using different types of amine ligands.[144] The preparation of platinum nanoparticles in the presence of long chain amine ligands results in particles of multipodal shape, which transforms into cubic, truncated cubic, or cuboctahedral shape upon heating.[144] Generally, the anisotropic growth of metallic nanoparticles is explained by a particular interaction of the ligands with selected facets of the crystal planes.[139] The nanoparticle growth is blocked, if the ligand binding is strong on the crystal plane and the growth is promoted, if the binding is weak on the crystal plane.[139]

Based on these considerations, for the present system it is assumed that the low binding affinity monovalent ligands promote the particles to grow in anisotropic direction and thus result in non-spherical shape particles. In contrast, the high binding affinity of di- and trivalent ligands leads to an isotropic growth, so that spherical particles result.

4.4.3.2. Platinum nanoparticles synthesized at stepwise increased temperatures between 160-200 °C

As shown in Section 4.3.3.1, the shapes of platinum nanoparticles are influenced by the multivalency of the amine ligands. The results in Section 4.3.3.1 are obtained from heating the reaction mixture directly to 200 °C. This procedure makes it difficult to derive the mechanism for the formation of the particles. This motivates us to study the influence of the multivalency of the ligands on the growth kinetics of platinum nanoparticles by stepwise increasing in temperature. For this purpose, systematic studies are carried out in the temperature range from 160 to 200 °C (see Figure 4.23). This might help to identify the minimum nucleation temperature and to study the influence of the ligand's multivalency at different temperatures.

A flow chart of the synthesis procedure using mono- and multivalent ligands for coating platinum nanoparticles is shown in Figure 4.23. The mono- or multivalent amine ligands and 1,2-hexadecanediol are added to $Pt(acac)_2$ in octyl ether and the mixture is heated to 160 °C. It is subsequently heated for 30 minutes followed by rising the temperature stepwise by 10 K every

30 minutes until 200 °C are reached. At this temperature the reaction mixture is kept for another 30 minutes (see Figure 4.23). The samples are collected at each temperature and they are directly investigated by TEM without any purification.
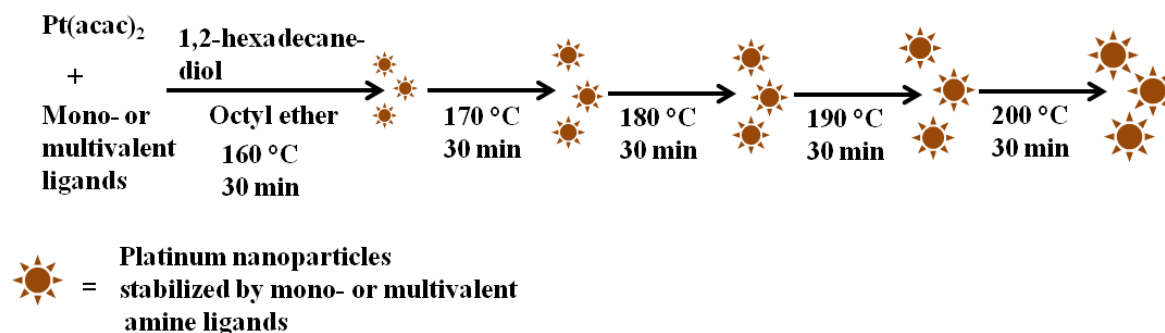

Figure 4.23: Flow chart explaining the experimental procedure for the formation of platinum nanoparticles in a stepwise procedure.

The start point of the nucleation process is estimated by the observation of a color change during the synthesis and also by TEM measurements. When the $Pt(acac)_2$ is heated with the monovalent amine ligands, the metal precursor starts to dissolve at 160 °C and at this stage the color of the reaction mixture changes from colorless to light yellow and then slowly to brown which shows that the nucleation of the nanoparticles starts at this temperature. However, even after heating for 30 minutes at 160 °C still unreacted $Pt(acac)_2$ is observed. When the reaction temperature is increased to 170 °C, all platinum precursors are dissolved and within 30 minutes the color changes from light brown to blackish brown. After that, the reaction mixture is subsequently heated to 180, 190, and 200 °C and maintained at each temperature for 30 minutes. If di- and trivalent amine ligands are used, the color of the reaction mixture remains yellow at 160 °C, even after 30 minutes of heating. However, the TEM images (see Figure 4.24) show that some particles are already present at 160 °C. Thus, it is assumed that at least some nucleation takes place at 160 °C. When the temperature is raised to 170 °C, the color changes to light brown within 5 minutes, but some unreacted platinum precursors are still found, which do not dissolve completely even after heating for 30 minutes. When the temperature is increased to 180 °C no unreacted platinum precursor can be observed after 5 minutes. At this stage, the color of the reaction mixture changes to blackish brown. Note, that the fact that no platinum precursor is

114

observed at 170 °C in case of the monovalent ligands and at 180 °C in case of the multivalent ligands does not mean that the formation of the particles is complete. Once the color of the reaction mixture changes to blackish brown it is difficult to notice if unreacted platinum precursors are still present. Additional experiments show that the formation of particles is not observed below 160 °C independent whether mono- or multivalent ligands are used. Further, at 160 °C it is observed that the color of the reaction mixture changes to brown only after heating for 8-10 hours. In addition, when the reaction mixtures are heated at 200 °C for more than 30 minutes, partial aggregation occurs.

The TEM images of platinum nanoparticles coated by mono-, di-, and trivalent amine ligands obtained from reactions in the temperature range between 160 and 200 °C are displayed in Figure 4.24. From these TEM images, it is clear that all particles obtained from this stepwise procedure have almost a spherical shape independent from the multivalency of the ligand and the reaction temperature. In contrast, if the particles are directly prepared to 200 °C only those particles prepared by di- or trivalent ligands are spherical, whereas the nanoparticles stabilized by monovalent amine ligands have a polyhedral shape (see Section 4.3.3.1). If the reaction temperature is stepwise increased, the particles stabilized by trivalent amine ligands have the largest diameter at all temperatures and the particles prepared by di- and monovalent amine ligands have within the experimental error the same diameter at all temperatures (see Table. 4.9). The size distributions obtained from the TEM measurements are also summarized in Table 4.9. The temperature-dependent synthesis shows a high reproducibility. Under identical conditions, particles with almost identical sizes within ±0.5 nm and a similar size distribution are received. The polydispersity decreases in all cases with increasing temperature (see Table 4.9). The particles stabilized by di- and trivalent ligands are highly polydisperse at 160 °C and 170 °C, but the polydispersity strongly decreases with increasing temperature, reaching about 14% and 17% at 200 °C, respectively. In the case of the nanoparticles stabilized by monovalent ligands, the initial polydispersity is at 160 °C significantly lower than in the presence of multivalent ligands, but the polydispersity of the particles stabilized by monovalent ligands decreases only slightly with increasing temperature.
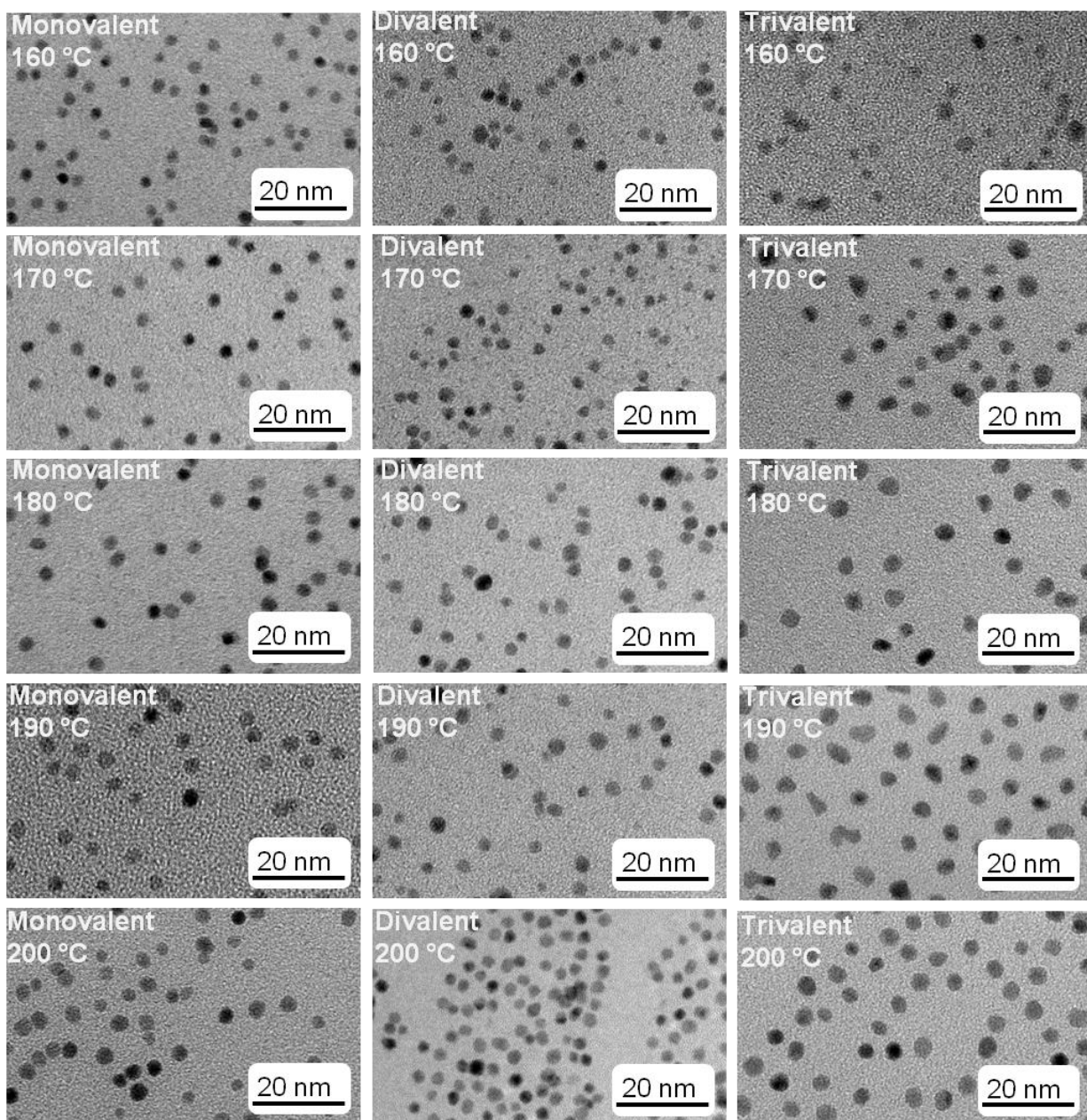
Figure 4.24: TEM images of platinum nanoparticles stabilized with mono-, di-, and trivalent amines synthesized at 160, 170, 180, 190, and 200 °C.

116

Table 4.9: Average diameter and size distribution obtained from the analysis of TEM images shown in Figure 4.23 of platinum nanoparticles using mono-, di-, and trivalent amine ligands prepared at 160, 170, 180, 190, and 200 °C. For a comparison, the data for the particles directly prepared at 200 °C (see Section 4.3.3.1) are also shown in the last line.

Temperature [°C]	Monovalent		Divalent		Trivalent	
	Diameter [nm]	Polydis-persity [%]	Diameter [nm]	Polydis-persity [%]	Diameter [nm]	Polydis-persity [%]
160	2.4±0.6	25	1.9±0.7	37	2.6±1.1	42
170	2.5±0.6	24	2.2±0.8	36	3.0±1.4	47
180	2.7±0.6	22	2.7±0.7	26	4.0±0.9	23
190	3.0±0.5	17	2.6±0.7	27	4.1±0.9	22
200	2.8±0.5	18	2.3±0.4	17	3.7±0.5	14
200 (one step)	5.7±0.6	11	2.6±0.5	19	3.6±0.4	11

Several authors reported that a variation of the reaction temperatures in the synthesis of platinum nanoparticles leads to particles with different morphologies.[138, 141] Ren et al. prepared different morphologies of platinum nanoparticles by decomposing the platinum precursor under a hydrogen pressure of 3 bar in the presence of oleylamine.[138] The authors assumed that an increase of the reaction temperature promotes the directional growth of platinum nanoparticles and leads to branched structures tripods, octapods, and multipods at 40, 70, and 100 °C respectively.[138] In contrast, in the present experiments the particles formed at all temperatures have a spherical shape, but the reaction temperature is much higher than in the case of Ren et al.[138] and no additional reductant is present.

From the observation of the color change during the particle synthesis and also from TEM measurements, the result obtained from the stepwise increasing the temperature process can be explained as follows: The nucleation processes for di- and trivalent ligands are slower and more

incomplete at low temperature (160 °C) than for the monovalent ligands. Likely, nucleation and growth are not well separated at this temperature, especially in case of the multivalent ligands so that highly polydisperse particles are formed. TEM measurements show that in presence of the monovalent ligands some further nucleation takes places at 170 °C. In contrast, the nucleation of multivalent ligand takes mainly place at 170 and 180 °C. As the polydispersity decreases with increasing temperature, it is assumed that the nucleation and growth process are more separated at higher temperature. As a consequence, the polydispersity decreases if the temperature is raised. These results reveal that the formation of nanoparticles occurs faster in the presence of monovalent ligands than in the presence of di- or trivalent ligands. Further, the experimental results indicate that in presence of monovalent ligands, the particle growth stops or a thermal equilibrium between growth and dissolution is reached at 180 °C, whereas in the presence of di- and trivalent ligands, this stage is reached at 190 °C.

A comparison of the results from the preparation process with a stepwise increase of the reaction temperature between 160 and 200 °C with the direct synthesis at 200 °C (see Section 4.3.3.1) yields the following differences: In presence of monovalent ligands, the particles prepared at 200 °C are larger than the particles prepared by a stepwise increased temperature. This can be explained by the observation that in the one-step heating process quick nucleation takes place and the growth process is completed within 3 minutes. Thus, a rather uncontrolled random growth of the particles takes place. In contrast (see Section 4.3.3.2), in the stepwise heating process a thermodynamically controlled, slow uniform and isotropic growth takes place at lower temperatures and therefore, spherical particles are received. In contrast, the particles prepared with di- and trivalent ligands are in the same size range independent of the reaction method. This is because the high binding affinity of the di- and trivalent ligands promotes a slow isotropic growth yielding spherical particles.

4.4.4. Influence of mono- and multivalent ligands on the formation of silver nanoparticles

In this Section the influence of amine functionalized mono- and multivalent ligands on the formation of the silver nanoparticles is discussed. For this investigation, the particles are prepared by a one-step synthesis at 120 °C as well as by a stepwise increase in temperature from 80 to 120 °C, similar as described in Sections 4.3.3.1 and 4.3.3.2 for platinum nanoparticles. For these syntheses $Ag(acac)_2$ is used as silver precursor and the influence of the ligand's multivalency on the formation, growth, and stability of the silver particles is studied by using TEM and UV-Vis measurements.

4.4.4.1. Silver nanoparticles synthesized at 120 °C

To $Ag(acac)_2$ in octyl ether, mono- or, di-, or trivalent amine ligands, and 1,2-hexadecandiol are added and heated to 120 °C. The reaction mixture is heated for 30 minutes at 120 °C and then cooled down to room temperature. After that, the nanoparticles are precipitated by the addition of ethanol. The particles are isolated by means of centrifugation at 1000 g for 10 min and subsequently, the supernatant is removed. The particles are washed three times with ethanol to remove amine ligands that are not particle-bound.

The influence of the ligand's multivalency on the formation of silver nanoparticles is analyzed from the observation of color changes during the synthesis, also by TEM and UV-Vis measurements. When $Ag(acac)_2$, the mono- or multivalent ligands, and 1,2-hexadecanediol in octyl ether are heated to 120 °C, the color of the mixture turns within 5 minutes from yellow to light brown and within 15 minutes to dark brown. The reaction mixture is subsequently heated for about 30 minutes for the completion of the reaction. The same color changes during in the reaction are observed for mono-, di-, and trivalent ligands. TEM images for the silver nanoparticles coated by mono- (a), di- (b), and trivalent (c) are shown in Fig. 4.25. Figure 4.25 (d) shows the plasmon resonance spectra of silver particles capped with mono-, di-, and trivalent amine ligands. The extinction maxima of the surface plasmon bands of the particles and the corresponding full width at half maximum (FWHM) are shown in Table 4.10. The size

distribution of the silver particles coated by monovalent ligands is shown in Figure 4.25 (a). It is broad and lies in the diameter range between ~1 nm to 25 nm. The extinction maxima of the plasmon resonance spectrum is observed at 416±0.5 nm and the FWHM value is 73.9±0.5 nm (see Table 4.10). A comparison of the extinction spectra in Figure 4.25 (d) reveals that the surface plasmon band of the silver nanoparticles stabilized by monovalent ligands is slightly broader than that of the nanoparticles stabilized by the di- and trivalent ligands. The particles coated by divalent ligands show a broad bimodal size distribution in TEM (see Figure 4.25 (b)) and the absorption maximum of the UV-Vis spectrum is observed at 415±0.7 nm, which is almost identical with the value for the monovalent ligands. The FWHM for the particles stabilized by the divalent ligand is 68.1±1.0 nm, which is slightly smaller than the value of the particles stabilized by monovalent ligands. Even though the size distributions of the particles stabilized by the trivalent ligands is broad with diameters between ~1 nm and 25 nm, the fraction of the small particles is much larger than that of the larger ones. The maximum of the plasmon resonance band for trivalent ligands is found at 411±0.7 nm, which is lower than the values obtained from particles stabilized with the mono-, and divalent ligands. The corresponding FWHM of the plasmon resonance is about 52.6±0.7 nm (see Table 4.10 and Figure 4.25 (d)). Thus, the plasmon band of the particles stabilized by the trivalent ligands is slightly narrower than that of those stabilized by mono- and divalent ligands.
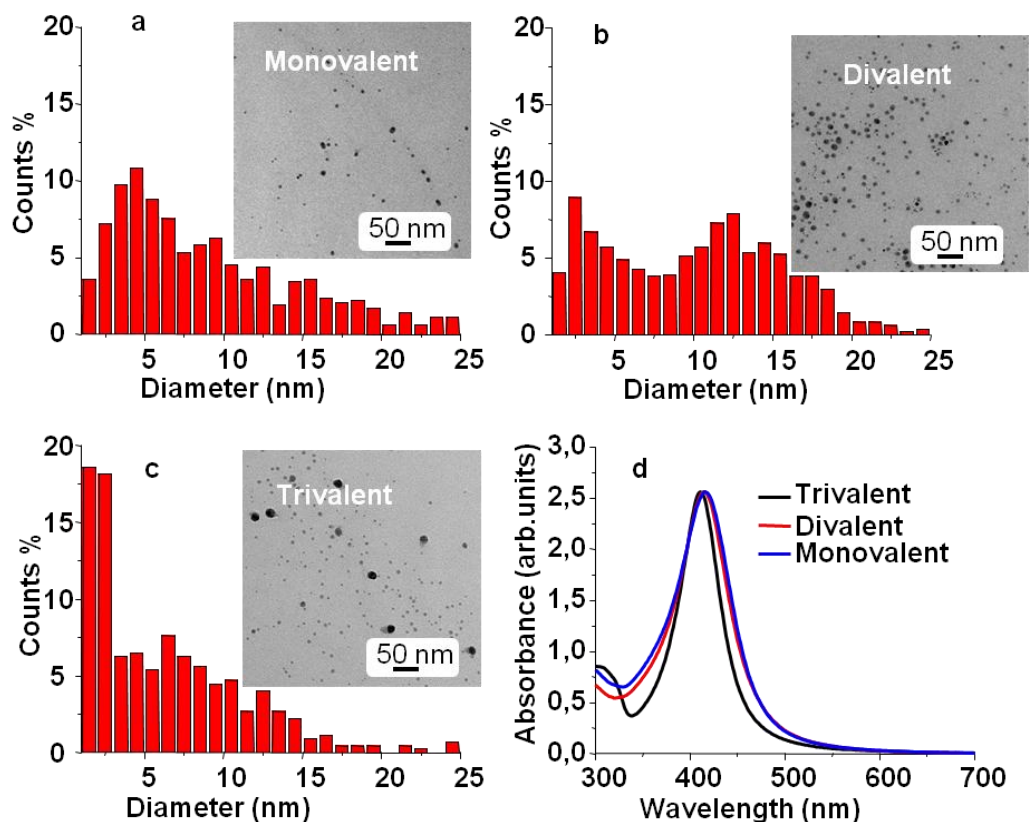
Figure 4.25: TEM images of amine-stabilized silver nanoparticles synthesized at 120 °C with (a) monovalent, (b) divalent, and (c) trivalent amine ligands as well as (d) plasmon resonance spectrum of silver particles stabilized by mono-, di-, and trivalent amine ligands.

Table 4.10: Extinction maxima of the surface plasmon bands and corresponding FWHM of silver nanoparticles stabilized by mono-, di-, and trivalent ligands. Each extinction maximum and the corresponding FWHM values are averaged data of two sets of experiments from different batches of particles.

Ligand	Monovalent	Divalent	Trivalent
Extinction Maximum [nm]	416±0.5	415±0.7	411±0.7
FWHM [nm]	73.9±0.5	68.1±1.0	52.6±0.7

The experimental results reveal that the particle size distribution and the UV-Vis spectra get narrower as the multivalency of the ligands increases. The narrower size distribution and the smaller average diameter of the particles stabilized by the trivalent ligands may be explained by the higher binding affinity of these ligands. If the ligands are tightly bound on the nanoparticle surface, further growth of the particles is impeded. However, for all ligands the extinction maxima are in the same range. The analysis of the TEM images reveals small differences between mono- and divalent ligands. Especially, the fraction of larger particles seems to be slightly larger in case of the divalent ligands. This is likely because of the slower nucleation process in presence of divalent ligands.

4.4.4.2. Silver nanoparticles synthesized by stepwise increase in temperatures between 80-120 °C

The silver particles are prepared by increasing the temperature in steps of 10 K, similar as described above for platinum nanoparticles (see Section 4.3.2.2). Systematic studies of the growth mechanism of silver nanoparticles are carried out in the temperature range between 80 and 120 °C (see Figure 4.27). In an additional experiment, it turned out that if the reaction mixture is heated above 120 °C aggregation occurs. This is similar to platinum particles, which aggregate above 200 °C. Thus, the temperature limits are chosen accordingly, so that aggregation is avoided.

The flow chart of the synthesis procedure of silver nanoparticles coated by mono- and multivalent ligands is shown in Figure 4.26. To Ag(acac)$_2$ in octyl ether, mono- or multivalent amine ligands and 1,2-hexadecanediol are added and heated to 80 °C. The mixture is heated for 30 minutes at this temperature followed by increasing the temperature stepwise by 10 K for 30 minutes until the temperature reaches 120 °C. At 120 °C the reaction mixture is also left for 30 minutes. The samples are collected at each temperature for the further analysis, in order to evaluate the effect of the temperature and multivalency of the ligands on the particle shape, size, and size distribution. This analysis makes use of TEM and UV-Vis spectroscopy.
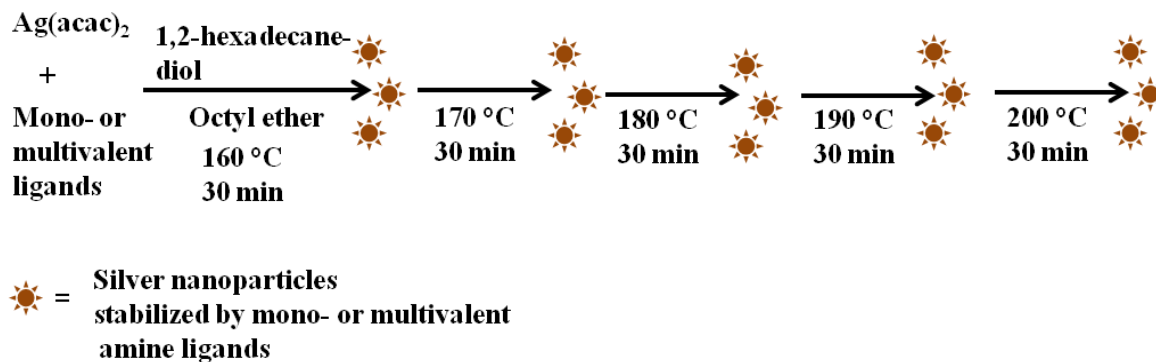
Figure 4.26: Flow chart explaining the experimental procedure for the formation of silver nanoparticles using mono- and multivalent ligands.

Initially, the reaction mixture is yellow and the color is independent from the ligand used. In the presence of monovalent ligands, the reaction mixture turns to light brown within 5 minutes when the reaction temperature reaches 80 °C. This shows that nucleation starts at this temperature. Further, the reaction mixture is heated for 30 minutes, where still unreacted silver precursors are observed. When the dispersion is heated to 90 °C, the unreacted brown powder of the silver precursors dissolves within 30 minutes. After this, the color of the reaction mixture stays dark brown between 100 °C and 120 °C. In the presence of multivalent ligands, no change in color is observed at 80 °C. However, some particles are observed in TEM images (see Figure 4.27) obtained from this temperature, which proves that nucleation starts already at this temperature. The color of the reaction mixture turns to light brown at 90 °C within 30 minutes, but at this temperature still a brown powder of the unreacted silver precursor is observed. It is observed that the silver precursor is dissolved at 100 °C and the color of the dispersion changes to dark brown. After this, the color of the reaction mixture stays dark brown at 110 °C and 120 °C. Note, that fact that no brown powder of Ag(acac)$_2$ is observed in the reaction mixture at 90 °C and above for monovalent ligand and at 100 °C and above for multivalent ligands does not imply that particle formation is complete at this stage of the reaction. Once the color of the reaction mixture changes to dark brown, it is difficult to notice if still unreacted silver precursors are present.

The size distribution of the nanoparticles stabilized by the monovalent ligands remains almost unchanged with increasing temperature, as shown in the TEM images in the left column of

Figure 4.27. The UV-Vis extinction spectra displayed in Figure 4.28 (a) and Table 4.11 show that the absorption maximum is slightly decreasing with increasing temperature and further, the FWHM is slightly decreasing when the temperature is increased (see Figure 4.28 (d)). In case of the divalent ligand, the TEM images (see middle column of Figure 4.27) of the samples prepared at 80 °C and 90 °C show similar particle sizes and the size distribution remains also practically constant. After heating the sample at 100 °C for 30 minutes, some more large particles (5-10 nm in diameter) are present in the sample than at lower temperatures and the size distribution appears more bimodal. At 110 °C the number of large particles slightly decreases and a higher number of small particles is observed at 120 °C (see middle column in Figure 4.27). However, the temperature-dependent changes in the wide size distribution are rather small.

The results of the UV-Vis measurements of silver particles formed in presence of the divalent ligands at different temperature are shown in Figure 4.28 (b). The extinction maxima of these spectra are displayed in Table 4.11. The maximum of the extinction spectra (see Table 4.11) and the corresponding FWHM (see Figure 4.28 (d)) of the particles stabilized by divalent ligands do not significantly change with increasing temperature. The TEM images of the silver nanoparticles stabilized by trivalent ligands obtained from a stepwise increase in reaction temperature are shown in the last column in Figure 4.28. At 80 °C, the particles are small and show a broad size distribution. At 90 °C the particles have a relatively small size distribution with a few larger particles. As the temperature is increased to 100 °C the average particle size is increased, where the diameter of the main fraction (particles of about 2-3 nm in diameter) is increased and a significant number of large particles are seen, reaching up to 18 nm. At 110 °C more large particles (>5-10 nm) are observed and the relative number of small particles is decreased. At 120 °C mostly small particles with a diameter of about 2-3 nm are present, but also some large particles of 5-20 nm are found. The UV-Vis extinction spectra of the silver particles stabilized by trivalent ligands obtained from the stepwise increased temperature are shown in Figure 4.28 (c). The maxima of the extinction spectra are summarized in Table 4.11 and the FWHM values are shown in Figure 4.28 (d). Both values, the maximum of the extinction spectrum and the FWHM value are decreasing with increasing temperature. This narrowing effect of the surface plasmon band is more obvious for particles which are stabilized by trivalent ligands than for those particles which are stabilized by di- and monovalent ligands (see Figure

124

4.28 c). This can be explained by the appearance of a higher number of small size particles (see TEM images in Figure 4.27). However, for silver particles no temperature-dependent spectral shift is observed in the UV-Vis spectra, as it was found earlier by Peng et al..[16] Peng et al. could show that if the diameter d of silver particles is stabilized by oleylamine ligands, then d decreases from d ≈ 20 nm to less than 12 nm, where the plasmon resonance is first blue-shifted but this turns into a strong red-shifts if the diameter decreased.[16] Accordingly, it is assumed that likely due to the occurrence of particles with sizes below and above this size limit in the present, fairly polydisperse samples a significant spectral shift in the UV-Vis extinction spectra is not observed.
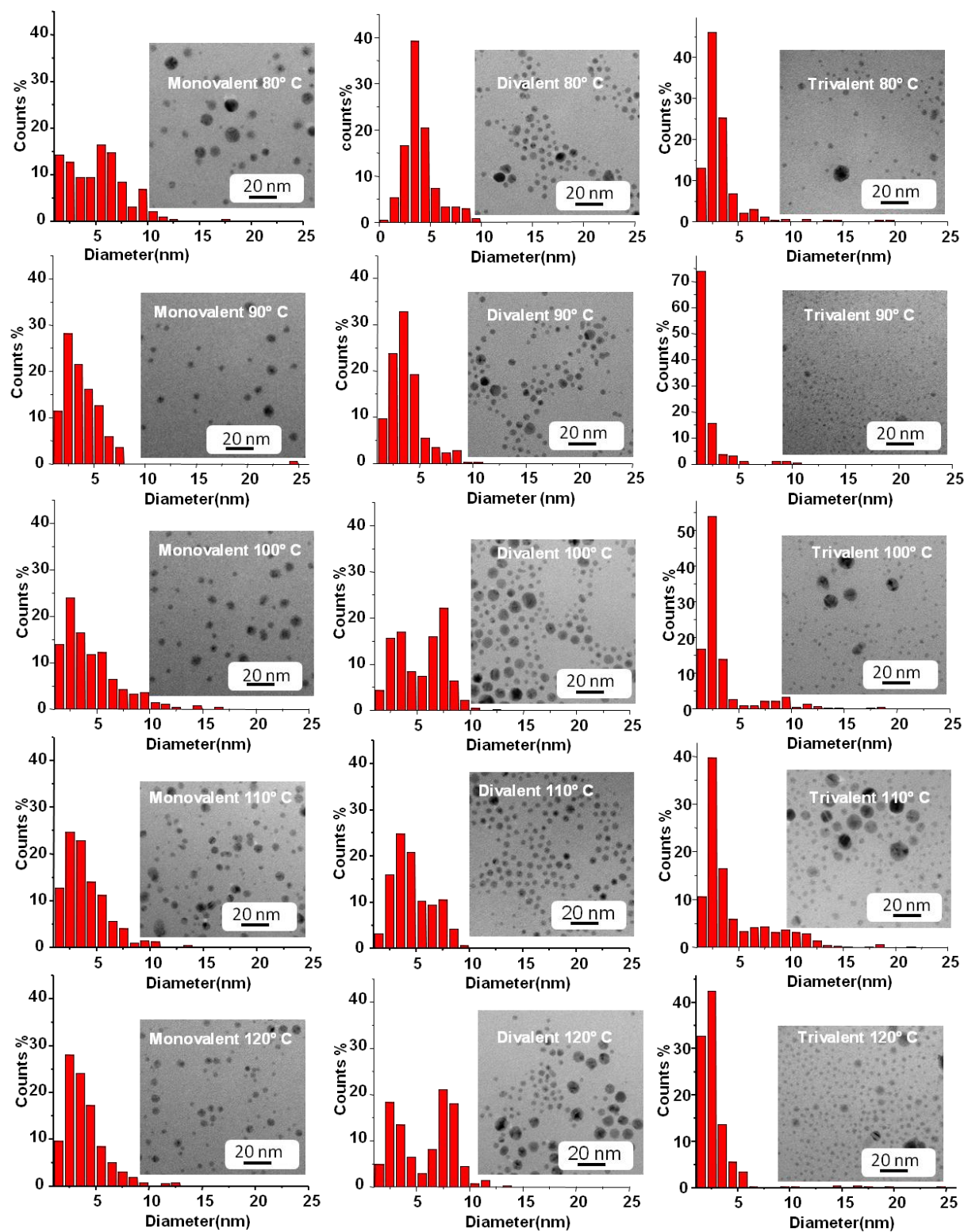
Figure 4.27: TEM images and histograms depicting the size distribution of silver nanoparticles stabilized with mono-, di-, and trivalent amine ligands prepared at 80, 90, 100, 110, and 120 °C.
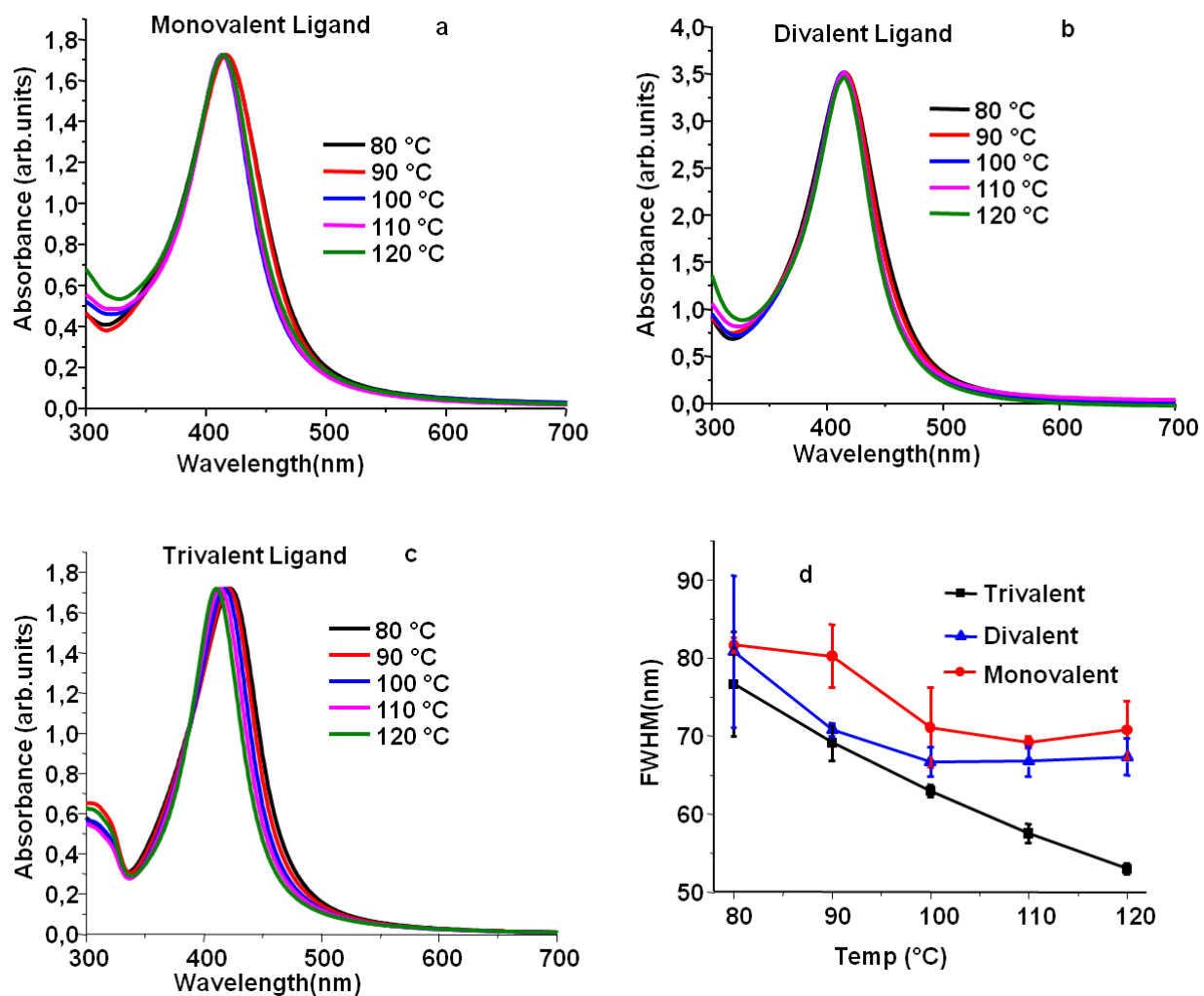
Figure 4.28: Plasmon resonance spectra of silver nanoparticles stabilized by (a) mono-, (b) di-, and (c) trivalent ligands in dichloromethane. The particles are prepared at 80, 90, 100, 110, and 120 °C, respectively (see text for details). Figure (d) shows the FWHM values of these nanoparticles as a function of the preparation temperature. The FWHM values are averaged data of two sets of spectra from different batches of particles.

Table 4.11: Maxima of the plasmon resonance spectra of silver nanoparticles stabilized by mono-, di-, and trivalent ligands in dichloromethane (see Figure 4.29 (a)-(c)). The particles are prepared at 80, 90, 100, 110, and 120 °C, respectively (see text for details). The extinction maximum values are averaged data of two sets of values from different batches of particles.

Temperature [°C]	Extinction maximum [nm]		
	Monovalent	Divalent	Trivalent
80	416±0.7	416±1.4	423±0.5
90	417±0.5	415±0.5	419±2.1
100	414±1.4	414±0.7	417±0.7
110	414±0.7	414±0.7	413±1.4
120	414±0.7	415±1.4	410±0.7

From the observed color changes during the particle synthesis, and the analysis of TEM images and UV-Vis measurements, the following reaction mechanism can be derived: In presence of monovalent ligands, nucleation takes place at 80 °C and the particle size distribution is rather broad. Since the visual observations suggest that the silver precursor dissolves completely only at 90 °C, it is assumed that further nucleation also takes place at 90 °C. After 30 minutes stirring at 90 °C the growth process is almost complete, above 90 °C according to the TEM data, neither the size distribution nor the average particles size changes significantly (see Figure 4.27). However, the width of the plasmon resonance band is slightly narrower at 100 °C than at 90 °C, which suggests that likely some minor Ostwald ripening or digestive ripening takes place.

Silver particles prepared directly at 120 °C in the presence of monovalent ligands have a significantly larger average size and a wider size distribution than those particles which are grown in the stepwise temperature increase process (9.6±6.7 nm instead of 3.9±2.0 nm see

Figures 4.25 (a) and 4.27, respectively). This can be explained by the much quicker nucleation and growth processes at 120 °C, as compared to the slower and more controlled processes at 80 °C and 90 °C, where the most of the particle formation takes place in the stepwise process.

From the observed color changes and from the TEM images obtained from the presence of divalent ligands it is assumed that in this case the nucleation process slightly starts at 80 °C but mainly takes place at 90 and 100 °C. Also, the average particle size is lager and size distribution is wider when the particles are prepared directly at 120 °C (10.2±5.6 nm instead of 5.8±2.6 nm see Figures 4.25 (b) and 4.27, respectively).

Similarly, also in the presence of trivalent ligands, the silver precursor is completely dissolved at 100 °C and it is assumed that the nucleation process starts at 80 °C, where it mainly takes place at 90 and 100 °C. The relative number of small particles increases when the temperature is increased from 80 to 90 °C, which supports the suggestion that significant nucleation, takes place at 90 °C. Also here, the average particle size is lager and size distribution is wider when the particles are directly prepared at 120 °C (6.8±5.5 nm instead of 2.8±2.2 nm see Figures 4.25 (c) and 4.27, respectively).

The overall observation shows that the nucleation process is slow in presence of multivalent ligands with a high binding affinity at lower temperature, as compared to the corresponding monovalent ligands. Independent from the ligand multivalency, the particles size and size distribution remains almost unchanged, when the temperature is increased. Thus, no significant Ostwald ripening or related processes as well as no aggregation take place, which indicates that mono, di-, and trivalent amine ligands are rather stably bound to silver particles. In contrast to this finding, Silvert et al. observed significant Ostwald ripening when they heated silver nanoparticles stabilized by ethylene glycol-polyvinylpyrolidone for longer times to 120 °C and in this way monodisperse particle are prepared.[143] However, the simply adsorbed ethylene glycol-polyvinylpyrolidone is less stable than the covalently bound amine ligands. Due to the high binding strength of amine ligands to silver already monovalent ligands are tightly bound, so that a further enhancement by multivalent ligands does not influence the properties of the particles upon a temperature increase. In addition to this ligand effect, it turned out that a stepwise growth process yields in all cases smaller particles with a narrower size distribution.

4.4.5. Conclusions

In this Section a novel and simple method is developed to prepare platinum and silver nanoparticles, which are stabilized by mono- and multivalent amine ligands using $Pt(acac)_2$ and $Ag(acac)_2$ as precursors, respectively. The platinum and silver particles stabilized by mono- and multivalent ligands are prepared by a one-step process as well as a process, where the reaction temperature is stepwise increased. The influence of the multivalency of the ligands on the formation of nanoparticles is systematically investigated by using TEM and UV-Vis spectroscopy.

The platinum particles prepared in a one-step process at 200 °C show a non-spherical shape in the presence of monovalent amine ligands and an almost spherical shape in presence of di- and trivalent ligands. This is explained by assuming that the binding affinity of the amine ligands controls the particle growth, where monovalent ligands lead to fast, uncontrolled anisotropic growth, whereas the presence of strongly-binding multivalent ligands results in an isotropic growth. In contrast, platinum particles prepared by stepwise increasing the temperature between 120 and 200 °C have a spherical shape, regardless of the valency of the ligands. This is because the slow nucleation process promotes the particles to grow isotropically, which yields spherically shaped particles.

The results obtained from the studies on silver particles, which are prepared in a one-step heating process at 120 °C and by stepwise increasing the reaction temperature between 80 and 120 °C show that the multivalency of the ligands clearly influences the nucleation process. In both cases, the nucleation process is quicker in the presence of monovalent ligands than in the presence of di- and trivalent ligands. Regarding the stepwise growth process, it turns out that, if monovalent ligands are used, nucleation and growth mainly takes place at 80 °C and is practically completed at 90 °C. In contrast, applying di- and trivalent ligands shifts the main nucleation and growth processes to temperatures of 90-100 °C. However, the multivalency of the ligands does not influence the shape of the particles, as it is observed for platinum nanoparticles. This can be explained by assuming that all applied amine ligands form a tight covalent bond to silver which

reduces the particle growth, so that all particles can grow isotropically into a more or less spherical shape. There is also no evidence for the preferred binding of ligands on specific crystals facets. However, the size distributions of silver particles prepared in the presence of mono-, di-, and trivalent ligands in a one-step heating process are wider than those of the particles which are prepared by the stepwise process. Further, the average size of the particles is larger for the particle from the one-step process than for those from a stepwise process. This can be explained by faster nucleation and growth of silver particles in the one-step process at higher temperature, as compared to the stepwise process.

5. Conclusions

The aim of this thesis was to tailor the properties of metallic nanoparticles, which are of interest for possible application. For this it is essential to understand the interactions between the ligands used as stabilizers and the particle surfaces. Specifically, different physico-chemical techniques are explored to investigate the interactions between ligands with noble metal nanoparticles, where the valency of the ligands is systematically varied. The interactions between thiol and amine functionalized mono- and multivalent ligands with gold, silver, and platinum nanoparticles have been studied using fluorescence spectroscopy, high magnification TEM, and UV-Vis spectroscopy.

The results of this work are summarized as follows: In Section 4.1, a recently developed approach to quantify the ligand exchange kinetics on gold nanoparticles by fluorescence spectroscopy is extended and applied for investigations of multivalent interactions. Gold nanoparticles with three different average diameters (2.2 ± 0.4 nm (Au-small), 3.2 ± 0.7 nm (Au-medium), and 4.4 ± 0.9 nm (Au-large) are synthesized using wet colloidal chemistry. Mono-, di-, and trivalent flexible alkyl thiol ligands are synthesized using reported procedures. The gold nanoparticles are initially prepared using a fluorescent pyrene which is bound by a monovalent thiol group on the surface. This pyrene thiol ligands are exchanged by the mono-, di-, and trivalent alkyl thiol ligands and the binding kinetics of the thiol ligands is investigated by time-resolved fluorescence spectroscopy. The influences of the ligand's multivalency and the particle size regarding the exchange kinetics are elucidated in detail by determining the ligand exchange reaction rate constants. For this purpose, various models have been used in order to fit the experimental results. There served to explain the experimental results. All results from kinetics studies are well fitted by a bi-exponential function as well as by a second order Langmuir diffusion model. The use of the bi-exponential model is motivated by the assumption that different sites of the nanoparticles have different reactivities, which takes in small gold nanoparticles edge-, corner-, face-, and defect-sites into account. The second order Langmuir diffusion model describes a diffusion-limited ligand exchange. A significant enhancement of the reaction rate is observed for tri- and divalent ligands compared to monovalent ones. This is

explained by a significant multivalency effect. In contrast, the exchange rates of the trivalent ligands are similar or even lower than those of the divalent ones, which is due to the steric hindrance of the bulky ligands. In addition, it could be shown that the ligand exchange rate constants increase with particle size.

The experimental results can be explained by a mechanism, where the exchange of one pyrene ligand causes a weakening of the gold-thiol bond of the pyrene ligands in its vicinity. It is observed that such a cooperative mechanism is more effective for larger particles and promotes the binding of multivalent thiol ligands. Such a mechanism is in agreement with a bi-exponential fit model of the kinetics, since this model takes different reactivity of different particles sites into account. In contrast, the diffusion-limited process is ruled out since it does neither explain the multivalency effect nor the particle size dependence of the ligand exchange process.

In Section 4.2, pyrene thiol ligands on gold nanoparticles with 2.2±0.4 nm (Au-small), 3.2±0.7 nm (Au-medium), and 4.4±0.9 nm (Au-large) diameter are exchanged by rigid mono- and divalent aromatic thiols. In contrast to the result discussed in Section 4.1, the particles aggregate immediately after the addition of the aromatic rigid thiol ligands. This is because the aromatic rigid thiol does not provide steric stabilization as the pyrene thiol does. Thus, a systematic study of the exchange kinetics of pyrene thiol ligands against aromatic rigid thiols on gold nanoparticles was not feasible. This reveals that mono- or multivalent flexible alkyl thiol ligands are effective stabilizers for gold nanoparticles in contrast to mono- or divalent rigid aromatic thiol ligands.

In Section 4.3, the ligand exchange kinetics of mono-, di-, and trivalent alkyl thiol ligands with pyrene thiols on 4.6±2.0 nm silver nanoparticles is discussed in greater detail. These kinetics results are compared to those results gathered for the ligand exchange reaction of mono-, di-, and trivalent alkyl thiol ligands with pyrene thiols on gold nanoparticles of similar size (4.4±0.9 nm in diameter). Significant aggregation is in case of the silver nanoparticles already observed in an initial phase of ligand exchange reaction. This could be due to insufficient steric stabilization of the nanoparticles by the flexible alkyl thiol ligands. These results reveal that a systematic study of the kinetics is also not feasible on gold and silver nanoparticles with a diameter of 4 nm or larger. However, the initial part of the kinetics curves reveals that the exchange rates of

134

multivalent ligands are higher than those of the monovalent one. The exchange rates of monovalent alkyl thiol ligands against pyrene thiol on silver nanoparticles are initially higher. However, at a later stage the exchange rates on gold nanoparticles appear to be higher than on silver nanoparticles. This change in the exchange rates can be explained by the differences in degrees of aggregation of gold and silver nanoparticles. In general gold is soft in nature than silver and thus gold shows a higher affinity towards thiol ligands than silver. Due to the lower affinity of thiol ligands to silver particles, aggregation of the silver particles during ligand exchange reaction is quicker than the aggregation of the gold nanoparticles.

In Section 4.4, a novel and simple method is developed for the synthesis of platinum and silver nanoparticles stabilized by mono- or multivalent alkyl amine ligands by using $Pt(acac)_2$ and $Ag(acac)_2$ as precursors, respectively. To investigate the influence of mono- and multivalent ligands on the formation of platinum and silver nanoparticles, particles are prepared by a one-step process as well as by a process where the temperature is stepwise increased. The influence of the ligand's multivalency on the formation of the particles is investigated by TEM and UV-Vis measurements.

The platinum particles prepared by a one-step process at 200 °C in presence of monovalent ligands grow into a non-spherical shape whereas the use of di- and trivalent ligands leads to the formation of spherical particles. This observation is explained by the different affinities of the ligands binding to the nanoparticles. The multivalent ligands with higher affinities lower the growth of particles so that they grow isotropically, whereas the monovalent ligands with a lower affinity to the particles cause an anisotropic particle growth. In contrast, platinum particles prepared by stepwise increasing the temperature between 120 and 200 °C have a spherical shape, regardless of whether mono- and multivalent ligands are used. Here, the slow growth process promotes an isotropic growth of the particles.

The results gathered for the silver particles prepared by a one-step heating process and by a stepwise temperature controlled process show that the ligand's multivalency influences the nucleation process. In both cases, it is observed that the nucleation process is slower in the presence of multivalent ligands than in the presence of monovalent ligands. In the stepwise process in the presence of monovalent ligands, nucleation and growth mainly take place at 80 °C

and are practically completed at 90 °C. In contrast, in the presence of di- and trivalent ligands the main nucleation and growth processes takes place between 90 and 100 °C. However, the multivalency of the ligands does not influence the shape of the particles, as it is observed for platinum particles. This can be explained by assuming that the amine ligands form a tight covalent bond to silver which lowers the particle growth rate, so that particles grow isotropically into a more or less spherical shape. Further, there is no evidence for a preferred binding of the ligands on specific crystals facets. However, the size distributions of silver particles prepared in the presence of mono- and multivalent ligands by a one-step heating process are wider than those of the particles prepared by the stepwise process, in which the temperature is increased. Moreover, the average size of the particles from the one-step process is larger than that of the particles prepared by a stepwise process. This can be explained by the faster nucleation and growth of the silver particles in the one-step process at higher temperature compared to the stepwise process at lower temperatures.

The obtained results show two important aspects of multivalent ligands on the functionalization and formation of noble metal nanoparticles:

1) Ligand exchange reactions of multivalent ligands are faster than those of monovalent ligands. The effectiveness of this multivalency effect can be reduced if the surface curvature of the particles is high and steric hindrance becomes a limiting factor.

2) The presence of multivalent ligands during particle formation can reduce the nucleation rate, decelerate the particle growth, and promote a more isotropic growth of the nanoparticles.

Both results can be explained by the higher affinity of multivalent ligands to the metallic nanoparticle surface compared to monovalent ligands.

List of figures

List of schemes

List of tables

References

[1]   D. N. Reinhoudt, M. Crego-Calama, *Science* **2002**, *295*, 2403.

[2]   M. Mammen, S.-K. Choi, G. M. Whitesides, *Angew. Chem. Int. Ed.* **1998**, *37*, 2754.

[3]   R. S. Kane, *Langmuir* **2010**, *26*, 8636.

[4]   L. L. Kiessling, J. E. Gestwicki, L. E. Strong, *Curr. Opin. Chem. Biol.* **2000**, *4*, 696.

[5]   A. Perl, A. G. Casado, D. Thompson, H. H. Dam, P. Jonkheijm, D. N. Reinhoudt, J. Huskens, *Nature Chem.* **2011**, *3*, 317.

[6]   J. E. Gestwicki, C. W. Cairo, L. E. Strong, K. A. Oetjen, L. L. Kiessling, *J. Am. Chem. Soc.* **2002**, *124*, 14922.

[7]   W. B. Turnbull, *Nature Chem.* **2011**, *3*, 267.

[8]   R. R. Kolega, J. B. Schlenoff, *Langmuir* **1998**, *14*, 5469.

[9]   F. Manea, C. Bindoli, S. Fallarini, G. Lombardi, L. Polito, L. Lay, R. Bonomi, F. Mancin, P. Scrimin, *Adv. Mater.* **2008**, *20*, 4348.

[10]   R. J. Pieters, *Org. Biomol. Chem.* **2009**, *7*, 2013.

[11]   R. Nagarajan, A. T. Hatton, *Nanoparticles: Synthesis, Stabilization, Passivation, and Functionalization.* American Chemical Society, **2008**.

[12]   C. N. R. Rao, G. U. Kulkarni, P. J. Thomas, P. P. Edwards, *Chem. Soc. Rev.* **2000**, *29*, 27.

[13]   G. H. Woehrle, J. E. Hutchison, *Inorg. Chem.* **2005**, *44*, 6149.

[14]   L. M. Liz-Marzán, *Mater. Today* **2004**, *7*, 26.

[15]   G. V. Hartland, *Annu. Rev. Phys. Chem.* **2006**, *57*, 403.

[16]   S. Peng, J. M. Mcmahon, G. C. Schatz, S. K. Gray, Y. Sun, *PNAS* **2010**, *107*, 14530.

[17]   Q. Zhang, J. Ge, T. Pham, J. Goebl, Y. Hu, Z. Lu, Y. Yin, *Angew. Chem. Int. Ed. Engl.* **2009**, *48*, 3516.

[18]   J. W. Yoo, S.-M. Lee, H.-T. Kim, M. A. El-Sayed, *Bull. Korean Chem. Soc.* **2004**, *25*, 395.

[19]   J. M. Petroski, Z. L. Wang, T. C. Green, M. A. El-Sayed, *J. Phys. Chem. B* **1998**, *102*, 3316.

[20]   A. Caragheorgheopol, V. Chechik, *Phys. Chem. Chem. Phys.* **2008**, *10*, 5029.

[21] C. S. Weisbecker, M. V. Merritt, G. M. Whitesides, *Langmuir* **1996**, *12*, 3763.

[22] S. S. Agasti, C.-C. You, P. Arumugam, V. M. Rotello, *J. Mater. Chem.* **2008**, *18*, 70.

[23] K. Wojczykowski, D. Meißner, P. Jutzi, I. Ennen, A. Hütten, M. Fricke, D. Volkmer, *Chem. Commun. (Camb)* **2006**, 3693.

[24] R. Guo, Y. Song, G. Wang, R. W. Murray, *J. Am. Chem. Soc.* **2005**, *127*, 2752.

[25] M. J. Hostetler, A. C. Templeton, R. W. Murray, *Langmuir* **1999**, *15*, 3782.

[26] P. Ionita, A. Caragheorgheopol, B. C. Gilbert, V. Chechik, *Langmuir* **2004**, *20*, 11536.

[27] M. Montalti, L. Prodi, N. Zaccheroni, R. Baxter, G. Teobaldi, F. Zerbetto, *Langmuir* **2003**, *19*, 5172.

[28] S.-K. Choi, *Synthetic multivalent molecules*, John Wiley & Sons, **2004**.

[29] S. J. Danishefsky, J. R. Allen, *Angew. Chem. Int. Ed.* **2000**, *39*, 836.

[30] I. J. Krauss, J. G. Joyce, A. C. Finnefrock, H. C. Song, V. Y. Dudkin, X. Geng, J. D. Warren, M. Chastain, J. W. Shiver, S. J. Danishefsky, *J. Am. Chem. Soc.* **2007**, *129*, 11042.

[31] Y. Liu, J. R. Carroll, L. A. Holt, J. McMahon, B. Giomarelli, G. Ghirlanda, *Biopolymers* **2009**, *92*, 194.

[32] J.-S. Park, A. N. Vo, D. Barriet, Y.-S. Shon, T. R. Lee, *Langmuir* **2005**, *21*, 2902.

[33] M. Faraday, *Philos. Trans. R. Soc. London* **1857**, *147*, 145.

[34] G. B. Sergeev, *Nanochemistry*, Elsevier, **2006**.

[35] G. Schmid, *Nanoparticles from theory to application*, Wiley-VCH, **2004**.

[36] Y. Yang, X. Gong, H. Zeng, L. Zhang, X. Zhang, C. Zou, S. Huang, *J. Phys. Chem. C* **2010**, *114*, 256.

[37] D.-K. Lee, S.-I. Park, J. K. Lee, N.-M. Hwang, *Acta. Materialia* **2007**, *55*, 5281.

[38] C. Burda, X. Chen, R. Narayanan, M. A. EI-Sayed, *Chem. Rev.* **2005**, *105*, 1025.

[39] J. A. Creighton, D. G. Eadon, *J. Chem. Soc.-Faraday Trans.* **1991**, *87*, 3881.

[40] L. M. Liz-Marzán, *Langmuir* **2006**, *22*, 32.

[41] P. Mulvaney, *Langmuir* **1996**, *12*, 788.

[42] U. Kreibig, C. V. Fragstein, *Z. Physik* **1969**, *224*, 307.

[43] M. M. Alvarez, J. T. Khoury, T. G. Schaaff, M. N. Shafigullin, I. Vezmar, R. L. Whetten, *J. Phys. Chem. B* **1997**, *101*, 3706.

[44] R. A. Zsigmondy, *Nobel Lecture* **1926**, 45.

[45] J. Turkevich, P. C. Stevenson, J. Hillier, *Discuss. Faraday Soc.* **1951**, *11*, 55.

[46] G. Frens, *Kolloid-Z. u. Z. Polymere* **1972**, *250*, 736

[47] M. Brust, M. Walker, D. Bethell, D. J. Schiffrin, R. Whyman, *J. Chem. Soc., Chem. Commun.* **1994**, 801.

[48] O. Masala, R. Seshadri, *Annu. Rev. Mater. Res.* **2004**, *34*, 41.

[49] R. Sardar, A. M. Funston, P. Mulvaney, R. W. Murray, *Langmuir* **2009**, *25*, 13840.

[50] N. Zheng, J. Fan, G. D. Stucky, *J. Am. Chem. Soc.* **2006**, *128*, 6550.

[51] B. L. V. Prasad, S. I. Stoeva, C. M. Sorensen, K. J. Klabunde, *Chem. Mater.* **2003**, *15*, 935.

[52] W. Mody, R. Siwale, S. A., H. R. Mody, *J. Pharm. Bioall. Sci.* **2010**, *2*, 282.

[53] J. Xu, X. Han, H. Liu, Y. Hu, *Colloids and Surfaces A: Physicochem. Eng. Aspects* **2006**, *273*, 179.

[54] S. Nie, S. R. Emory, *Science* **1997**, *275*, 1102.

[55] J. Thiel, L. Pakstis, S. Buzby, M. Raffi, C. Ni, D. J. Pochan, S. I. Shah, *Small* **2007**, *3*, 799.

[56] A. Šileikaitė, I. Prosyčevas, J. Puišo, A. Juraitis, A. Guobienė, *Mater. Sci.* **2006**, *12*, 287.

[57] S. Y. Kang, K. Kim, *Langmuir* **1998**, *14*, 226.

[58] R. Shankar, B. B. Wu, T. P. Bigioni, *J. Phys. Chem. C* **2010**, *114*, 15916.

[59] E. G. Castro, R. V. Salvatierra, W. H. Schreiner, M. M. Oliveira, A. J. G. Zarbin, *Chem. Mater.* **2010**, *22*, 360.

[60] J. Chen, B. Lim, E. P. Lee, Y. Xia, *Nano Today* **2009**, *4*, 81.

[61] S. E. Eklund, D. E. Cliffel, *Langmuir* **2004**, *20*, 6012.

[62] M. Subhramannia, K. Ramaiyan, V. K. Pillai, *Langmuir* **2008**, *24*, 3576.

[63] S. F. Li, Y. H. Guo, W. W. Sun, D. L. Sun, X. B. Yu, *J. Phys. Chem. C* **2010**, *114*, 21885.

[64] J. Yang, T. C. Deivaraj, H.-P. Too, J. Y. Lee, *J. Phys. Chem. B* **2004**, *108*, 2181.

[65] T. S. Ahmadi, Z. L. Wang, T. C. Green, A. Henglein, M. A. El-sayd, *Science* **1996**, *272*, 1924.

[66] S. Coffey, *Rodd's Chemistry of Carbon Compounds*, Elsevier, **1965**.

[67] B. C. Cossar, J. O. Fournier, D. L. Fields, D. D. Reynolds, *J. O. C.* **1962**, *27*, 93.

[68]   K. Wojczkowski, P. Jutzi, *Synlett* **2006**, *1*, 39.

[69]   D. R. Strobach, *Carbohyd. Res.* **1971**, *17*, 457.

[70]   R. R. Frey, C. K. Wada, R. B. Garland, M. L. Curtin, M. R. Michaelides, J. Li, L. J. Pease, K. B. Glaser, P. A. Marcotte, J. J. Bouska, S. S. Murphy, S. K. Davidsen, *Bioorg & Medi. Chem. Let.* **2002**, *12*, 3443.

[71]   O. Mitsunobu, *Synthesis* **1981**, *1*, 1.

[72]   P. Uznański, J. Kurjata, E. Bryszewska, *Mater. Sci-Poland.* **2009**, *27*, 659.

[73]   A. Hofmann, *Ph.D Thesis* Freie Universität Berlin (Berlin), **2010**.

[74]   R. N. Shreve, D. R. Burtsfield, *Ind. Eng. Chem.* **1941**, *33*, 218.

[75]   U. Ragnarsson, L. Grehn, *Acc. Chem. Res.* **1991**, *24*, 285.

[76]   A. Roychowdhury, H. Illangkoon, C. L. Hendrickson, S. A. Benner, *Org. Lett.* **2004**, *6*, 489.

[77]   J. Skarzewski, E. Daniluk, *Monatsh. Chem.* **1983**, *114*, 1071.

[78]   D. Fenske, P. Sonström, J. Stöver, X. Wang, H. Borchert, J. Parisi, J. Kolny-Olesiak, M. Bäumer, K. Al-Shamery, *Chem. Cat. Chem.* **2010**, *2*, 198.

[79]   H. Hiramatsu, F. E. Osterloh, *Chem. Mater.* **2004**, *16*, 2509.

[80]   C. N. Kostelansky, J. J. Pietron, M.-S. Chen, W. J. Dessick, K. E. Swider-Lyons, D. E. Ramaker, R. M. Stroud, C. A. Klug, B. S. Zelakiewicz, T. L. Schull, *J. Phys. Chem. B* **2006**, *110*, 21487.

[81]   D. V. Leff, L. Brandt, J. R. Heath, *Langmuir* **1996**, *12*, 4723.

[82]   S. K. Pahari, T. Adschiri, A. B. Panda, *J. Mater. Chem.* **2011**, *21*, 10377.

[83]   R. L. Donkers, Y. Song, R. W. Murray, *Langmuir* **2004**, *20*, 4703.

[84]   R. Hong, J. M. Fernández, H. Nakade, R. Arvizo, T. Emrick, V. M. Rotello, *Chem. Commun. (Camb)* **2006**, 2347.

[85]   A. Kassam, G. Bremner, B. Clark, G. Ulibarri, R. B. Lennox, *J. Am. Chem. Soc.* **2006**, *128*, 3476.

[86]   J. Petroski, M. H. Chou, C. Creutz, *Inorg. Chem.* **2004**, *43*, 1597.

[87]   Y. Shichibu, Y. Negishi, T. Tsukuda, T. Teranishi, *J. Am. Chem. Soc.* **2005**, *127*, 13464.

[88]   M. G. Warner, S. M. Reed, J. E. Hutchison, *Chem. Mater.* **2000**, *12*, 3316.

[89]   G. H. Woehrle, L. O. Brown, J. E. Hutchison, *J. Am. Chem. Soc.* **2005**, *127*, 2172.

[90] G. H. Woehrle, M. G. Warner, J. E. Hutchison, *J. Phys. Chem. B* **2002**, *106*, 9979.

[91] S. Rucareanu, V. J. Gandubert, R. B. Lennox, *Chem. Mater.* **2006**, *18*, 4674.

[92] L. Polavarapu, Q. H. Xu, *Nanotechnology* **2009**, *20*, 185606.

[93] A. J. Kell, R. L. Donkers, M. S. Workentin, *Langmuir* **2005**, *21*, 735.

[94] W. Wan, J. T. W. Yeow, *Nanotechnology* **2009**, *20*, 325702.

[95] P. Ionita, A. Caragheorgheopol, *J. Am. Chem. Soc.* **2002**, *124*, 9048.

[96] P. Atkins, J. de Paula, *Atkin's Physical Chemistry*, W. H. Freeman and company, **2006**.

[97] K. A. Connors, *Chemical Kinetics-The study of reaction rates in solution*, VCH., **1990**.

[98] J. D. Badjic´, S. J. Cantrill, J. F. Stoddart, *J. Am. Chem. Soc.* **2004**, *126*, 2288.

[99] Y. Song, R. W. Murray, *J. Am. Chem. Soc.* **2002**, *124*, 7096.

[100] E. Arranz-Plaza, A. S. Tracy, A. Siriwardena, J. M. Pierce, G.-J. Boons, *J. Am. Chem. Soc.* **2002**, *124*, 13035.

[101] B. M. Tissue, in *http://www.files.chem.vt.edu/chem-ed/spec/beerslaw.html*, **2000**.

[102] J. R. Lakowicz, *Principles of fluorescence spectroscopy*, Springer, **2006**.

[103] I. D. Johnson, M. W. Davidson,
http://www.olympusmicro.com/primer/java/jablonski/jabintro/index.html, **2011**.

[104] J. B. Birks, L. G. Christophorou, *Spectrochimlca Acta.* **1963**, *19*, 401.

[105] I. Yamazaki, N. Tamai, T. Yamazaki, *J. Phys. Chem.* **1987**, *91*, 3572.

[106] S. V. Camyshan, N. P. Gritsan, V. V. Korolev, N. M. Bazhin, *Chem. Phys.* **1990**, *142*, 59

[107] C. S. Parmenter, J. D. Rau, *J. Chem. Phys.* **1969**, *51*, 2242.

[108] M. Inokuti, F. Hirayama, *J. Chem. Phys.* **1965**, *43*, 1978.

[109] N. Nerambourg, M. H. V. Werts, M. Charlot, M. Blanchard-Desce, *Langmuir* **2007**, *23*, 5563.

[110] B. I. Ipe, K. G. Thomas, S. Barazzouk, S. Hotchandani, P. V. Kamat, *J. Phys. Chem. B* **2002**, *106*, 18.

[111] N. Yao, Z. L. Wang, *Hanbook of microscopy for nanotechnology*, Kluwer academic publishers, **2005**.

[112] R. F. Egerton, *Physical principles of electron microscopy*, Springer, **2005**.

[113] M. Matoba, T. Kajimoto, K. Nishide, M. Node, *Chem. Pharm. Bull.* **2006**, *54*, 141.

[114] B. Weibull, M. Matell, *Acta Chem. Scand.* **1962**, *4*, 1062.

[115]   S. C. Hernandez, in *NNIN REU* **2006**, 66.

[116]   S. Perumal, A. Hofmann, N. Scholz, E. Rühl, C. Graf, *Langmuir* **2011**, *27*, 4456.

[117]   G. Battistini, P. G. Cozzi, J.-P. Jalkanen, M. Montalti, L. Prodi, N. Zaccheroni, F. Zerbetto, *ACS Nano* **2008**, *2*, 77.

[118]   K. W. Kittredge, M. A. Fox, J. K. Whitesell, *J. Phys. Chem. B* **2001**, *105*, 10594.

[119]   J. J. Hickman, D. Ofer, C. Zou, M. S. Wrighton, P. E. Laibinis, G. M. Whitsides, *J. Am. Chem. Soc.* **1991**, *113*, 1128.

[120]   J. B. Schlenoff, M. Li, H. Ly, *J. Am. Chem. Soc.* **1995**, *117*, 12528.

[121]   C. D. Bain, J. Evall, G. M. Whitesides, *J. Am. Chem. Soc.* **1989**, *111*, 7155.

[122]   Y. Song, T. Huang, R. W. Murray, *J. Am. Chem. Soc.* **2003**, *125*, 11694.

[123]   R. E. Benfield, *J. Chem. Soc.-Faraday Trans.* **1992**, *88*, 1107.

[124]   O. Dannenberger, M. Buck, M. Grunze, *J. Phys. Chem. B.* **1999**, *103*, 2202.

[125]   R. Georgiadis, K. P. Peterlinz, A. W. Peterson, *J. Am. Chem. Soc.* **2000**, *122*, 3166.

[126]   K. A. Peterlinz, R. Georgiadis, *Langmuir* **1996**, *12*, 4731.

[127]   D. Yan, J. A. Saunders, G. K. Jennings, *Langmuir* **2002**, *18*, 10202.

[128]   T. Hatsui, H. Setoyama, N. Kosugi, B. Wassermann, I. L. Bradeanu, E. Rühl, *J. Chem. Phys.* **2005**, *123*, 154304.

[129]   A. Knop, B. Wassermann, E. Rühl, *Phys. Rev. Lett.* **1998**, *80*, 2302.

[130]   N. Sändig, F. Zerbetto, *Chem. Commun. (Camb)* **2010**, *46*, 667.

[131]   P. D. Jadzinsky, G. Calero, C. J. Ackerson, D. A. Bushnell, R. D. Kornberg, *Science* **2007**, *318*, 430.

[132]   A. Einstein, *Ann. Phys.* **1905**, *17*, 549.

[133]   S.-W. Joo, *Chem. Lett.* **2004**, *33*, 60.

[134]   T. Kim, K. Lee, M.-S. Gong, S-W. Joo, *Langmuir* **2005**, *21*, 9524.

[135]   S. Chen, R. W. Murray, *Langmuir* **1999**, *15*, 682.

[136]   J. K. Lim, Y. Kim, O. Kwon, S.-W. Joo, *Chem. phys. chem.* **2008**, *9*, 1781.

[137]   S. Nath, S. K. Ghosh, S. Kundu, S. Praharaj, S. Panigrahi, T. Pal, *J. Nanopart. Res.* **2006**, *8*, 111.

[138]   J. Ren, R. D. Tilley, *Small* **2007**, *3*, 1508.

[139]   A. R. Tao, S. Habas, P. Yang, *Small* **2008**, *4*, 310.

[140] D. D. Evanoff, G. Chumanov, *J. Phys. Chem. B* **2004**, *108*, 13957.

[141] S. Cheong, J. D. Watt, R. D. Tilley, *Nanoscale* **2010**, *2*, 2045.

[142] E. V. Shevchenko, D. V. Talapin, H. Schnablegger, A. Kornowski, Ö. Festin, P. Svedlinch, M. Haase, H. Weller, *J. Am. Chem. Soc.* **2003**, *125*, 9090.

[143] P.-Y. Silvert, R. Herrera-Urbina, K. Tekaia-Elhsissen, *J. Mater. Chem.* **1997**, *7*, 293.

[144] M. R. Axet, K. Philippot, B. Chaudret, M. Cabié, S. Giorgio, C. R. Henry, *Small* **2011**, *7*, 235.

[145] X. Zhong, Y. Feng, I. Lieberwirth, W. Knoll, *Chem. Mater.* **2006**, *18*, 2468.

Appendices

A.1 List of chemicals

Chemicals	Company Name	Purity (%)
11-Aminoundecanoic acid	Sigma-Aldrich	99
Borane tert-butylamine complex	Sigma-Aldrich	97
1-Bromooctane	Sigma-Aldrich	99
1-Decanal	Fluka	95
Chloroauric acid	Sigma-Aldrich	99.999
Chloroform	VWR	99.2
Chloroplatinic acid hydrate	Sigma-Aldrich	99.995
Chloro(triphenylphosphine) Gold(I)	Sigma-Aldrich	99.9
Dichloromethane	VWR	100
N-N'-Dicyclohexyldicarbodiimide	Sigma-Aldrich	98
Diethyl ether	VWR	100
Diethyl malonate	Sigma-Aldrich	99
Diisopropyl azodicarboxylate	ABCR	94
4-Dimethylaminopyridine	Sigma-Aldrich	99
Dimethyl formamide	Sigma-Aldrich	99.8
Dimethyl sulfoxide	Sigma-Aldrich	99.5
Dioxane	Merck	99.5
Di-tert-butyl dicarbonate	ABCR	97
Dodecanethiol	Sigma-Aldrich	98
Dodecylamine	Fluka	98
4-Dodecylbenzenesulfonyl chloride	Wako	98
Ethanol	Merck	97
Ethyl acetate	VWR	Technical grade
Formaldehyde	Sigma-Aldrich	36.5
Hexane	VWR	Technical grade

1,2-Hexadecanediol	Sigma-Aldrich	90
Hydrochloric acid	Roth	37
Hydrogen peroxide	Roth	30
Lithium aluminium hydride	Merck	For synthesis
11-Mercaptoundecanoic acid	Sigma-Aldrich	95
Methanol	Sigma-Aldrich	99.9
Methanesulfonyl chloride	Sigma-Aldrich	98
Nitric acid	Roth	65
Octyl ether	Sigma-Aldrich	99
Platinum (II) acetylacetonate	Sigma-Aldrich	97
Potassium hydroxide	Roth	85
1-Pyrene butanol	Sigma-Aldrich	99
Pyridine	Sigma-Aldrich	100
Silver (II) acetylacetonate	Sigma-Aldrich	98
Silver nitrate	Sigma-Aldrich	99.999
Sodium	Sigma-Aldrich	99
Sodium azide	Sigma-Aldrich	99.5
Sodium bicarbonate	Grüssing	99.5
Sodium borohydride	Sigma-Aldrich	99
Sodium carbonate	Roth	99.8
Sodium chloride	Roth	99
Sodium hydroxide	Grüssing	99
Sodium sulfate	Grüssing	99
Sodium thiosulfate	Merck	98
Tetrahydrofuran	Sigma-Aldrich	99.5
Tetraoctylammonium bromide	Sigma-Aldrich	98
Thioacetic acid	Sigma-Aldrich	96
Trifluoroacetic acid	Acros Organics	99
Triphenyl phosphine	Sigma-Aldrich	99

A.2 List of acronyms

AcSH	thioacetic acid
br.	broad band (in NMR)
CH_2Cl_2	dichloromethane
$CHCl_3$	chloroform
DCC	N-N'-dicyclohexylcarbodiimide
DMF	dimethylformamide
DMSO	dimethyl sulfoxide
4-DMAP	dimethylaminopyridine
DIAD	diisopropylazodicarboxylate
EtOAc	ethyl acetate
EtOH	ethanol
Et_2O	diethyl ether
ESI-TOF	electronspray ionization
g	gram
h	hour
HCHO	formaldehyde
HCl	hydrochloric acid
H_2O_2	hydrogen peroxide
HRTEM	high resolution transmission electron microscopy
i.e	that is
KOH	potassium hydroxide
$LiAlH_4$	lithium aluminium hydride
m	multiplet (in NMR)
mL	milli liter
m/z	charge to mass ratio
mmol	milli mole
MeOH	methanol

NaHCO$_3$	sodium bicarbonate
NaN$_3$	sodium azide
NaOH	sodium hydroxide
NaS$_2$O$_3$	sodium thiosulfate
Na$_2$SO$_4$	sodium sulfate
nm	nanometer
NMR	nuclear magnetic resonance
q	quartet (in NMR)
RT	room temperature
s	singlet (in NMR)
SAM	self-assembled monolayer
t	triplet (in NMR)
TOAB	tertaoctylammonium bromide
TEM	transmission electron microscopy
THF	tetrahydrofuran
UV	ultraviolet
Vis	visible

List of Publications and conference proceedings

Publications

- Perumal, S.; Hofmann, A.; Scholz, N.; Rühl, E.; Graf, C. "Kinetics Study of the Binding of Multivalent Ligands on Size-Selected Gold Nanoparticles". *Langmuir* **2011**, *27*, 4456.

- Kirubakaran, S.; Perumal, S.; Bannerji, A.; Rao, D. N.; Chandrasekaran, S. "One Pot Facile Synthesis of New Thio and Seleno Urea Derivatives: New potent Urease Inhibitors". *Bioorg & Med. Chem Lett.* **2007**, *17*, 22, 6387.

- Voggu, R.; Perumal, S.; Chandrasekaran, S.; Rao, C. N. R. "Assembling Nanocrystals and Nanotubes through click chemistry". *Chem. Phy. Lett*. **2007**, *443*, 118.

- Kirubakaran, S.; Perumal, S.; Chandrasekaran, S. "Novel Cyclic Tetraselenides of Mannose: Synthesis, Mechanistic Studies and Structural Properties". *Tetrahedron Lett. 48*, **2007,** 2091.

- Kirubakaran, S.; Perumal, S.; Shubasree, S.; Perali, R. S.; Chandrasekaran, S. "New Chalcogenides of Thymidine and Uridine: Synthesis and Structural properties". *Carbohyd. Res.* **2007**, *342*, 1151.

- Shrutisagar, D. H.; Perali, R. S.; Perumal, S.; Chandrasekaran, S. "Efficient Synthesis of Fused Perhydrofuro [2,3-b] pyrans (and furans) by Ring Opening of 1,2-Cyclopropanated Sugar Derivatives". *Org. Lett.* **2007**, *9,* 1331.

- Perumal, S.; Böttcher, C.; Klatte, T.; Graf, C.; Rühl, E. "Controlled Synthesis of Platinum and Silver Nanoparticles using Amine functionalized Multivalent Ligands". Manuscript under preparation.

Oral Presentation

- Suguna Perumal, Christoph Böttcher, Tom Klatte, Christina Graf and Eckart Rühl. "Controlling the formation of silver and platinum Nanoparticles". 2nd External Doctoral Students Workshop of the Graduate School SFB 765, Rheinsberg, Germany (21-23 Sep 2011).

- Suguna Perumal, Christina Graf and Eckart Rühl. "Binding effects of Multivalent Ligands on Gold, silver and platinum Nanoparticles". University of Hyderabad, India (Aug 21-27 2011).

- Suguna Perumal, Christina Graf and Eckart Rühl. "Kinetics Study of Binding of Multivalent Ligands on Gold, silver and platinum Nanoparticles". International conference on nanomaterials and nanotechnology (NANO 2010), Tiruchengode, India (Dec 13-16 2010).

- Suguna Perumal, Andreas Hofmann, Norman Scholz, Christina Graf and Eckart Rühl. "Kinetics Study of Binding of Multivalent Ligands on Size Selected Gold Nanoparticles". MRS Fall Meeting, Boston, USA (Nov 30- Dec4 2009).

- Suguna Perumal, Andreas Hofmann, Christina Graf and Eckart Rühl. "Kinetics Study of Binding of Multivalent Ligands on Size Selected Gold Nanoparticles". DPG Spring Meeting (Deutsche Physikalische Gesellschaft e.v.), Dresden, Germany (22-27 March 2009).

Poster Presentation

- Suguna Perumal, Tom Klatte, Christina Graf and Eckart Rühl. "Kinetics Study of Binding of the Multivalent Ligands on Gold, silver and platinum Nanoparticles". International Symposium of the Collaborative Research Center (SFB) 765, Berlin, Germany (14-15 Oct 2010).

- Suguna Perumal, Andreas Hofmann, Norman Scholz, Christina Graf and Eckart Rühl. "Kinetics Study of Binding of Multivalent Ligands on Gold, silver and platinum Nanoparticles". Bunsentagung, Bielefeld, Germany (13-15 May 2010).

- Suguna Perumal, Andreas Hofmann, Norman Scholz, Christina Graf and Eckart Rühl. "Kinetics Study of Binding of Multivalent Ligands on size selected Gold Nanoparticles". 1st External Doctoral Students Workshop of the Graduate School SFB 765, Rheinsberg, Germany (7-9 Sep 2009).

- Suguna Perumal, Andreas Hofmann, Norman Scholz, Christina Graf and Eckart Rühl. "Kinetics Study of Binding of Multivalent Ligands on Size Selected Gold Nanoparticles". GOLD 2009, Heidelberg, Germany (26-29 July 2009).

- Andreas Hofmann, Suguna Perumal, Norman Scholz, Christina Graf and Eckart Rühl. "Investigation of the Binding Kinetics of Mono- and Multivalent Thiol Ligands on Gold Nanoparticles". Bunsentagung, Saarbücken, Germany (1-3 May 2008).

Acknowledgments

I would like to extend my sincere thanks to my supervisor Prof. Dr. Eckart Rühl for giving me the opportunity to work in the fascinating field of nanochemistry and for providing me an interactive and good working atmosphere. Additionally, I would like to thank him for his patience, support, thoughtful scientific discussions and for the motivation that helped me to achieve my research goals.

I am grateful to thank Prof. Dr. Christina Graf for her guidance, encouragement, creative ideas which helped me greatly to overcome the difficulties which I encountered during my lab work. I would like to thank her for her patience in reading my manuscript and thesis.

I would like to acknowledge the following people for helping me with various measurements, without which this thesis work wouldn't be possible. I thank Dr. H. Renz, V. Eckert-Funke and S. Selve in the Technical University Berlin and PD. Dr. C. Böttcher (Freie University Berlin) for TEM measurements. Additionally, I would like to extend my immense thanks to NMR and Mass spectroscopy at the Institute of Chemistry and Biochemistry Freie University Berlin for their timely measurements.

I thank Mr. E. Biller (AG Rühl) for constructing the thermostat in fluorescence spectrometer which literally paved way for my extensive work based on fluorescence studies and also for helping with the technical issues in the lab. Further, I thank Mr. S. Thierbach (AG Rühl) also for his technical assistance.

I thank master students Abdal-Azim Al-Terkawi and Tom Klatte for their assistance in the lab.

I would like to specially thank Prof. Rolf Hilgenfeld, Institute of Biochemistry, University of Lübeck, without him I might not have come to Germany for research. I would like to thank him for his help and support during my hard times and for finding the current position in Prof. Dr. E. Rühl's group.

I thank the present and past, laboratory and office colleagues, Andreas, Peter, Shi-Hao, Benni, Xin, Valerie and Christian with whom I shared a very pleasant work time and also for their fruitful scientific discussions. Also I thank other group members who made friendly and relaxed work atmosphere.